Interferometer-Based Studies of Quantum Hall Phenomena

A dissertation presented
by

Douglas Templeton McClure III

to
The Department of Physics
in partial fulfillment of the requirements
for the degree of
Doctor of Philosophy
in the subject of

Physics

Harvard University
Cambridge, Massachusetts
May 2012

Thesis advisor

Charles M. Marcus

Author

Douglas Templeton McClure III

Interferometer-Based Studies of Quantum Hall Phenomena

Abstract

The fractional quantum Hall (FQH) effect harbors a wealth of unique phenomena, many of which remain mysterious. Of particular interest is the predicted existence of quasi-particles with unusual topological properties, especially in light of recent proposals to observe these properties using electronic interferometers. An introduction to quantum Hall physics and electronic interferometry is given in Chapter 1 of this thesis. The remaining chapters, summarized below, describe a set of experiments in which FQH systems are studied using electronic Fabry-Perot interferometry and related techniques.

Since prior studies of electronic Fabry-Perot interferometers revealed unexpected behavior even in the integer quantum Hall (IQH) regime, we began our measurements there. Our initial experiment, presented in Chapter 2, disentangles signatures of Coulomb interaction effects from those of Aharonov-Bohm (AB) interference and provides the first measurement of pure AB interference in these devices. In our next experiment, presented in Chapter 3, we measure AB interference oscillations as a function of an applied dc bias, use their period to study the velocity of the interfering electrons, and study how the oscillations decay as a function of bias and magnetic field.

Moving to the FQH regime, applying a similar-sized bias to a quantum point contact leads to long-lasting changes in the strengths and positions of FQH plateaus. The involvement of lattice nuclear spins in this effect, suggested by the long persistence times, is confirmed using NMR-type measurements. Although the exact physical process responsible

for the effect remains unclear, its filling-factor dependence provides a striking illustration of composite fermion physics. These measurements are described in Chapter 4.

In certain devices, interference oscillations associated with several FQH states are observed. Interpretation of their magnetic-field and gate-voltage periods provides a measurement of quasi-particle charge, and temperature dependence measurements suggest differences between the edge structure of IQH and FQH states. These measurements are described in Chapter 5.

Finally, Chapter 6 presents some recent, not-yet-published observations that may shed light on ways to improve the visibility of existing oscillations and potentially observe interference at additional FQH states. This chapter concludes with a discussion of possible next steps toward achieving these goals.

Contents

List of Figures

Acknowledgments

After spending nine years in the Marcus Lab (three as an undergraduate), reflecting on the countless people who have helped me perform experiments and become a better scientist over this time now amounts to a somewhat daunting task. But the people I'd like to thank first are those without whom this amazing experience would never have even begun. My parents have supported me in every way possible since the day I was born, and so here I'd like to thank them in particular for recognizing the interest I expressed, as soon as I was old enough to crawl, in figuring out how things work, pushing buttons, and tinkering with electronics. Fortunately, despite the negative short-term consequences for various household gadgets, my parents tolerated this fascination of mine and eventually encouraged me to fulfill my curiosity by studying physics.

As for how, as a college freshman, I ended up finding a position in a lab I liked so much that I not only continued working in it year-round for the rest of college, but also defied the conventional wisdom and stuck around for my Ph.D., I should first thank Nathaniel Craig, a former undergrad in the Marcus Lab, for introducing me to Charlie at an event in February 2003 and suggesting that I might like working in his lab. The fact that I've continued to enjoy working here for so long, however, is a testament to what a great advisor Charlie has been. When experiments seem to be going well, he always knows just how to push them to the next level to make the results even more convincing or interesting, and when experiments are not going well, he knows when to be patient and what to try next. He has a great sense for finding the most interesting question to ask and devising the simplest, clearest experiment to answer it. What makes him a truly great advisor, though, is that even from halfway around the world, he actively fosters a positive, collaborative atmosphere in the lab, and sees to it that nothing ever stands in the way of doing science.

One of the best aspects of working in the Marcus Lab has been the opportunity to work alongside and learn from the other students, post-docs, and visitors who have been a

part of the lab over the years. Despite having remarkably diverse backgrounds and interests, Marcus Lab members have always shared an interest in helping each other not only succeed, but have fun along the way. Among the people who guided me during my early years in the lab, I'd like to thank Leo DiCarlo for being such a great role model and teaching me how to do high-quality work in the lab, Yiming Zhang for inspiring me to be thorough and efficient while still enjoying the work, and David Reilly for his eagerness to lend a hand or crack a joke whenever either was needed.

In my first year of grad school, after switching from the "Noise Team" to the "5/2 Team," I had the pleasure of working with several people from whom I learned a great deal. I'd like to thank Jeff Miller for introducing me to both quantum Hall physics and the cleanroom, Eli Levenson-Falk for helping out in both the cleanroom and the lab, Reinier Heeres for his help in setting up the fridge and the lab wiki, and Iuliana Radu from the Kastner group for many useful and enjoyable discussions. Yiming also joined the 5/2 Team not too long after I did, and continued to be a fantastic mentor and friend.

During my later years of grad school, after all of my early colleagues had left, I continued to have the good fortune of working closely with some exceptionally talented and hardworking first- and second-year grad students. I thank Angela Kou for her enthusiasm and tenacity even when it seemed like nothing was going right, and for her patience as I learned to be a better mentor by trial and error. I thank Willy Chang for his unflagging eagerness to step up and do whatever was necessary to move the experiment forward at any time of the day. Reflecting on the two years during which I was nominally the one helping to teach Angela and Willy how to do experiments, I am particularly struck by two realizations: how much I ended up learning from both of them, and how much I'll miss them after I graduate. Although I worked with Patrick Gallagher for only a short time, his knack for asking questions that tested the limits of my knowledge, and especially his

desire to understand every detail of a problem, pushed me to become a more careful thinker in the lab. I'd also like to acknowledge our summer REU student Paden Roder, who was a pleasure to work with and made valuable contributions to our efforts to develop a new device fabrication process.

The contributions of other members of the Marcus Lab to my learning and happiness over the years are too numerous to permit a detailed account, but I would like to acknowledge Hugh Churchill, Edward Laird, Maja Cassidy, Christian Barthel, Jimmy Williams, Jim Medford, Andrew Higginbotham, Patrick Herring, Ferdinand Kuemmeth, Javad Shabani, Vlad Manucharyan, Brandon Armstrong, Merritt Moore, Ruby Lai, Menyoung Lee, and Jason Wien for being great colleagues and friends. I'd like to thank Hugh in particular for suggesting that I join him as a teaching fellow for Professor Eric Heller's "The Physics of Music and Sound," and thank both Professor Heller and Professor Tom Hayes ("Laboratory Electronics") for the opportunity to teach for them.

The other members of my thesis committee, Professors Yacoby and Kastner, have each helped me to better understand certain aspects of my research over the years, often simply by knowing exactly the right question to ask at the right time. Given the significant overlap in research areas between the Marcus Lab and the Yacoby Lab two floors above us, it is not surprising that I benefited from many useful conversations with Vivek Venkatachalam, Sean Hart, Mikey Shulman, and other members of the Yacoby group. What I'm even more grateful for are our regular tennis matches; I hope we continue to find the time to play on occasion. I also enjoyed useful discussions with Xi Lin and Colin Dillard of the Kastner Lab.

It has been a great privilege to have enlightening discussions with many prominent theorists in the field, most notably Bert Halperin, Ady Stern, Bernd Rosenow, Dima Feldman, Izhar Neder, and Claudio Chamon. I appreciate their invaluable insights, their

dedication to figuring out the complex theoretical models that have helped explain our experimental results, and their patience in helping me understand said models.

The study of the fractional quantum Hall effect would not have progressed nearly as much as it did over the last thirty years without the work of Loren Pfeiffer and his colleagues to continually improve the quality of the gallium arsenide wafers in which the effect is seen. I'd like to thank him for not only these contributions to the field, but also for helping me find wafers suitable for my purposes, and growing new ones as needed. In recent years, his former colleague Michael Manfra also started his own growth effort, and I thank him for providing wafers and useful discussions about how to improve their design.

I spent many hours during my first two years of grad school working on the coldfinger, filter boxes and other hardware to be mounted in the dilution refrigerator. I am grateful to Jim Eisenstein for teaching me several tricks of the trade, and also for setting an example of how to do careful experiments and give clear presentations. I was also helped tremendously by Louie, Al, and the rest of the staff at the SEAS machine shop, who not only did an excellent job machining the parts, but also helped me improve my designs and could always find a way to squeeze in rush orders when necessary. I would like to thank the Gabrielse group for allowing me to use their vacuum brazing system to assemble the coldfinger. For hardware and electrical work outside the fridge, Frank Morrissey, Michele Waters, and their teams have also been extremely helpful.

Scientists are known for being absent-minded, and for good reason: science often requires intense focus on a particular problem, leaving little mental energy to spare for more practical matters. Fortunately, the administrators for the Marcus group and the physics department have been excellent at taking care of such practical matters. I'd like to thank all of them, including James Gotfredson, Jess Martin, Rita Filipowicz, Sheila Ferguson, Carol Davis, and Bill Walker, for all of their behind-the-scenes work that allowed me to focus

on my experiments, and for never appearing too fazed by my various urgent, last-minute requests.

Device fabrication at the Harvard Center for Nanoscale Systems (CNS) has been an integral part of my research. The expansion of the cleanroom facilities that occurred following the move into the LISE building provided new equipment without which certain aspects of my fabrication process would not have been possible. Although this expansion was accompanied by a meteoric increase in the number of new cleanroom users, the dedication of the CNS staff ensured that not only did the equipment keep working, but the sense of community among the researchers and staff was maintained. I'd particularly like to thank Yuan Lu, Mac Hathaway, Ed Macomber, Noah Clay, Dave Lange, and Steve Paolini for their help and for making the CNS cleanroom such an amazing place to work.

This project would not have been possible without funding from Microsoft's Project Q. I'd like to thank everyone at Microsoft whose long-term vision and love of science has made this unique collaboration possible, including but certainly not limited to Michael Freedman, Chetan Nayak, and Sean Fraer, who each contributed in various ways to making the semi-annual meetings in Santa Barbara so enjoyable and interesting.

Although I've spent most of my time during graduate school working in the lab and the cleanroom, I've also managed to have a great time outside the lab thanks to many people. Christy, I never thought I'd meet someone whose personality, interests, and dreams would mesh so well with mine. Thank you for putting up with my sometimes-excessive dedication to checking my experiment on my phone, for encouraging me to work more efficiently and get more sleep, and for all the fun adventures we've had and will surely have. It was a pleasure living with Josh, Lee, Helen, Asif and Kyle (not all at once!) over the last several years, and I especially appreciate their tolerance of my unpredictable work, sleep and cooking schedules. I'd also like to thank all of my friends who have helped make our

yearly ski trips into a great tradition that I hope we'll continue for years to come.

Finally, a unique aspect of graduate student life at Harvard is the extensive social, athletic, intellectual and cultural programming available through the Dudley House community. Participating in this community has been a great way not only to meet graduate students from other fields, but also to discover a new dimension of people I previously interacted with only in the cleanroom or the classroom. In addition to all of my friends from these activities, I would like to thank the Dudley House Masters Jim and Doreen Hogle for fostering such a great community, Susan Zawalich and Chad Conlan for keeping it running smoothly, and Jon Fan for encouraging me to become a Dudley Athletics Fellow, one of the most rewarding activities I did during graduate school and the source of some of my best memories.

Chapter 1

Introduction

1.1 Motivation

For the last six years, I've studied the physics of electrons confined to a two-dimensional plane in a gallium arsenide (GaAs) crystal at extremely low temperatures and high magnetic fields. Since I'm sure many of my friends and family who have supported me throughout this effort nonetheless wondered what drove me to spend so much time studying such a seemingly random and esoteric problem, I'd like to begin this first section by trying to convey, in the least technical terms possible, what makes the fractional quantum Hall effect so captivating.

Our system of interest is a GaAs-based two-dimensional electron gas (2DEG) in a Hall bar geometry: a rectangular piece of semiconductor material designed to confine electrons to a 2D plane near the top of the chip, with metal blobs along the edges through which electrical contact to the 2DEG can be made. A sample GaAs Hall bar is shown in Figure 1.1(a). Suppose we try to cool such a chip from room temperature ($T \approx 300$ K) to absolute zero, while periodically performing the measurements illustrated in Figure 1.1(b) as a function of the magnetic field B applied perpendicular to the 2DEG. The applied current I_{x}

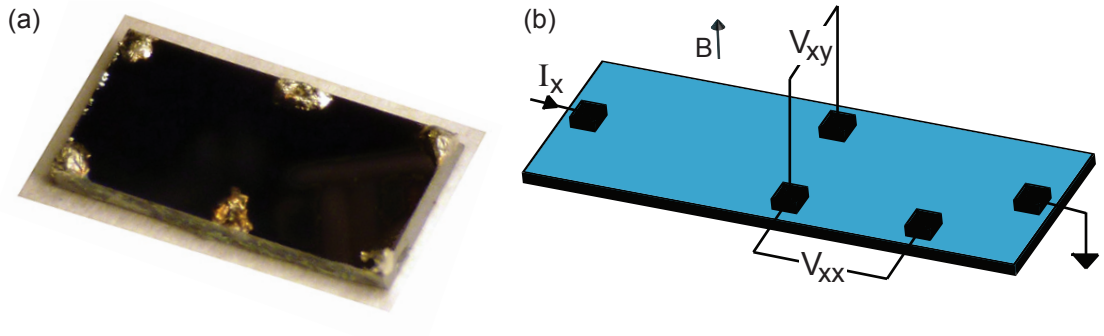

Figure 1.1: (a) GaAs Hall bar with six indium contacts. (b) Schematic Hall bar indicating a typical measurement configuration. A current bias I_x applied at one end of the sample gives rise to voltages V_{xy} and V_{xx}, from which the Hall and longitudinal resistances are calculated as $R_{xy} = V_{xy}/I_x$ and $R_{xx} = V_{xx}/I_x$.

gives rise to two voltages: V_{xx}, along the direction of current flow, comes from dissipation, and V_{xy}, in the transverse direction, comes from the bending of electron trajectories by the magnetic field. From these measured voltages we calculate the longitudinal resistance $R_{xx} = V_{xx}/I_x$ and the Hall resistance $R_{xy} = V_{xy}/I_x$. For almost the whole cooldown, we observe little qualitative change in the magneto-transport features: R_{xy} is proportional to B, and R_{xx} is more or less constant as a function of B. Approaching $T \sim 4$ K, the boiling point of liquid helium at standard pressure, the Hall resistance begins to develop a regular series of plateaus at resistances $R_{xy} = h/(\nu e^2)$, where ν is a positive integer, each accompanied by an equally broad region of vanishing longitudinal resistance. Such behavior is shown in Figure 1.2(a).

Below this temperature, even more plateaus begin to appear, now with Hall resistances corresponding to rational fractions $\nu = r/s$, where r is an integer and $s = 3, 5, 7, \ldots$. As seen in Figure 1.2(b), these plateaus are strongest when $s = 3$, and become weaker with higher s. At this point, one might remark that the integer values of ν are merely the special case of $\nu = r/s$ with $s = 1$, a natural precursor to the $s = 3, 5, 7, \ldots$ series. Indeed, it turns out that the plateaus at integer and fractional values of ν are related, though in a much

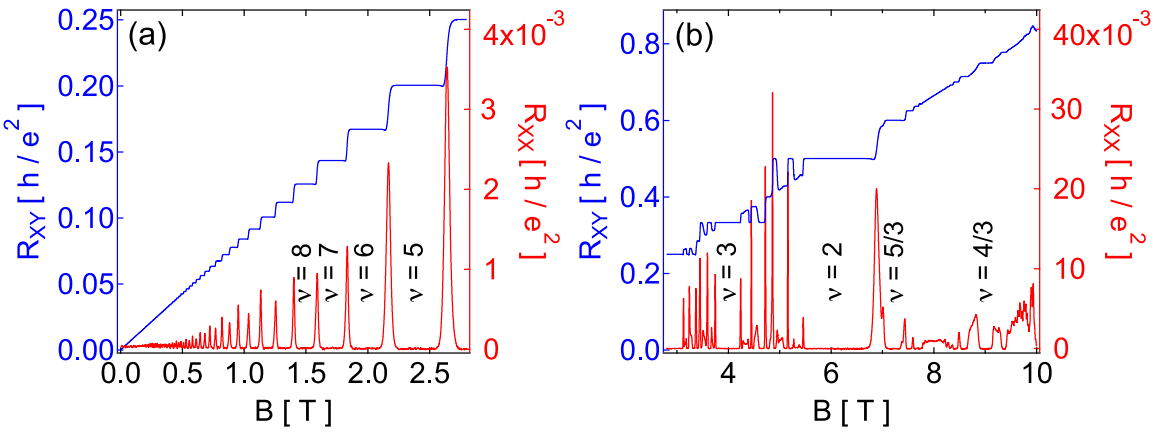

Figure 1.2: Hall (blue) and longitudinal (red) resistances as a function of magnetic field at a temperature of about 0.01 K. (a) As magnetic field is increased, a transition from classical to quantum Hall behavior is observed. (b) At even higher magnetic fields, the Hall resistance exhibits plateaus at fractional filling factors and even non-monotonic features.

more complex way than this simple mathematical observation suggests. Continuing the trip toward absolute zero, more fractional plateaus continue to appear and strengthen, and if we happen to have an especially nice GaAs wafer with just the right structure, grown under just the right conditions, a surprising feature might begin to appear below $T \sim 0.1$ K: a single plateau corresponding to a value of ν with an even denominator: 5/2. Cooling a little further, a similar feature begins to appear at $\nu = 7/2$. Approaching $T \sim 0.02$ K, these plateaus and the associated zeros in R_{xx} become more fully developed, but no other clear even-denominator plateaus appear. Finally, by $T \sim 0.01$ K, the closest to absolute zero we'll be able to get, one more surprising feature develops: the Hall resistance, which at higher temperatures increased monotonically as a function of B, now exhibits striking non-monotonic features near the $\nu = 5/2$ and $\nu = 7/2$ plateaus.

As this hypothetical experiment illustrates, cooling a 2DEG to the lowest attainable temperatures produces a remarkable evolution in which layer upon layer of new phenomena develop at an increasing rate. The proportionality of R_{xy} to B at all tempera-

tures, known as the classical Hall effect, arises from Lorentz's law and was first observed in 1879 [1]. The plateaus at integer ν, known as the integer quantum Hall Effect (IQHE), arise from the quantum-mechanical requirement that an electron moving in a circular orbit have a single-valued wave-function at all points, as a result of which its energy may only take on certain discrete values. First observed in 1980 [2], the IQHE is remarkably robust: aside from the easily satisfied requirement of a 2D conductor (see Section 1.2.2), most details of the system do not affect the basic phenomenology, and in fact the quantization of the R_{xy} plateaus has been measured to be consistent across samples at a level on the order of a part in a billion [3]. The plateaus at fractional ν, known as the FQHE, came as quite a surprise when they were first seen in 1982 [4]. Though phenomenologically similar to the IQHE plateaus, they in fact arise from an entirely different source, namely the electron-electron repulsion described by Coulomb's law [5]. The two even-denominator FQHE plateaus, first seen in 1987 [6], appear likely to involve one additional ingredient: a pairing effect [7] analogous to that in the BCS model [8] of superconductivity. While in BCS superconductors such pairing (a sort of electron-electron *attraction*) arises from an electron-phonon coupling, here it appears to arise from a particular softening of the electron-electron repulsion by screening from electrons well below the Fermi energy, which do not participate in transport. Remarkably, a common technique in many-body physics, that of defining a new set of particles in terms of which to describe the system, allows the IQHE and FQHE to be unified into a single framework known as Composite Fermion Theory [9]. Finally, the non-monotonic features, known as the re-entrant IQHE, appear to arise from segregation of the 2DEG into bubble-like regions of one IQHE state in a background of a different IQHE state [10, 11].

This cornucopia of interesting phenomena is rendered even more intriguing (and potentially even useful!) by certain properties believed to be associated with the FQHE,

especially the $\nu = 5/2$ state[1]. As hinted, though certainly not implied, by the fractionally quantized Hall resistances, electrical current is carried in the FQH regime not by electrons but by fractionally charged quasi-particles. Even more intriguing, these quasi-particles are expected to exhibit fractional statistics [12], the still-unobserved property that braiding one around another can lead to an observable change in their quantum-mechanical phase. Naturally, the even-denominator states might be expected to have even more special properties, and indeed, the Moore-Read wavefunction [7] that may describe these states predicts them to exhibit non-Abelian statistics, in which braiding of identical particles not only changes their relative phase but also transforms the system from one ground state to another. The observation of such behavior would not only represent a major milestone in physics but also represent the first step toward building a topological quantum computer [13], which in principle could be made extremely robust against decoherence [14].

In short, quantum Hall systems are a physicist's funhouse, with fascinating features around every turn and new doors opening where walls used to appear. I feel very fortunate to have had the opportunity to learn about these systems and contribute to our understanding of them in some small way. With so many puzzles still unsolved, I look forward to seeing where their answers lead.

1.2 Fermions in two dimensions

As discussed in the preceding section, the fractional quantum Hall effect is comprised of several layers of physical phenomena. This section will briefly review the major concepts associated with each layer, starting with general properties of electrons in two dimensions and progressing all the way through proposals for detecting non-Abelian statistics

[1]The 5/2 state gets much more attention than its 7/2 cousin by virtue of being the stronger, better-developed of the two states, but their underlying physics is expected to be nominally the same.

at $\nu = 5/2$. Emphasis will fall on topics relevant to understanding the experiments presented in the subsequent chapters. While the focus will be on theoretical concepts, relevant experimental results will be mentioned throughout. Details of experiments directly relevant to those presented in this thesis will be saved for Section 1.4.

1.2.1 Fermi sea in 2D

For a variety of reasons that will become apparent throughout the remainder of this chapter, all of the phenomena studied in this thesis require the confinement of charge-carrying particles (in our case, electrons) to a 2D plane. For free, non-interacting fermions in a 2D plane with periodic boundary conditions, single-particle wavefunctions are traveling waves identified by three quantum numbers: a spin (up or down) and a momentum $\hbar\vec{k} = \frac{2\pi\hbar}{L}(N_x, N_y)$, where N_x and N_y are integers and L is the length on which the wavefunction is periodic in both the x and y directions. The corresponding energies are $E_k = \frac{\hbar^2 k^2}{2m}$, where m is the particle mass. In equilibrium, particles in the system will settle into the lowest-energy configuration, but being fermions, only one can occupy each allowed state. This combination of constraints results in the formation of a *Fermi sea* in which each state with an energy $0 \leq E_k \leq E_F$ is occupied by a single fermion, and all higher energy states are unoccupied; the maximum occupied energy E_F is known as the *Fermi energy*. For a 2D system, it can be shown [15] that $E_F = \frac{\hbar^2 \pi n}{m}$, where n is the density of particles.

1.2.2 Semiconducting quantum well heterostructures

Confinement of charge-carrying fermions is typically achieved using a layered semiconductor heterostructure in which a bandgap difference between adjacent layers forms a potential well in which the carriers donated by a remote dopant layer collect, as illustrated in Figure 1.3. The shape of this well can be approximated as either triangular or square

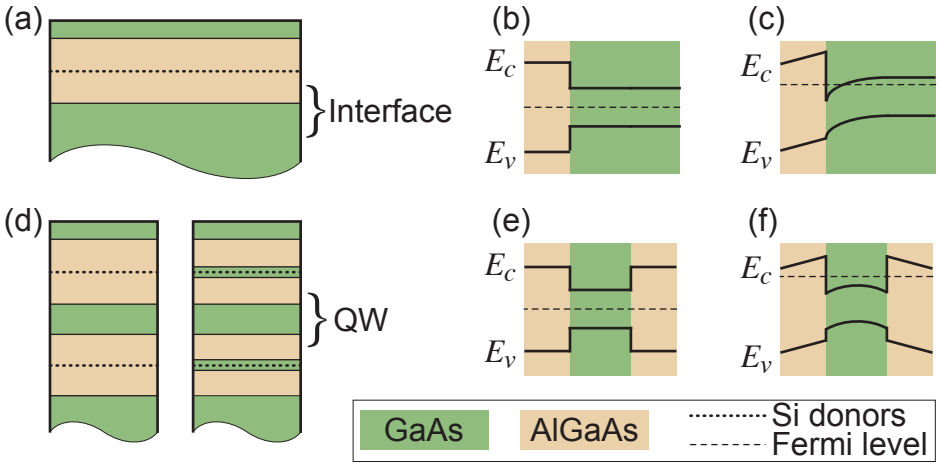

Figure 1.3: Heterostructure designs and their associated band structures for confining a 2DEG at a single interface (a-c) or a quantum well (d-f). Band-structure diagrams, corresponding to the regions indicated by the brackets in (a) and (d), show the bottom of the conduction band (E_c), the top of the valence band (E_v) and the Fermi level E_F both before (b,e) and after (c,f) doping. Free electrons accumulate in the regions where $E_F > E_c$. In the quantum-well structure (d), Si donors are sometimes placed directly in the AlGaAs spacer (left) and sometimes in a narrow GaAs quantum well known as a doping well (right).

depending on the structure, and the system of carriers can be considered 2D in nature when the two lowest-energy localized states of this potential differ by a large enough energy that all localized particles reside in the lowest state.

Such heterostructures are typically grown using molecular beam epitaxy [16] from a combination of two semiconductor materials with different bandgaps [17]. In III-V systems such as GaAs, Si dopants can serve as electron donors if they take the place of the Group III material or acceptors if they take the place of the Group V material, allowing the creation of either 2DEG or 2D hole gas (2DHG) structures. For high-mobility applications, the GaAs/AlGaAs system is a popular choice since the similarity of the GaAs and AlAs lattice constants (both close to 5.65 Å) minimizes crystal strain and the likelihood of defects at the layer interfaces. More details of these structures are discussed in Section A.1. Although the IQHE and FQHE have been observed in both 2DEG's and 2DHG's in several different III-V

systems, as well as CdTe [18] and graphene [19], the GaAs/AlGaAs-based 2DEG remains the system in which the highest mobilities have been recorded [20], and moreover the only one in which the FQH state at $\nu = 5/2$ has been reported.

1.2.3 GaAs 2DEG in zero magnetic field

Contrary to the assumption made in Section 1.2.1, the electrons in a semiconductor-based 2DEG are not free, but in fact experience a periodic potential from the host lattice. Remarkably, the effects of this potential can largely be accounted for by simply considering the electrons to have a different effective mass, given in GaAs by $m^* = 0.067m_e$ [15]. With this number, we can evaluate some of the important energy scales governing the formation and behavior of the 2DEG. Typically the structures used for these experiments use an AlGaAs-GaAs-AlGaAs square-well with a GaAs-layer thickness of roughly $a = 30$ nm. The AlGaAs-GaAs bandgap difference, roughly 300 meV [17], can be assumed larger than any other relevant energy scale, in which case the energy gap between the ground and first excited states of this potential can be approximated by that of an infinite square well:

$$\Delta E_{QW} = E^2_{QW} - E^1_{QW} = \frac{\hbar^2\pi^2}{2m^*a^2}(2^2 - 1^2) = 19 \text{ meV}. \tag{1.1}$$

A typical electron density in these samples is on the order of $n = 2 \times 10^{11}$ cm^{-2}, yielding a Fermi energy of $E_F = 7.1$ meV, less than ΔE_{QW} as required, though perhaps not by as much as one might have hoped. Furthermore, comparisons of ΔE_{QW} and E_F to the temperature scale of the experiment (usually on the order of 10 mK = 0.86 μeV) reveal respectively that thermal population of the quantum well's second subband is negligible and that 2DEG transport is dominated by electrons at energies very close to E_F.

Although a perfectly periodic potential does not scatter electrons [15], even the most carefully grown GaAs wafers have many defects at which scattering may occur, and interfaces and donor impurities also contribute to scattering [21, 22]. Although these different

types of scattering may affect electron transport differently, their relative contributions in a single sample are difficult to evaluate, and so the degree of scattering is typically quantified by a combined effective scattering time τ inferred from a Drude-model calculation [23]. In this model, just as air resistance causes a falling object to reach a terminal velocity, so do scattering events cause electrons accelerating in an electric field to reach a drift velocity, v_{d}. One finds that the drift velocity is proportional to the applied electric field, and the proportionality constant, known as the mobility, is given by $\mu = e\tau/m^*$. Converting the drift velocity to a drift current using $J = nev_{\mathrm{d}}$, and applying Ohm's law, allows μ to be calculated from the measured conductivity as $\mu = \sigma/(ne)$. In the 2DEG's used for these experiments, with $\mu \gtrsim 15 \times 10^6$ cm^2/(V $\cdot$ s) (see Appendix D), this model implies an effective scattering time of $\tau \gtrsim 0.5$ ns. A discussion of scattering processes limiting τ and hence μ, as well as the relationship of μ to the quality of the FQHE features, can be found in Section A.1.

1.2.4 Quantum Hall effects

A 2DEG of electron density n subject to a perpendicular magnetic field $B_\perp$ can be characterized by the ratio of electron density to magnetic field strength, quantified by the dimensionless filling factor ν:

$$\nu = \frac{n}{B/\phi_0}, \tag{1.2}$$

where $\phi_0 \equiv h/e$ is the magnetic flux quantum. The experimental observations that R_{xx} is nearly independent of $B_\perp$ and $R_{\mathrm{xy}} \propto 1/B_\perp$, seen in all samples at temperatures high enough that quantum effects can be neglected, can be understood through a classical Drude-model argument analogous to the one presented in Section 1.2.3 but with an added Lorentz force term [23]. Measuring R_{xy} vs. $B_\perp$ is the most commonly used method of determining n, which, along with the measured R_{xx}, can be used to calculate μ. At lower temperatures, the

quantized plateaus in R_{xy} and zeroes in R_{xx} that appear near all integer and certain fractional values of ν are signatures of the IQHE and FQHE, respectively. This section describes the salient features of these effects and relevant considerations for their observation.

Integer quantum Hall effect

An electron at the Fermi energy in a 2DEG subject to a perpendicular magnetic field $\mathbf{B}_\perp$ experiences a Lorentz force $\mathbf{F} = |e|\mathbf{v_F} \times \mathbf{B}_\perp$ in the plane of the 2DEG. In the absence of significant electric fields from scattering sites, sample edges, or an applied bias, this force leads to circular motion at the cyclotron frequency $\omega_c = eB_\perp/m^*$. The periodic return to the same position (guaranteed in 2D but not 3D) imposes boundary conditions on the electron wavefunction that lead to quantization of the angular momentum. The resulting discrete allowed energies,

$$E_N = \hbar\omega_c(N + 1/2), \tag{1.3}$$

are known as Landau levels (LL's), each of which has a degeneracy given by $2B_\perp/\phi_0$, corresponding to one spin-up and one spin-down state per flux quantum. In practice, Zeeman splitting (and valley splitting in materials such as graphene) split each LL into subbands, but we ignore these non-universal effects for now. As seen in Figure 1.4, the energy of each LL is bent upwards by the confining potential at the edges of the Hall bar; notably, each LL that lies below E_F in the bulk of the sample crosses E_F near the edge. This situation leads to distinctive transport characteristics: when E_F lies between LL's in the bulk, the absence of low-energy excited states suppresses conduction, just as in a standard insulator; on the other hand, low-energy excitations do exist at the points near the edges where each LL crosses E_F, leading to the formation of conducting strips known as edge states. Each strip is effectively a 1D quantum wire [24], and therefore has a conductance of $2e^2/h$. What makes the quantum Hall edge states different from other quantum wires is

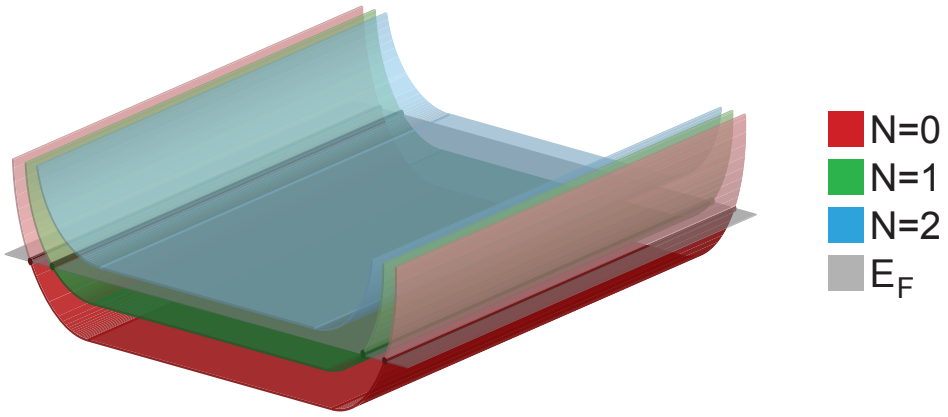

Figure 1.4: Schematic diagram of Landau levels in a 2DEG. In the bulk of the 2DEG, LL's below the Fermi energy are occupied. At the 2DEG edges, LL energies are bent upward by the confining potential, leading to the formation of chiral, current-carrying edge states.

their chiral nature: as expected from a classical skipping-orbit picture, the magnetic field forces electrons to move in a single direction along the edge of the sample, either clockwise or counterclockwise depending on the direction of the field. The resulting strong suppression of backscattering is the origin of the ultra-precise quantization.

In real systems, the LL energies are not exactly quantized but can be broadened by temperature, quantum lifetime, and disorder. The disorder broadening in particular plays an important role in creating the quantized plateaus: without disorder, the values of ν at which E_F lies between LL's would comprise a set of measure zero, and so the plateau widths would be negligibly small. The presence of hills and valleys in the potential, however, creates bands of localized states at energies just above and below each E_N. As a result, instead of jumping straight from E_N to $E_{N\pm1}$ as ν is increased or decreased, E_F lies between E_N values over a significant range of ν centered around each quantized value. Since only the states exactly at E_N (i.e. within kT or $\hbar/\tau$) are delocalized, the bulk remains insulating over the broad ranges of ν where R_{xy} plateaus are seen experimentally.

IQHE in GaAs

For electrons in GaAs, the Zeeman splitting between spin-up and spin-down states is $E_Z = |g|\mu_B B$, where $|g| \approx 0.44$ is the magnitude of the g-factor in GaAs, $\mu_B = e\hbar/2m$ is the Bohr magneton (note that m is the bare electron mass, not the effective band mass), and B is the total magnetic field, which in these experiments always equals $B_\perp$. At $B_\perp = 1$ T, roughly the lowest field at which most data presented in this thesis is collected, the cyclotron energy is $E_c = \hbar\omega_c \approx 1.7$ meV, equivalent to a temperature on the order of 20 K, and the Zeeman energy is $E_Z \approx 25$ μeV, corresponding to a temperature on the order of 300 mK. As a result, at the temperatures and magnetic fields of these experiments, temperature broadening of the LL's is insignificant. As for lifetime broadening, caused by the finite scattering time and the energy-time uncertainty principle, the typical scattering time of 0.5 ns found in Section 1.2.3 yields a broadening of $\hbar/\tau \sim 1$ μeV, comparable to or smaller than the effect of temperature.

Fractional quantum Hall effect

Soon after the discovery of the IQHE, whose basic principle was well understood, a stunning discovery was made: weak plateaus in R_{xy} and minima in R_{xx} at $\nu = 1/3$ and possibly 2/3 [4]. As in the IQHE, these features suggested the presence of an energy gap preventing transport in the bulk of the sample. Given the fractional values of ν, however, a different mechanism had to be responsible for the creation of the gap in this case.

The use of the term "gas" implies that the electrons in a 2DEG interact only weakly with each other. Under most circumstances, this approximation is valid since 2DEG densities are high enough that the electrons' kinetic energy ($\propto n$) dominates their interaction energy ($\propto \sqrt{n}$) and interactions are well screened. At high magnetic field, however, the quantization of the cyclotron motion means that although a large kinetic energy is still

present, it is fixed by the strong magnetic confinement and cannot contribute to screening. As a result, the Coulomb interaction energy can become significant and even dominant, opening the door to strongly correlated electron behavior. As it turns out, such behavior is in fact responsible for the FQHE: at certain filling factors, the system of electrons is able to reduce its energy by condensing into a strongly correlated ground state. A possible wavefunction for such a state was first proposed by Laughlin [25] to describe the behavior at $\nu = 1/3$.

Since then, the development of 2DEG's with higher mobilities has led to the discovery of a vast set of FQHE states of varying strengths. The overwhelming majority occur in the lowest Landau level ($\nu < 2$), but a few, including the only even-denominator states ($\nu = 5/2, 7/2$, and possibly $19/8$) appear in the second Landau level. No FQH states have been seen in any Landau levels beyond the second. Despite the dizzying array of seemingly random values of ν at which FQHE states form, careful analysis reveals a fascinating pattern that captures not only the observed filling factors but also their relative strengths. The model accounting for this behavior is presented in the next section.

Composite fermion model

All Hamiltonians in condensed matter physics contain interaction terms, which generally prevent exact solutions of the full Hamiltonian for systems containing more than a handful of particles. Since typical systems actually contain somewhere on the order of 10^{23} particles, evidently approximations need to be made. In many cases, such as in the IQHE, the interaction energy is small compared to some other energy scale, in which case a good approximate solution can be found perturbatively, i.e. by first solving the problem with the interaction terms set to zero, and then calculating the effect of the interaction terms on these solutions to first or second order.

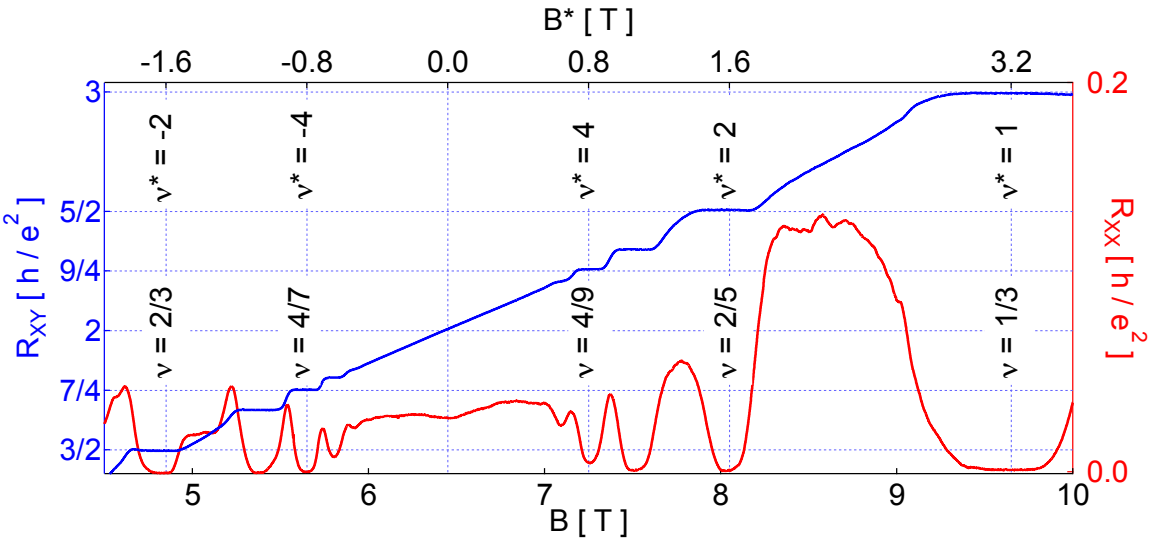

Figure 1.5: Data illustrating the CF-model correspondence between IQH and FQH states. The actual field and electron filling factors are indicated by B and ν, while the effective field and CF filling factors are indicated by B^* and ν^*.

In the case of the FQHE, however, the interaction terms dominate the Hamiltonian because of the aforementioned quenching of the kinetic energy by Landau level quantization. Without help from a quantum computer, the problem is essentially unsolvable by brute force. Fortunately, a comparison of the FQHE to the IQHE suggests that a common trick in many-body physics, perhaps most famously used in the BCS theory of superconductivity [8], may be applied here as well. As evident from Figure 1.5, the strongest series of FQHE states, centered around $\nu = 1/2$ and $B = 6.5$ T, would be all but indistinguishable from a series of IQHE states centered around zero field if the axis labels were removed. Evidently the FQHE *is* the IQHE of some particle or another. If we can identify that particle, which we presume is weakly interacting since it exhibits the IQHE, then we can understand the mechanism of the FQHE just as Bardeen, Cooper and Schreiffer explained superconductivity in terms of weakly interacting Cooper pairs.

The fact that the strongest sequence of fractions always radiates from $\nu = 1/2$

provides a key clue as to the composition of these weakly interacting particles: whatever the particles are, they evidently feel zero effective magnetic field here despite the presence of a relatively strong field providing two magnetic flux quanta per electron. If, on the other hand, two flux quanta somehow associate themselves with each electron to form a new composite particle, then these particles will effectively feel zero magnetic field since there are no remaining flux quanta. This argument is at the heart of the composite fermion (CF) model of the FQHE, and its validity has been borne out by many experimental observations, even at magnetic fields where the FQHE is not observed [26, 27]. In the most general case, each electron can be associated with $2p$ flux quanta, transforming the system of electrons at magnetic field B into one of ^{2p}CF's in an effective magnetic field of $B^* = B - 2p\rho\phi_0$, where the electron density is represented by ρ instead of n, as is typical in this context, for reasons that will become clear presently. At $B^* = 0$, the CF's may be expected to form a Fermi sea, and as B is varied away from the value at which $B^* = 0$, quantized cyclotron motion of CF's may be expected to lead to the formation of composite fermion Landau levels (CF-LL's) in analogy with the standard IQHE. In particular, CF-LL's should occur at positive and negative integer values of

$$\nu^* = \rho/(B^*/\phi_0) = \nu/(1 - 2p\nu), \tag{1.4}$$

which occur for values of ν given by

$$\nu = n/(2pn \pm 1) \tag{1.5}$$

for all positive integers n, with $n = |\nu^*|$. While Equation 1.5 can yield many more values of ν than have been shown to demonstrate FQHE, combining this equation with the fact that by analogy with the IQHE, the CF-LL gap should be proportional to $1/n$, as well as the intuition that higher values of p might lead to weaker states, one arrives at reasonable predictions for the FQHE states that should be observed and their relative strengths.

Filling factor 5/2 and other second Landau level features

Laughlin's wavefunction and its generalization in the CF model were motivated in part by the lack of observed FQH states at even-denominator values of ν, and the relevance of the CF model was further established by the observation of Fermi sea-like behavior near $\nu = 1/2$ and $3/2$; FQHE-like behavior at an even-denominator filling factor would suggest a system of composite bosons [28]. As it turns out, such behavior is seen in the second Landau level, and was first observed [6] just as the CF model was being developed. The FQH state at filling factor $\nu = 5/2$, shown in Figure 1.6, has recently become the most-studied aspect of the FQHE, and yet it remains one of the most mysterious. Several wavefunctions [28, 29, 30, 7, 31] have been suggested that may describe the boson-like behavior believed to occur here, most famously the Pfaffian wavefunction developed by Moore and Read [7]. This wavefunction is remarkable in that not only does it potentially describe the behavior of this bizarre state, and do so in terms of a CF pairing analogous to the BCS model of superconductivity, but most surprisingly, the excitations of a ground state described by this wavefunction have been shown theoretically [32] to obey not only anyonic but even non-Abelian statistics, a subject to be discussed further in Section 1.2.5. At present, there is some experimental evidence in favor of the Moore-Read wavefunction [33, 34, 35, 36, 37], but other less-interesting possibilities cannot yet be ruled out. As hinted at the end of Section 1.1 and discussed further in Section 1.2.6, the history of the QHE—especially in the second Landau level—is full of surprises.

In addition to the 5/2 FQH state, another striking set of features appears in the second LL, as shown in Figure 1.6: four additional zeroes in R_{xx} accompanied by non-monotonic features in R_{xy} that saturate at an integer value of ν. These features, which largely disappear above about 20 mK, are termed the re-entrant integer quantum Hall effect (RIQHE) and believed to arise from so-called "bubble" [10, 11] phases in which the

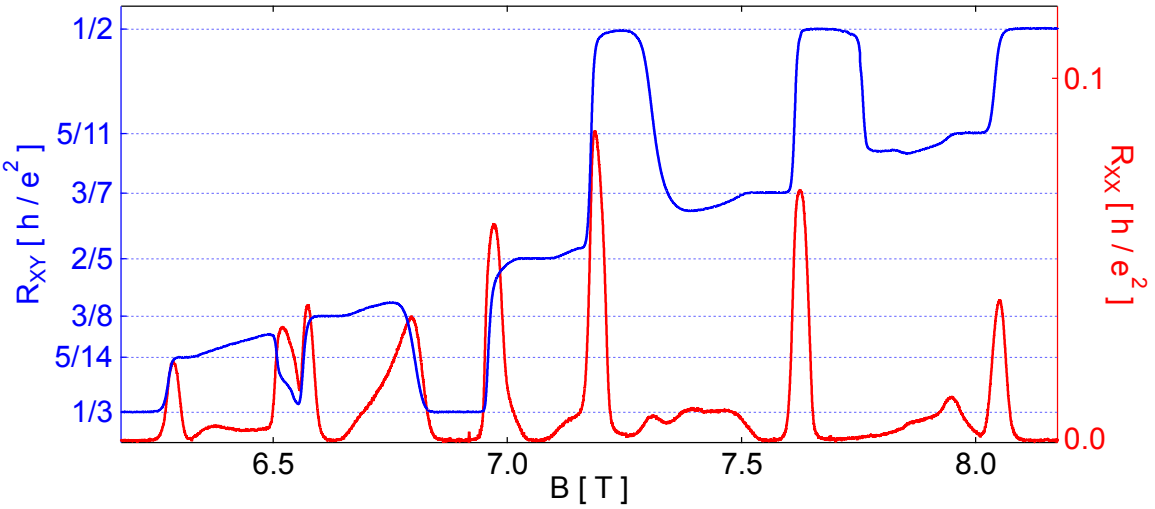

Figure 1.6: Hall (blue) and longitudinal (red) resistances as a function of magnetic field in the spin-up branch of the second Landau level. Notable features include the plateau at $R_{\rm xy} = 2/5\ h/e^2$, corresponding to the $\nu = 5/2$ FQHE state, and the four non-monotonic features in $R_{\rm xy}$, known as the RIQHE.

2DEG separates into distinct regions of $\nu = 2$ and $\nu = 3$ like drops of oil in a film of water. These features are not studied explicitly here, but their presence and strength provides a sensitive gauge of electron temperature in the $5 - 25$ mK range (see Section B.5.2).

1.2.5 Unique properties of fractional quantum Hall states

So far, we have focused on developing an understanding of FQH states in their ground state, i.e. with all CF-LL's either completely filled or empty. In reality, excitations are almost always present, arising from three main sources: filling factor, temperature, and bias. Just as in the IQHE, exact filling occurs at only a discrete set of magnetic fields corresponding roughly to the centers of the observed plateaus; even slightly away from these points, the presence of extra electrons or extra flux quanta leads to the occupation of excited states. Even at exact filling, excited states may be thermally populated, particularly for weaker states, which may have energy gaps on the order of 500 mK or less. Finally, even

at exact filling and zero temperature, electronic transport measurements require injecting electrons into the 2DEG. The injected electrons will excite the system out of its ground state, and so an understanding of electron transport in the FQH regime requires an understanding of its excitations. These properties can be derived using a variety of arguments; here we review the basic results.

Fractional charge

Originally predicted by Laughlin [25], the notion that excitations of FQH states should carry fractional charge was generalized with the development of the CF model, through which the remarkably simple and general result can be derived that for any $\nu = r/s$ described by the CF model, the quasi-particle excitations carry a local charge of $e^* = e/s$ [12]. A more complicated analysis is needed for $\nu = 5/2$ since the CF model does not directly apply, but the most common prediction, arising from the Pfaffian and a few other possible wavefunctions, is for a charge of $e^* = e/4$.

At "Laughlin-like" filling factors, i.e. $\nu = 1/s$, fractional charges consistent with the Laughlin/CF-model prediction have been measured using several techniques including shot noise [38, 39, 40], anti-dots [41], and local compressibility measurements [42]. At other filling factors, including 5/2, shot-noise measurements have yielded more complicated results [43, 44, 45], interpreted as an effective bunching of FQH quasi-particles at low temperatures and low energies [46, 47], but recent measurements of local compressibility [36] have also observed a 3/4 ratio of e^* at $\nu = 5/2$ to that at $\nu = 7/3$, consistent with the Laughlin/CF prediction at 7/3 and the most commonly predicted value at 5/2. Measurements of zero-bias tunneling anomalies [35, 48] at these two filling factors also provide evidence for this conclusion.

Fractional braiding statistics

The familiar behavior of matter and force carriers in 3D is shaped by their exchange statistics, according to which they can be categorized as either fermions or bosons. That there are only two such possibilities comes from the fact that a double exchange of identical particles must leave the wavefunction unchanged, and so a single exchange can only multiply the wavefunction by a factor of $e^{i\theta}$ where $\theta = 0$ (bosons) or π (fermions). This restriction on exchange statistics remains valid in any number of dimensions, but in 2D another type of particle statistics can be conceived, known as braiding statistics. In 3D, braiding a particle in a complete circle around another one is not a well-defined notion, and any attempt at such an operation is effectively equivalent to a double exchange as far as particle statistics is concerned. In 2D, however, a circular trajectory enclosing another particle is topologically different from one not enclosing that particle. As a result, a complete braid is distinguishable from a double exchange, and moreover distinguishable from doing nothing: as a result, such an operation can in principle lead to arbitrary changes in the wavefunction.

Although there is plenty of theoretical and experimental evidence that composite fermions obey fermionic exchange statistics (as there had better be, given their name), the fact that they are partly composed of magnetic flux quanta suggests, by analogy with the Aharonov-Bohm effect (to be discussed in Section 1.3.1), that braiding one CF around another may lead to accumulation of a phase. In fact, it can be shown that for ν given by Equation 1.5, both CF quasi-particles and CF quasi-holes have a braiding statistics parameter of

$$\alpha = \frac{2p}{2pn \pm 1}, \tag{1.6}$$

defined such that a braiding operation multiplies the wavefunction by a phase $e^{i\alpha\pi}$. Since α can take on any real value, including fractional ones, this property is called either anyonic

or fractional braiding statistics. The details of the derivation and original references are presented in Chapter 9 of Jain's comprehensive book on composite fermion physics [12]. Although some researchers have claimed [49, 50] to have seen experimental evidence for fractional statistics (see Section 1.4), most agree that a clear observation has yet to be made.

Non-Abelian braiding statistics

An even more interesting type of braiding statistics, and one that could possibly be exploited to perform topological quantum computing [13], is predicted for systems in which braiding quasi-particles actually transforms the system among a subspace of degenerate ground states. This type of braiding statistics is called non-Abelian, since the unitary transformations resulting from braid operations in general do not commute. It would be an understatement to say that much of the interest in the 5/2 state arises from the possibility that its excitations obey non-Abelian statistics [51]. Proposed experiments to detect non-Abelian statistics in FQH systems are briefly discussed in Section 1.3.

Edge structure

While edge states in the IQH regime are believed to consist of single compressible strips, carrying excitations of charge e, that occur at the intersections of the Fermi level with the LL's (Section 1.2.4), FQH-regime edge states are generally believed to be much more complicated, with their properties depending on factors such as the magnetic field, the slope of the edge-confining potential [52, 53], and even disorder [54, 55]; in fact, disorder has been predicted to result in the formation of neutral modes, which transport a heat current instead of a charge current along the boundary of the FQH state. Neutral modes are also expected to be a critical component of any incompressible state at even-denominator

filling [30]. Being neutral, such modes are permitted to travel opposite to the direction of net charge transport, a property exploited by recent experiments in which the first experimental evidence for their existence has been reported [56, 57]. The possible effect of neutral modes on interferometry is discussed in Chapter 6.

1.2.6 Spin-related phenomena

As with the initial description of the IQHE, our treatment of the FQHE has so far ignored the spin degree of freedom. While the Zeeman energy is always much smaller than the cyclotron energy in GaAs, it can become significant compared to the energy gaps of many FQHE states, leading to competition between configurations with different degrees of spin polarization [58]. Interestingly, since the Zeeman energy is proportional to B while the Coulomb energy is proportional to $\sqrt{B}$, some filling factors can be either polarized or unpolarized depending on the field at which they occur. For example, at high enough magnetic fields, the $\nu = 2/3$ state can consist of two spin-up CF-LL's, but at lower fields (i.e. at lower electron densities), can have one spin-up and one spin-down CF-LL. At some intermediate field, the Zeeman and Coulomb effects are nearly equal and opposite in magnitude, resulting in a collapse of the FQH gap. Several experiments have demonstrated such transitions using either a tilted magnetic field (allowing the Zeeman energy to be increased while keeping the perpendicular field constant) or a 2DEG with a global back gate that allows the density to be varied [59, 33].

Spin-polarization measurements are of particular interest at the $\nu = 5/2$ state, since if this state is described by the Moore-Read wavefunction, then the electrons participating in the state must be spin-polarized. Although observation of spin polarization would not confirm that this wavefunction is the correct one, it would rule out others such as the (3,3,1) state [28], a wavefunction in which two components (here the spin-up and spin-down

subspaces) are each described by a Laughlin 1/3-like state, with additional correlations between the two subspaces. On the other hand, observation of unpolarized electrons at 5/2 would constitute strong evidence against the Moore-Read wavefunction, and consequently against the possibility of non-Abelian statistics at 5/2.

Experimentally, the observed collapse of the 5/2 state in a tilted magnetic field [60] appeared to suggest an unpolarized state. Ten years later, Morf [61] re-ignited interest in the problem by performing numerical calculations on systems of up to 18 particles indicating that a spin-polarized state should be favored at 5/2, and furthermore proposing an alternative explanation for the tilted-field results. Within two years, his theory received experimental support by measurements of the energy gap $\Delta_{5/2}$ as a function of magnetic field in a sample with tunable density, which showed no evidence of de-stabilization at fields as high as 10 T [62]. Most recently, an experiment in which the 2DEG spin polarization was measured via its Knight-shift effect on the NMR frequency of the ^{75}As nuclei in the lattice [37] also suggested a fully polarized state at 5/2. This result is not entirely convincing since the second-Landau-level electrons are measured to be fully polarized over the entire range $2 \leq \nu \leq 2.7$, a result that would also be expected in the absence of any FQHE-related effects, but it joins a growing body of experimental and numerical evidence suggestive of a spin-polarized state at 5/2.

Electron-lattice interactions

Electrons in high-mobility 2DEG's inherently have minimal interaction with the atoms in the GaAs/AlGaAs lattice. Their spins can interact with those of the lattice nuclei via the hyperfine interaction, but such electron-nuclear spin-flip scattering is usually suppressed by the mismatch in Zeeman energies of the electrons and the nuclei. Under certain conditions, however, interaction with nuclear spins can affect electron transport

significantly [58]. Despite the large magnetic fields used for these experiments, the nuclear spin polarization normally remains negligible thanks to the small nuclear Curie temperature. The nuclei are usually well isolated from not only the 2DEG but also each other, with the result that if a local polarization is somehow achieved, it can persist for a long time, often on the order of an hour. Transport effects that persist on such long timescales are therefore often indicative of phenomena involving nuclear spins.

As for how significant electron-nuclear interaction can be achieved given the aforementioned mismatch in energy scales, there are essentially two ways to do it: either provide the required energy by means of an external bias, or somehow make the energy scales match. Application of a bias can lead to a buildup of nuclear polarization in at least two ways: (a) by repeated excitation of electrons into a higher energy state with opposite spin, as seen in IQH-regime [63] and FQH-regime [64] breakdown experiments; and (b) spin-flip tunneling processes at quantum point contacts [65].

Finding a way to match the energy scales for electronic and nuclear spin flips seems at first like a less-likely way to foster electron-nuclear interaction than the above techniques, but it turns out that such behavior occurs naturally in the vicinity of $\nu = 1$. The gap at $\nu = 1$ is enhanced by a strong exchange interaction [66], which also leads to the creation of low-energy collective excitations called Skyrmions that are capable of interacting with nuclear spins [67]. Unlike those induced by an applied bias, this interaction does not lead to a buildup of polarization, but instead provides a channel for rapid depolarization, for which striking evidence has been observed [68].

1.3 Electron interferometry

Starting with Young's celebrated demonstration of the wave nature of light more than two centuries ago [69], and accelerating with the development of the Fabry-Perot [70] and Mach-Zehnder [71, 72] optical interferometers almost a century later, interferometry has been an immensely useful tool for studying a wide variety of systems. In the Fabry-Perot geometry, consisting of two beam-splitters in series, destructive interference suppresses forward transmission except at certain wavelengths determined by the distance between the beam-splitters and the angle of incidence. In the Mach-Zehnder geometry, light is split into two paths and then recombined; the relative phase between the two paths leads to either destructive or constructive interference.

With the invention of the quantum point contact (QPC) [73] and related devices, the tools were in place to perform similar interferometry experiments with electrons in 2DEG's. The earliest such experiment, fittingly enough, was a double-slit experiment analogous to Young's [74]. Even more robust interferometers can in principle be made by taking advantage of the "beams" of electrons formed by edge states in the quantum Hall regime: adjusting the gate voltages on a QPC allows the transmission and reflection of a single quantum Hall edge to be adjusted, effectively forming a tunable beam-splitter for electrons. Specifically, in exact analogy with the optical versions, an electronic Fabry-Perot interferometer [75] is a two-QPC device in which interference occurs between two or more trajectories reflected around the same loop different numbers of times (including zero), and an electronic Mach-Zehnder interferometer is a two-QPC device in which interference occurs between exactly two trajectories following separate paths [76].

Performing interferometry experiments with electrons is complicated by the fact that unlike photons, electrons interact with each other and with external electric and mag-

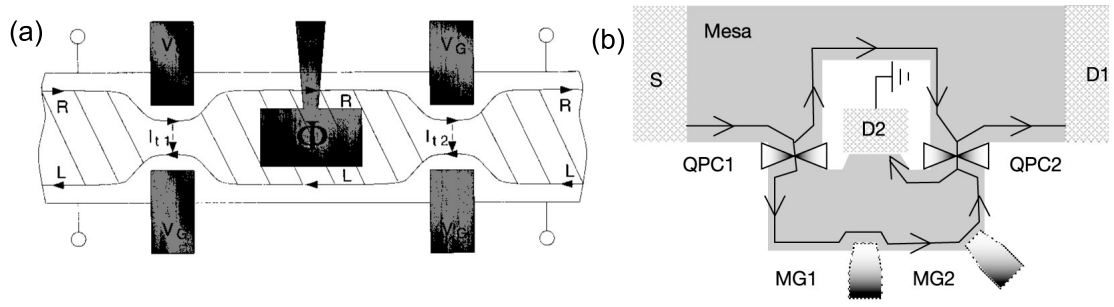

Figure 1.7: (a) Schematic electronic Fabry-Perot interferometer, adapted from [75]. (b) Schematic electronic Mach-Zehnder interferometer, adapted from [76].

netic fields in ways that affect their phase, but of course such effects are what make the experiments interesting. In both types of quantum-Hall-regime interferometers, factors potentially affecting the relative phase of the two paths include the Aharonov-Bohm effect, fractional and non-Abelian braiding staistics, decoherence, and Coulomb interactions. In addition, the possibility of effectively infinite reflection within the Fabry-Perot geometry opens the door to quantum-dot-like behavior [77]. These effects are presented briefly in the remainder of this section, and in more detail in several references [23, 75, 78, 79, 80, 81, 82]. Early implementations of electronic Fabry-Perot and Mach-Zehnder[2] interferometers are discussed in Section 1.4.2.

1.3.1 Aharonov-Bohm phases

In classical electromagnetism, all physical effects can be described in terms of the electric and magnetic fields. The electric scalar potential V and the magnetic vector potential $\vec{A}$ play no direct role. In quantum mechanics, on the other hand, these potentials directly affect the phase a particle accumulates while traveling along any path. In particular,

[2]The experiments presented in this thesis focus on the Fabry-Perot geometry, but some of the results have interesting connections to experiments in the Mach-Zehnder geometry, so theoretical and experimental aspects of both geometries will be discussed to the extent that they are relevant.

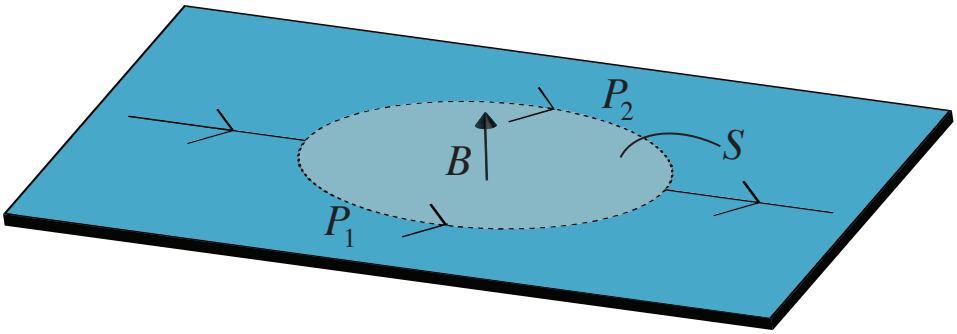

Figure 1.8: The Aharonov-Bohm effect occurs when two possible trajectories enclose magnetic flux, leading to a relative phase difference between them.

a particle of charge q traveling along a path P accumulates a phase

$$\phi = \frac{q}{\hbar}\int_P \vec{A}\cdot dP. \tag{1.7}$$

Given two possible trajectories P_1 and P_2 that enclose a region of non-zero B, as illustrated in Figure 1.8, the difference in phase accumulated along each trajectory is given by

$$\Delta\phi = \frac{q}{\hbar}\int_{P1-P2} \vec{A}\cdot d(P_1 - P_2). \tag{1.8}$$

Note that although the trajectories themselves may lie entirely in a region in which $B = 0$, the enclosed field will result in a finite $\vec{A}$ along both trajectories. Since the sum of the two trajectories defines a loop enclosing a surface S, Stokes's Theorem allows the line integral of $\vec{A}$ to be transformed into a surface integral of $\Delta \times \vec{A}$ over S. In the simplest and most common case, that of a uniform magnetic field, the integration becomes trivial and gives

$$\Delta\phi = \frac{q}{\hbar}B\cdot S. \tag{1.9}$$

Although this effect is most notable for the direct action of $\vec{A}$ even in a region where $B = 0$, in practice a uniform magnetic field is usually used since it is much easier to produce and does not change the result. This effect can in principle be observed in both Fabry-Perot

and Mach-Zehnder interferometers in the quantum Hall regime: in both cases, it should lead to resistance oscillations as a function of magnetic field, with a period corresponding to one flux quantum (ϕ_0) through the device area when the interfering particles are electrons. When the interfering particles are quasi-particles with fractional charge e/s, the magnetic field period would simply be multiplied by a factor of s if not for the effect of statistical phases to be discussed in the next section[3]. Since the enclosed flux depends not only on B but also on the device area, AB oscillations also appear as a function of gate voltages that couple to the area. Since this coupling is roughly linear and does not depend on magnetic field, but the number of flux quanta per area increases with field, one expects gate-voltage periods to scale as $V_{\text{gate}} = 1/B$ for electron interference. For quasi-particles, the gate-voltage period would again be multiplied by a factor of s if not for the effect of statistical phases.

1.3.2 Statistical phases

As discussed in Section 1.2.5, the current-carrying quasi-particles associated with all FQH states not only have fractional charge but are also expected to obey fractional braiding statistics. Since such quasi-particles travel along FQH edge states and may also be localized in the bulk of the 2DEG, interferometry experiments with FQH edges should be sensitive to the phase accumulated when one such particle is braided around another. The experimental signatures are complicated by the fact that changes in the number of bulk quasi-particles localized within the interferometer, which lead to discrete shifts in the relative phase of the two interfering paths, are likely to occur as the magnetic field and gate voltages are changed, and possibly randomly on an unknown timescale depending on

[3]Such a result would be in contradiction to the Byers-Yang theorem [83], according to which all properties of a system must be periodic in ϕ_0 in order to satisfy gauge invariance.

the strength of the coupling between the interior of the interferometer, the edges, and the leads [84]. Even neglecting the possibly of random changes in the number of enclosed quasi-particles, the exact behavior is expected to depend on electrostatic details [75]. In general, however, the most robust signatures of fractional statistics would be regular, discrete phase shifts in the interference pattern that could be associated with expected changes in the number of enclosed quasi-particles.

In principle, the signatures of non-Abelian statistics should be clearer than those of Abelian statistics: in the Fabry-Perot interferometer, for example, oscillations are expected to alternately appear and vanish as the parity of the number of enclosed quasi-particles is changed from even to odd and back [79]. In real systems, however, these effects could also be spoiled by instability in the number of enclosed particles [85] or mimicked by other phenomena [81].

1.3.3 Dephasing effects

Any process that relies on quantum superposition may be affected by decoherence: if interaction with the environment leads to an effective measurement of the state of the quantum system (e.g. the path traveled by an electron), then the quantum behavior will be washed out. For example, consider an electron in a two-path interferometer as illustrated in Figure 1.8, and suppose there is a nearby impurity that has a non-zero probability of scattering an electron traveling along either path. If the impurity has no degrees of freedom, then even if an interaction does occur, it has no way of "recording" the path taken by the electron, and therefore cannot lead to decoherence. If the impurity does have degrees of freedom (e.g. spin) that can interact with the passing electron, then it may lead to decoherence, but only if the result of the interaction is sensitive to the path taken by the electron; in particular, long-wavelength phonons should not contribute significantly

to decoherence [86]. As a result, the main source of decoherence in GaAs 2DEG's at low temperatures is expected to be electron-electron interactions, which also become suppressed in the zero-temperature, zero-bias limit [74].

In the context of quantum-Hall-regime Fabry-Perot interferometry, one might naively expect that strong interference signals should be easily visible given the long mean free path of edge-state electrons and low 2DEG temperatures. The fact that the interference amplitudes have turned out to be lower than one might have naively expected is addressed in several places throughout this thesis: Sections 3.3 and 5.4 present relevant experimental results, and Chapter 6 offers additional discussion and more suggestive data.

1.3.4 Coulomb effects

The geometry of an electronic Fabry-Perot interferometer resembles that of a quantum dot [77], in which the most prominent feature in electron transport is the Coulomb blockade effect arising from the modulation of tunneling through the dot by its large charging energy. Although electronic Fabry-Perot interferometers typically operate with larger conductances than Coulomb-blockaded quantum dots, much of this extra conductance comes from fully transmitted edge states, which may couple only weakly to the inner region of the interferometer. As a result, charging effects might be expected to affect transport[4]. A naive analogy with Coulomb-blockaded quantum dots would suggest that charging physics in a Fabry-Perot interferometer might manifest itself in the form of resistance oscillations as a function of gate voltage, but would not lead to any periodic behavior as a function of magnetic field. Further analysis, however, reveals that in the presence of fully transmitted edge states, the corresponding LL's can act as additional gates whose effective voltage de-

[4]In the Mach-Zehnder geometry, on the other hand, the enclosed area is much larger, in fact large enough to enclose a drain contact, and so the charging energy is negligible.

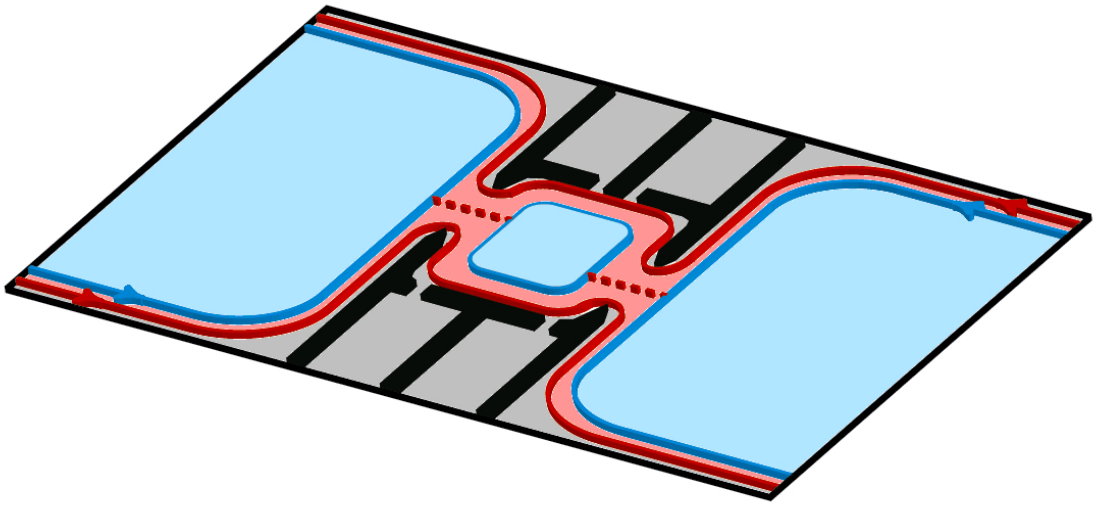

Figure 1.9: The origin of Coulomb-dominated oscillations is easiest to understand in the strong backscattering regime, where transport through the interferometer is mediated by an island of charge tunnel-coupled to each lead.

pends on the magnetic field [87, 82]. This phenomenon, now known as Coulomb-dominated (CD) interference, mimics oscillations arising from pure Aharonov-Bohm (AB) interference but has different detailed behavior (most dramatically, an opposite sign of the slope of constant-phase lines when resistance is measured in the plane of gate voltage and magnetic field; see Chapter 2).

Although the thorough combined analysis of AB and CD interference performed by Halperin et al. [82] is quite general, the effect of the Coulomb interaction is most easily explained in the case where transmission through the constrictions occurs via weak forward tunneling, leading to the creation of a well-defined island of charge within the interferometer as shown in Figure 1.9. This explanation is presented for the IQH regime, following Rosenow et al. [87], in Chapter 2. The generalization to the FQH regime, following Halperin et al. [82], is presented in Chapter 5. Moreover, as illustrated in more detail in Chapter 5 and discussed further in Chapter 6, the situation illustrated in Figure 1.9 corresponds to the regions of

filling factor where Coulomb-dominated oscillations are most readily observed.

1.4 Experimental context

These experiments are done in a vacuum in the literal sense, but not so in the figurative sense. Here I provide a summary of the prior and concurrent experimental work most relevant to the interferometry experiments presented in this thesis.

1.4.1 Experimental detection of electron interference

Before discussing experiments, it is worth understanding what is being measured. While changes in transmission resulting from optical interference are measured using photon detectors, changes in transmission resulting from electron interference lead to measurable changes in the resistance of the device. In the quantum Hall regime, the device resistance can be measured either longitudinally (R_{L}, analogous to R_{xx} but with the device between the voltage probes) or diagonally (R_{D}, analogous to R_{xy} but with the device between the voltage probes) [24]. The two measurements are in principle equivalent, related for a standard choice of contacts by $R_{\mathrm{D}} = R_{\mathrm{xy}} + R_{\mathrm{L}}$, but in practice, R_{D} has an advantage: with a clever arrangement of the voltage probes [88], R_{D} can be made to contain information only about transmission through the device up to a very good approximation, while R_{L} inherently includes a small but noticeable contribution from the bulk R_{xx}. As a result, we and most other experimental groups measure R_{D}. Interpretation of R_{D} in terms of edge-state transmission is simplified by the quite general observation that at most one edge state is ever partially transmitted, with all others being fully transmitted or fully reflected. In the FQH regime, however, interpretation can be complicated by the fact that the conductance of each edge state depends on which other edge states are present, which may not always be clear. Fortunately, as illustrated in Chapter 5, the identity of the unknown edges appears

to be of minimal relevance to interpreting our results.

A primary disadvantage of the ambiguities inherent in interpreting R_{D} in the FQH regime is that different groups have developed different and conflicting terminologies, making it difficult to discuss a series of experiments using coherent language. For simplicity, therefore, in the remainder of this section I will use ν to refer to the filling factor whose physics is being probed by the measurement being discussed, and likewise will use the terms IQH-regime and FQH-regime interferometry to refer to measurements designed to probe the physics of those respective regimes.

1.4.2 Previous work

Fabry-Perot interferometry

The observation of Aharonov-Bohm-like oscillations in electronic Fabry-Perot interferometers dates back to 1989 [89]. In this and other early experiments [90, 91, 92], the behavior of the magnetic-field and gate-voltage periods was not consistent with single-particle AB interference, but the exact role of Coulomb interactions and the underlying LL's in producing the observed results was not yet appreciated. The first reported Fabry-Perot interferometry measurement in the FQH regime [93, 94] was difficult to interpret: not only was the IQH-regime understanding of such devices still incomplete, but the observed behavior in that experiment appeared to violate the Byers-Yang theorem [83], and the proposed interpretation relied on a seemingly unlikely fine-tuning of filling factors [95, 87][5]. A follow-up experiment from the same group [49], performed in a simpler regime, yielded a

[5]Based on the occasional observation of similar behavior (namely oscillations with a surprisingly large magnetic-field period) in my own devices, as well as a recent experiment demonstrating AFM imaging of similar behavior in the IQH regime [96], I believe the most likely explanation for this result is resonant tunneling through an unintentional localized state at one of the constrictions. This hypothesis could be tested by comparing the oscillation periods with respect to the different gates defining the device: for a constriction resonance, the periods with respect to adjacent gates would be much smaller than for gates near the opposite constriction.

less surprising result: the magnetic field period at $\nu = 1/3$ matched that at $\nu = 1$, and the gate-voltage period was reduced by a factor of 3. This experiment was again interpreted by its authors as evidence of fractional statistics, but still the lack of a complete understanding of the system prevented other, potentially more likely effects from being ruled out.[6]

Mach-Zehnder interferometry

The first electronic Mach-Zehnder interferometry experiment was not reported until fairly recently [76]. The Mach-Zehnder is a technically more difficult device to fabricate than the Fabry-Perot, requiring a micron-scale ohmic contact in the center of the device and an air-bridge to connect this ohmic to a pad large enough to be contacted via wire-bonding. The necessarily large area of the interference loop leads to a very small magnetic field period for AB oscillations, requiring that the magnetic field be swept extremely slowly in order to observe them. These circumstances may partially explain the apparent late realization of the Mach-Zehnder relative to that of the Fabry-Perot, but considering that AB interference of non-interacting electrons was not observed in a Fabry-Perot prior to the work of Chapter 2, it may be more appropriate to ask why the observation of such behavior took so long in either geometry. This subject will be taken up in Chapter 6.

Subsequent Mach-Zehnder experiments revealed a surprising checkerboard-like pattern of oscillations as a function of dc bias and magnetic field [97, 98, 99]. Interestingly, we observe similar patterns in Fabry-Perot interferometers (Chapter 3), but their dependence on magnetic field and other parameters differs significantly from that seen in Mach-Zehnders. Another difference is that in the Fabry-Perot geometry, this pattern arises in a single-particle picture [75], but in the Mach-Zehnder it appears to arise from electron

[6]Based on subsequent experimental and theoretical work, it seems likely that this result was actually the first published instance of CD oscillations at $\nu = 1/3$, in which case it would constitute a measurement of fractional charge but not statistics.

interactions [100, 101, 102], an ironic twist since the geometry of the Fabry-Perot tends to be much more conductive to Coulomb effects than that of the Mach-Zehnder. Despite these differences, and to some extent because of them, the checkerboard patterns and their interpretations serve to highlight some of the similarities and differences between the two geometries.

1.4.3 Progress achieved by these experiments

The experiments presented in this thesis explore a number of factors related to Fabry-Perot interferometry in quantum Hall systems. Beginning in the integer quantum Hall regime, evidence clarifying the role of Coulomb interactions is uncovered (Section 2.3), and the first clear demonstration of behavior consistent with AB interference of non-interacting particles is presented (Section 2.4). This phenomenon is used to measure the magnetic-field dependence of edge-state velocities and coherence times (Chapter 3). Moving to the fractional quantum Hall regime, spin-flip interactions between 2DEG electrons and lattice nuclei are seen to have dramatic effects on transport in micron-scale devices (Chapter 4). In addition to providing additional evidence for the relevance of the CF model, this behavior may be used to shed light on the spin polarization of various FQH states, and could affect interference measurements as discussed in Section 4.7. Coulomb-dominated interference in the FQH regime, previously observed only at $\nu = 1/3$, is observed for the first time at several FQH states (Chapter 5), providing the first reported measurement of the quasi-particle charge at 4/3 and 5/3. The temperature dependence data presented near the end of Chapter 5 and in Chapter 6 shed light on factors limiting the amplitude of the oscillations and possibly hinting at ways to observe them at more filling factors, including $\nu = 5/2$.

1.4.4 Concurrent progress

Concurrent with the experimental work presented in this thesis, other groups also published related results. This section describes the main results and their relationship to the work presented here.

Fabry-Perot interferometry: IQH regime

In the IQH regime, data comparable to our CD oscillations were also recently published by the Kang [103], Goldman [104], and Heiblum [105] groups, in the latter two cases including a 2D plot confirming the CD nature of the oscillations. Ofek et al. [105] also reproduced our observation of pure AB oscillations in a large top-gated interferometer, as well as that of simultaneous AB and CD oscillations a small device[7]. Pure AB oscillations in a small device have been claimed by Willett et al. [106], but limited data has been published, and in particular no 2D plot verifying the AB nature of the oscillations. Not only is the reported absence of CD oscillations at any filling factor surprising, but so is the presence of AB oscillations in a device with such large (1 μm) constrictions: we never see AB oscillations in devices with constrictions larger than about 500 nm, nor has any other group published such an observation.

Fabry-Perot interferometry: FQH regime

The first clear FQH-regime CD oscillations were demonstrated by Ofek et al. [105] at $\nu = 1/3$; the magnetic-field and gate-voltage period scaling in this experiment was comparable to that found by Camino et al. in 2007 (see Section 1.4.2), but Ofek et al. also included a 2D plot verifying the CD nature of the oscillations. Additional CD oscillations

[7]The simultaneous AB and CD oscillations evident in Figure 7 of Ofek et al. were not identified as such at the time, and our observation of simultaneous AB and CD has not been previously published; see Chapter 6 for examples of simultaneous AB and CD oscillations.

have been claimed by An et al. [50] near $\nu = 7/3$ and $\nu = 5/2$, but the lack of plateaus at these filling factors and the unexplained scaling of the gate-voltage periods suggest the possibility of resonance-like behavior similar to that discussed in Footnote 5. Finally, AB oscillations have been claimed near $\nu = 5/2$ by Willett et al. [107, 106], but the lack of 2D plots, the poorly defined periods evident from the FFT's, and the heavy filtering and processing of the data make it difficult to draw any firm conclusions from these results.

Mach-Zehnder interferometry

Recent Mach-Zehnder interferometry experiments have focused on the study of dephasing mechanisms in the IQH regime [108, 109, 110]. Despite the large IQH-regime visibilities, no oscillations have been reported at any FQH states, even robust ones with relatively simple edges such as $\nu = 1/3$. Although surprising, this result is consistent with the lack of clear signatures of pure AB interference associated with any FQH states in the Fabry-Perot geometry. As experimental and theoretical work continues to clarify the mechanisms limiting visibility in both geometries, it seems likely that the reason for the absence of this much-sought phenomenon will be understood and eventually—God willing—overcome.

Chapter 2

Distinct signatures for Coulomb blockade and Aharonov-Bohm interference in electronic Fabry-Perot interferometers

Yiming Zhang, D. T. McClure, E. M. Levenson-Falk, C. M. Marcus
Department of Physics, Harvard University, Cambridge, Massachusetts 02138, USA
L. N. Pfeiffer, K. W. West
Alcatel-Lucent, Murray Hill, New Jersey 07974, USA

Two distinct types of magnetoresistance oscillations are observed in two electronic Fabry-Perot interferometers of different sizes in the integer quantum Hall regime. Measuring these oscillations as a function of magnetic field and gate voltages, we describe three signatures that distinguish the two types. The oscillations observed in a 2.0 μm^2 device are understood to arise from a Coulomb blockade mechanism, and those observed in an 18 μm^2 device from an Aharonov-Bohm mechanism. This work clarifies, provides ways to distinguish, and demonstrates control over these distinct mechanisms of oscillations seen in electronic Fabry-Perot interferometers.[1]

[1]This chapter is adapted with permission from Phys. Rev. B **79**, 241304 (2009).

2.1 Introduction

Mesoscopic electronics can exhibit wave-like interference effects [111, 112, 76, 99], particle-like charging effects [77], or a complex mix of both [113]. Experiments over the past two decades have investigated the competition between wave and particle properties [114], as well as regimes where they coexist [115, 116, 117, 113]. The electronic Fabry-Perot interferometer (FPI)—a planar two-contact quantum dot operating in the quantum Hall regime—is a system where both interference and Coulomb interactions can play important roles. This device has attracted particular interest recently due to predicted signatures of fractional [75] and non-Abelian [79, 118, 119] statistics. The interpretation of experiments, however, is subtle, and must account for the interplay of charging and interference effects in these coherent confined structures.

The pioneering experimental investigation of resistance oscillations in an electronic FPI [89] interpreted the oscillations in terms of an Aharonov-Bohm (AB) interference of edge states, attributing the magnetic field dependence of the field-oscillation period to a changing effective dot area. More recent experiments [91, 92, 120, 121, 103] have observed frequencies of integer multiples of the fundamental AB frequency; in particular, a proportionality of field frequency to the number of fully-occupied Landau levels (LL's) has been well established [122, 120, 121, 103] in devices up to a few μm^2 in size. Both experimental [90, 91, 120, 121, 103] and theoretical [122, 87, 123] investigations indicate that Coulomb interaction plays a critical role in these previously observed oscillations—as a function of both magnetic field and electrostatic gate voltage—suggesting an interpretation in terms of field- or gate-controlled Coulomb blockade (CB). The questions of whether it is even possible to observe resistance oscillations that arise from pure AB interference in FPI's, and if so, in what regime, and how to distinguish the two mechanisms, have yet to be answered

to our knowledge.

In this chapter, we report two different types of resistance oscillations as a function of perpendicular magnetic field, B, and gate voltage in FPI's of two different sizes. The type observed in the smaller (2.0 μm^2) device, similar to previous results [89, 90, 91, 92, 120, 121, 103], is consistent with the interacting CB interpretation, while that observed in the larger (18 μm^2) device is consistent with noninteracting AB interference. Specifically, three signatures that distinguish the two types of oscillations are presented: The magnetic field period is inversely proportional to the number of fully occupied LL's for CB, but field-independent for AB; The gate-voltage period is field-independent for CB, but inversely proportional to B for AB; Resistance stripes in the two-dimensional plane of B and gate voltage have a positive (negative) slope in the CB (AB) regime.

2.2 Devices and measurement

The devices were fabricated on a high-mobility two-dimensional electron gas (2DEG) residing in a 30 nm wide GaAs/AlGaAs quantum well 200 nm below the chip surface, with Si δ-doping layers 100 nm below and above the quantum well. The mobility is $\sim 2,000$ m^2/Vs measured in the dark, and the density is 2.6×10^{15} m^{-2}. Surface gates that define the FPI's are patterned using electron-beam lithography on wet-etched Hall bars [see Fig. 2.1(a)]. These gates come in from top left and bottom right, converging near the middle of the Hall bar. Figures 2.1(b) and (c) show gate layouts for the 2.0 μm^2 and 18 μm^2 interferometers. All gate voltages except V_C are set around ~ -3 V (depletion occurs at ~ -1.6 V). Voltages, V_C, on the center gates are set near 0 V to allow fine tuning of density and area.

Measurements are made using a current bias $I = 400$ pA, with B oriented into the 2DEG plane as shown in Fig. 2.1(a). The diagonal resistance, $R_D \equiv dV_D/dI$ is related

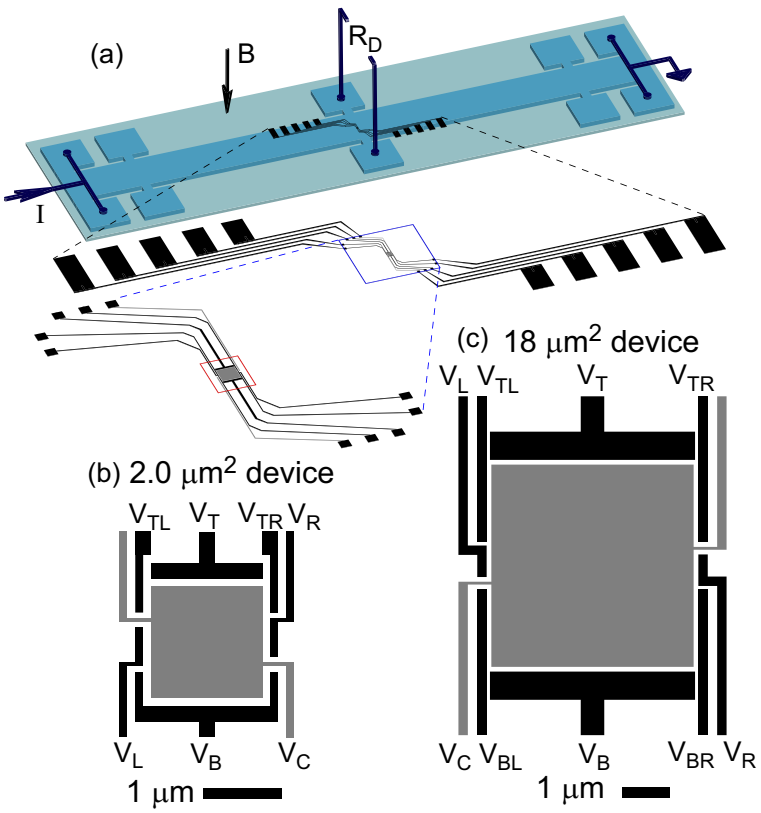

Figure 2.1: Measurement setup and devices. (a) Diagram of the wet-etched Hall bar, surface gates, and measurement configuration. Diagonal resistance, R_D, is measured directly across the Hall bar, with current bias, I. Subsequent zoom-ins of the surface gates are also shown; the red box encloses the detailed gate layouts for the device shown in (c). (b,c) Gate layouts for the 2.0 μm^2 and 18 μm^2 devices, respectively. The areas quoted refer to those under V_C.

to the dimensionless conductance of the device $g = (h/e^2)/R_D$ [88]. Here, V_D is the voltage difference between edge states entering from the top right and bottom left of the device.

2.3 Resistance oscillations in the 2.0 μm^2 device

Figure 2.2(a) shows R_D as a function of B measured in the 2.0 μm^2 device, displaying several quantized integer plateaus. Figures 2.2(b) and (c) show the zoom-ins below the $g = 1$ and 2 plateaus, respectively, displaying oscillations in R_D as a function of B, with

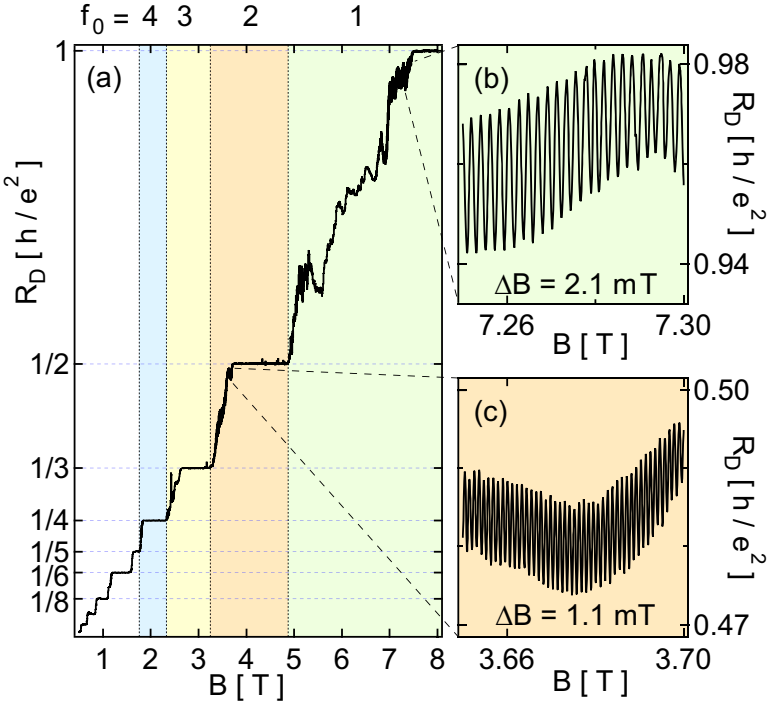

Figure 2.2: Oscillations in R_{D} as a function of magnetic field, B, for the 2.0 μm^2 device. (a) R_{D} as a function of B, showing well-quantized integer plateaus. Different colored backgrounds indicate different numbers of fully-occupied LL's, f_0, through the device. (b, c) Zoom-ins of the data in (a), at $f_0 = 1$ and 2, respectively, showing oscillations in R_{D}, and their B periods, ΔB.

periods $\Delta B = 2.1$ mT and 1.1 mT. This ΔB of 2.1 mT corresponds to one flux quantum, $\phi_0 \equiv h/e$, through an area $A = 2.0$ μm^2, which matches the device design; hence 1.1 mT corresponds to $\phi_0/2$ through about the same area. This is indeed the field-period scaling observed previously [89, 120, 121, 103], where for f_0 number of fully occupied LL's in the constrictions, ΔB is expected to be given by $(\phi_0/A)/f_0$. Thus, in Fig. 2.3(a) we show ΔB at each $1/f_0$, and a linear fit constrained through the origin, demonstrating the expected relationship.

We emphasize that this field-period scaling is inconsistent with simple AB oscillations, which would give a constant ΔB corresponding to one flux quantum through the area of the device. This can, however, be understood within an intuitive picture presented

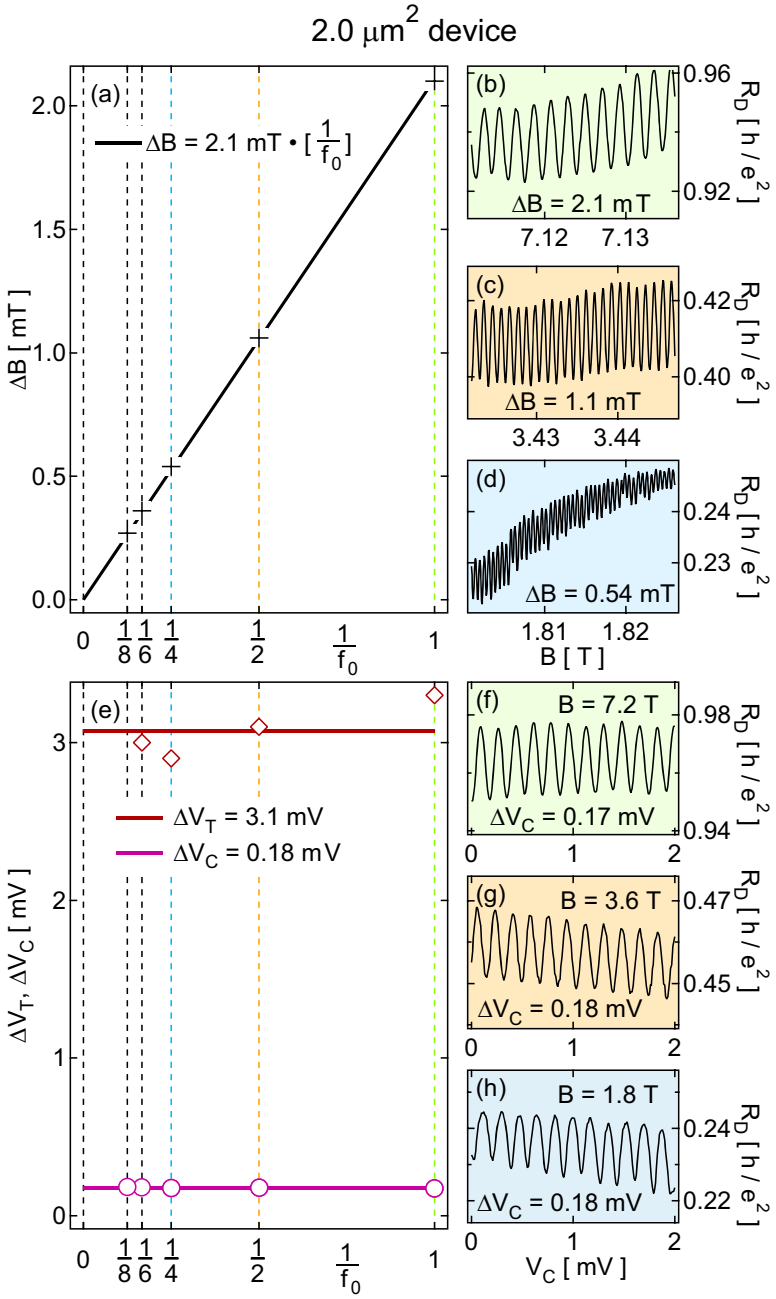

Figure 2.3: Magnetic field and gate voltage periods at various f_0, for the 2.0 μm^2 device. (a) ΔB as a function of $1/f_0$, and a best-fit line constrained through the origin. (b-d) $R_{\rm D}$ oscillations as a function of B, at $f_0 = 1$, 2, and 4, respectively. (e) $\Delta V_{\rm T}$ (diamonds) and $\Delta V_{\rm C}$ (circles) as a function of $1/f_0$, and their averages indicated by horizontal lines. (f-h) $R_{\rm D}$ oscillations as a function of $V_{\rm C}$, at $f_0 = 1$, 2, and 4, respectively.

in a recent theoretical analysis [87] that considers a dominant Coulomb interaction within the device. In this picture, on the riser of $R_{\rm D}$ where $f_0 < g < f_0 + 1$, the $(f_0 + 1)^{\rm th}$ and higher LL's will form a quasi-isolated island inside the device that will give rise to Coulomb blockade effects for sufficiently large charging energy,

$$E_{\rm C} = \frac{1}{2C}(ef_0 \cdot BA/\phi_0 + eN - C_{\rm g}V_{\rm gate})^2, \tag{2.1}$$

where N is the number of electrons on the island, C is the total capacitance, and $C_{\rm g}$ is the capacitance between the gate and the dot. The magnetic field couples electrostatically to the island through the underlying LL's: when B increases by ϕ_0/A, the number of electrons in each of the f_0 underlying LL's will increase by one. These LL's will act as gates to the isolated island: Coulomb repulsion favors a constant total electron number inside the device, so N will decrease by f_0 for every ϕ_0/A change in B, giving rise to f_0 resistance oscillations.

Further evidence for the CB mechanism in the 2.0 μm^2 device is found in the resistance oscillations as a function of gate voltages. Figures 2.3(f-h) show $R_{\rm D}$ as a function of center gate voltage $V_{\rm C}$, for $f_0 = 1$, 2 and 4, respectively. Figure 3(e) summarizes gate voltage periods $\Delta V_{\rm T}$ and $\Delta V_{\rm C}$ at various f_0, and shows they are independent of f_0. This behavior is consistent with the CB mechanism, because, as can be inferred from Eq. (2.1), gate-voltage periods are determined by the capacitance $C_{\rm g}$, which should be independent of f_0.

2.4 Resistance oscillations in the 18 μm^2 device

Having identified CB as the dominant mechanism[2] for resistance oscillations in the 2.0 μm^2 device, we fabricated and measured an 18 μm^2 device, an order of magnitude larger

[2]Although the existence of interference in small devices cannot be ruled out, we emphasize that Coulomb charging alone is sufficient to explain all data observed in small devices. A recent preprint (Ref. [104])

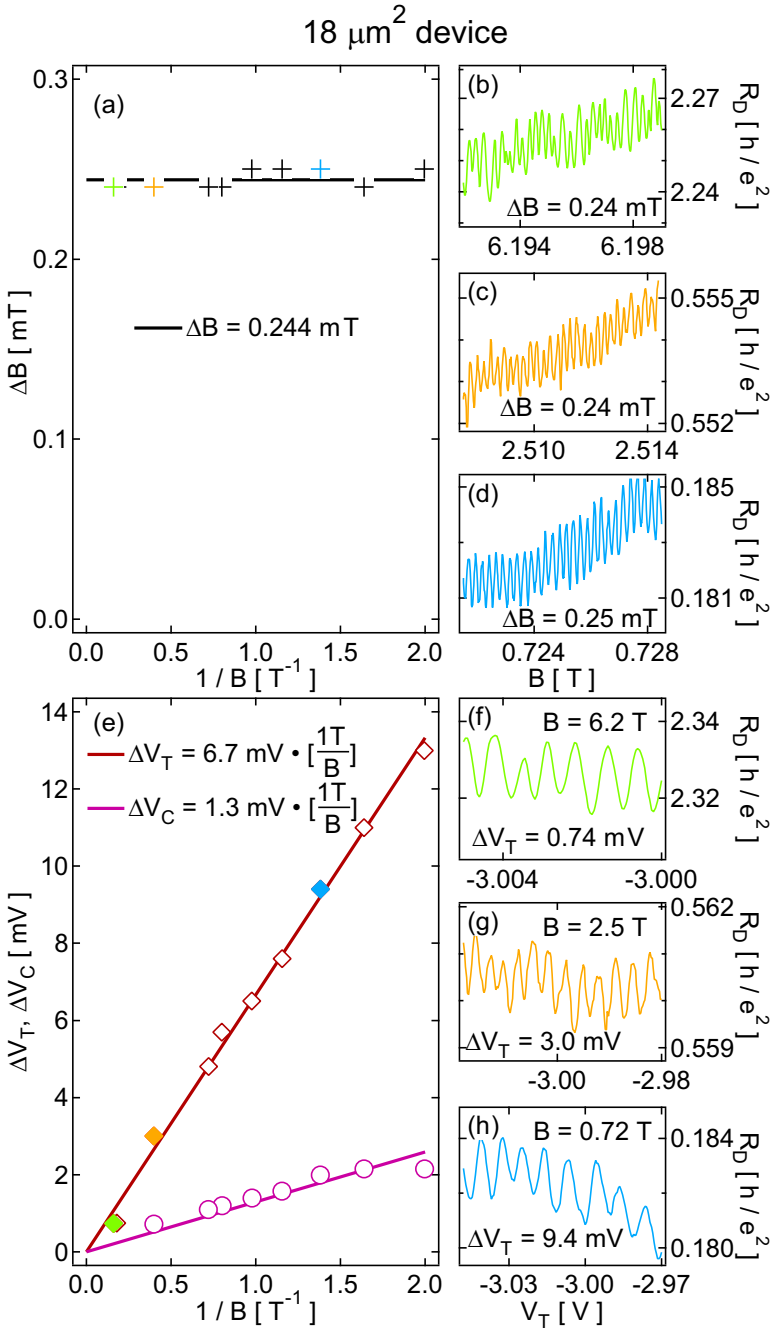

Figure 2.4: Magnetic field and gate voltage periods at various B, for the 18 μm^2 device. (a) ΔB as a function of $1/B$, and their average indicated by a horizontal line. (b-d) $R_{\rm D}$ oscillations as a function of B, over three magnetic field ranges. (e) $\Delta V_{\rm T}$ (diamonds) and $\Delta V_{\rm C}$ (circles) as a function of $1/B$, and best-fit lines constrained through the origin. (f-h) $R_{\rm D}$ oscillations as a function of $V_{\rm T}$, at $B = 6.2$ T, 2.5 T, and 0.72 T, respectively.

interprets magneto-oscillations in a small dot in terms of an interfering AB path, quantized to enclose an integer N. However, as will be seen in Fig. 2.4(e), gate voltage periods can change continuously by an order of magnitude in the AB regime, suggesting that N is not quantized in the AB regime.

in size, hence an order of magnitude smaller in charging energy. The center gate covering the whole device, not present in previous experiments [89, 90, 91, 92, 120, 121, 103], also serves to reduce the charging energy. In this device, R_D as a function of B at three different fields is plotted in Figs. 2.4(b-d), showing nearly constant ΔB. The summary of data in Fig. 2.4(a) shows that ΔB, measured at 10 different fields ranging from 0.5 to 6.2 T, is indeed independent of B; its average value of 0.244 mT corresponds to one ϕ_0 through an area of 17 μm^2, close to the designed area. This is in contrast to the behavior observed in the 2.0 μm^2 device, and is consistent with simple AB interference. Gate voltage periods are also studied, as has been done in the 2.0 μm^2 device. Figures 2.4(f-h) show R_D as a function of V_T at three different fields, and Fig. 2.4(e) shows both ΔV_T and ΔV_C as a function of $1/B$. In contrast to the behavior observed in the 2.0 μm^2 device, ΔV_T and ΔV_C are no longer independent of B, but proportional to $1/B$. This behavior is consistent with AB interference, because the total flux is given by $\phi = B \cdot A$ and the flux period is always ϕ_0; assuming that the area changes linearly with gate voltage, gate-voltage periods would scale as $1/B$ for AB.

2.5 One more signature

As shown above, the magnetic field and gate voltage periods have qualitatively different B dependence in the 2.0 μm^2 and 18 μm^2 devices, the former consistent with CB, and the latter consistent with AB interference. Based on these physical pictures, one can make another prediction in which these two mechanisms will lead to opposite behaviors. In the CB case, increasing B increases the electron number in the underlying LL's, thus reducing the electron number in the isolated island via Coulomb repulsion. This is equivalent to applying more negative gate voltage to the device. On the other hand, for the AB case,

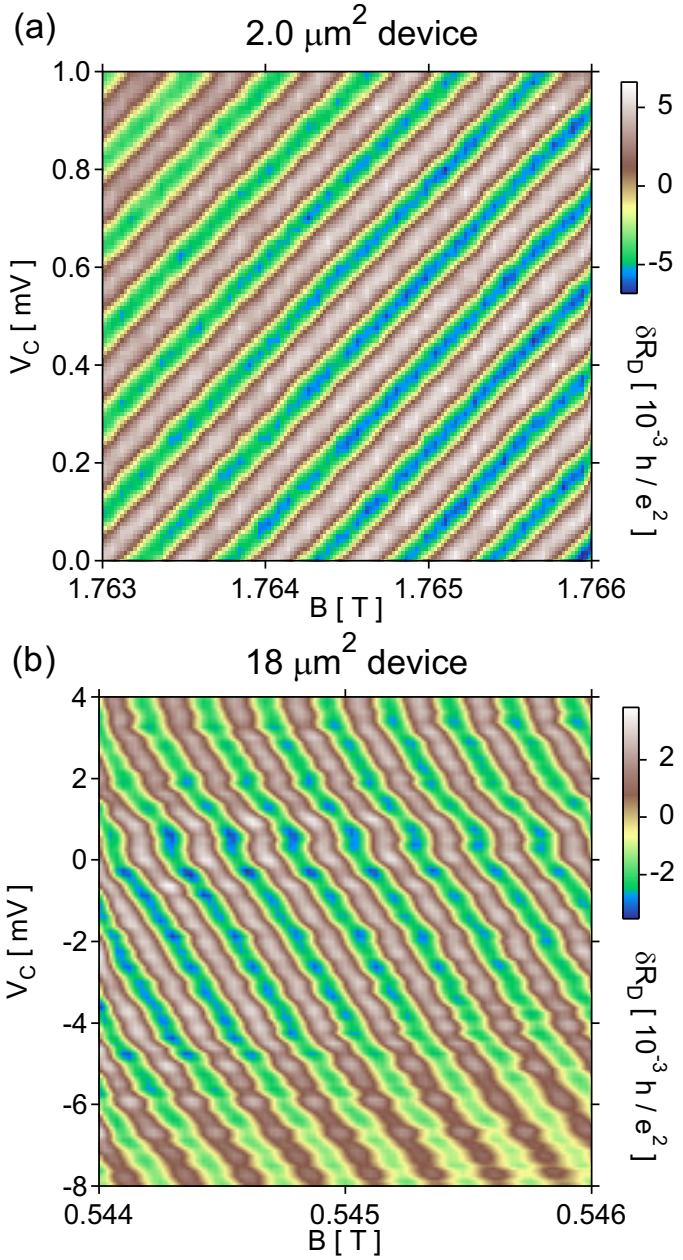

Figure 2.5: (a) $\delta R_{\rm D}$, i.e. $R_{\rm D}$ with a smooth background subtracted, as a function of B and $V_{\rm C}$, for the 2.0 μm^2 device. (b) Same as in (a), but for the 18 μm^2 device.

increasing B increases the total flux through the interferometer, and applying more positive gate voltage increases the area, thus also the total flux; therefore, higher B is equivalent to more positive gate voltage. As a result, if $R_{\rm D}$ is plotted in a plane of gate voltage and B,

we expect stripes with a positive slope in the CB case and a negative slope in the AB case.

Figures 2.5(a,b) show R_{D} as a function of V_{C} and B for the 2.0 $\mu\mathrm{m}^2$ and 18 $\mu\mathrm{m}^2$ devices, respectively. As anticipated, the stripes from the 2.0 $\mu\mathrm{m}^2$ device have a positive slope, consistent with the CB mechanism, while stripes from the 18 $\mu\mathrm{m}^2$ device have a negative slope, consistent with AB interference. This difference can serve to determine the origin of resistance oscillations without the need to change magnetic field significantly.

2.6 Discussion

The three distinct signatures that we observe between CB and AB interference in this work can also shed light on some of the previous experiments and their interpretations. A few recent experiments studying fractional charge and statistics in FPI's [94, 93, 49, 107] interpret resistance oscillations as arising from AB interference while taking each gate-voltage period as indicating a change of a quantized charge. However, as shown in Fig. 2.4(e), the gate voltage periods observed in the big device change by more than an order of magnitude over the field range that we study, and are inversely proportional to $1/B$, suggesting that charge is not quantized in the AB regime. Also in Ref. [49], the authors have observed that the magnetic field period stay constant between filling factor 1 and 1/3, but the gate voltage period at filling factor 1/3 is only 1/3 the size at filling factor 1. Although these observations can be interpreted as a result of fractional statistics, as the authors have done, there are at least two other possible interpretations: integer AB interference and CB with a charge of $e/3$. We consider clear identification of the mechanisms leading to oscillations—for instance using the method of Fig. 2.5—to be crucial for interpreting future experiments, particularly as the quantum states under investigation become more subtle.

2.7 Acknowledgments

We acknowledge J. B. Miller for device fabrication and discussion, R. Heeres for his work on the cryostat, and I. P. Radu, M. A. Kastner, B. Rosenow, N. Ofek, I. Neder and B. I. Halperin for helpful discussions. This research is supported in part by Microsoft Corporation Project Q, IBM, NSF (DMR-0501796), and the Center for Nanoscale Systems at Harvard University.

2.8 Epilogue

One piece of evidence that Coulomb interaction plays an important role in producing the observed "CB" oscillations (subsequently referred to as CD oscillations to distinguish them from true CB oscillations) is the fact that this behavior only appears in small devices. On the other hand, there was no reason to suspect that a small device, if tuned properly, would not also be capable of demonstrating pure AB interference. In the large device, AB interference was seen only when the constrictions were quite pinched off, leading to a significantly smaller filling factor in the constrictions than in the bulk. In the small device, the constrictions were never pinched off to such an extent since the CD oscillations appeared with the constrictions less pinched off. In subsequent experiments, however, we operated small devices with the constrictions more pinched off, and found both AB and CD oscillations to be possible (even simultaneously!) under those conditions, as shown in Chapter 6.

Chapter 3

Edge-state velocity and coherence in a quantum Hall Fabry-Perot interferometer

D. T. McClure[†], Yiming Zhang[†], B. Rosenow[†‡], E. M. Levenson-Falk[†], C. M. Marcus[†]
[†]*Department of Physics, Harvard University, Cambridge, Massachusetts 02138, USA*
[‡]*Max-Planck-Institute for Solid State Research, Heisenbergstr. 1, D-70569 Stuttgart, Germany*
L. N. Pfeiffer, K. W. West
Bell Laboratories, Alcatel-Lucent Technologies, Murray Hill, New Jersey 07974, USA

We investigate nonlinear transport in electronic Fabry-Perot interferometers in the integer quantum Hall regime. For interferometers sufficiently large that Coulomb blockade effects are absent, a checkerboard-like pattern of conductance oscillations as a function of dc bias and perpendicular magnetic field is observed. Edge-state velocities extracted from the checkerboard data are compared to model calculations and found to be consistent with a crossover from skipping orbits at low fields to $\vec{E} \times \vec{B}$ drift at high fields. Suppression of visibility as a function of bias and magnetic field is accounted for by including energy- and field-dependent dephasing of edge electrons.[1]

[1]This chapter is adapted with permission from Phys. Rev. Lett. **103**, 206806 (2009).

3.1 Introduction

The electronic Fabry-Perot interferometer (FPI), implemented as a quantum dot in the quantum Hall (QH) regime, has attracted theoretical [75, 118, 79, 87, 119] and experimental [93, 124, 49, 103, 107, 125] interest recently, especially in light of the possibility of observing fractional [75] or non-Abelian [79, 118, 119, 80] statistics in this geometry. Earlier experiments reveal that Coulomb [89, 90, 126] and Kondo [127, 128] physics can play important roles, as well. With such a rich spectrum of physics in these devices, a thorough understanding of the mechanisms governing transport even in the integer QH regime remains elusive.

While most work on electronic FPI's to date has focused on transport at zero dc bias, finite-bias measurements have proved to be a useful tool in understanding the physical mechanisms important in other interferometer geometries. In metallic [129] and semiconducting [130] rings interrupted by tunnel barriers, oscillations in transmission as a function of magnetic field and dc bias, forming a checkerboard pattern, have been observed. These features, attributed to the electrostatic Aharonov-Bohm (AB) effect [131, 132, 133], were used to measure the time of flight and dephasing in these devices. Similar checkerboard-like lobe structures have also been observed in Mach-Zehnder interferometers [97, 99, 109]. In that case, the pattern of oscillations is not readily explained within a single-particle picture and remains the subject of continued theoretical study [134, 100, 102, 101]. In electronic FPI's, conductance oscillations as a function of dc bias have been investigated theoretically [75] and provide a means of extracting the edge-state velocity from the period in dc bias. Edge-state velocity measurement without the use of high-bandwidth measurements [135, 136] will likely be useful in determining appropriate device parameters to probe exotic statistics beyond the integer regime. This approach was recently used [124] to mea-

sure the edge-state velocity at $\nu = 1/3$, though in a small ($\sim 1\ \mu\mathrm{m}^2$) device where Coulomb interactions, absent in the theory, may be expected to play a dominant role [103, 125].

In this Letter, we present measurements of finite-bias conductance oscillations in an 18 μm^2 electronic FPI whose zero-bias behavior is consistent with AB interference without significant Coulomb effects [125]. We find a checkerboard-like pattern of conductance oscillations as a function of dc bias and magnetic field, in agreement with the predictions of Chamon et al. [75]. Measuring the period in dc bias allows the velocity of the tunneling edge state to be extracted over a range of magnetic fields, yielding a low-field saturation consistent with a crossover from $\vec{E} \times \vec{B}$ drift to skipping orbits. High-bias fading in the checkerboard pattern is quantitatively consistent with a dephasing rate proportional to energy and magnetic field. Zero-bias oscillations in a 2 μm^2 device of similar design, where Coulomb effects are significant [125], do not evolve periodically with dc bias; instead, plots of conductance versus bias and magnetic field reveal diamond-like regions of blockaded transport in the weak-forward-tunneling regime that become more smeared out with stronger forward tunneling.

3.2 Devices and measurements

Devices are fabricated on GaAs/AlGaAs quantum-well structures with a two-dimensional electron gas (2DEG) of density $n = 2.7{\times}10^{15}$ m^{-2} and mobility $\mu = 2,000$ m^2/Vs located 200 nm below the surface. Hall bars are wet-etched as shown in Fig. 1(a), and metal surface gates are patterned by electron-beam lithography as in Fig. 1(b). Interferometers are defined by negative voltages (~ -3 V) applied to all gates except V_C, and samples are cooled in a dilution refrigerator to ~ 20 mK. A current bias I, consisting of a dc component of up to 30 nA and a 135-Hz component of 400 pA, gives rise to the diagonal voltage V_D

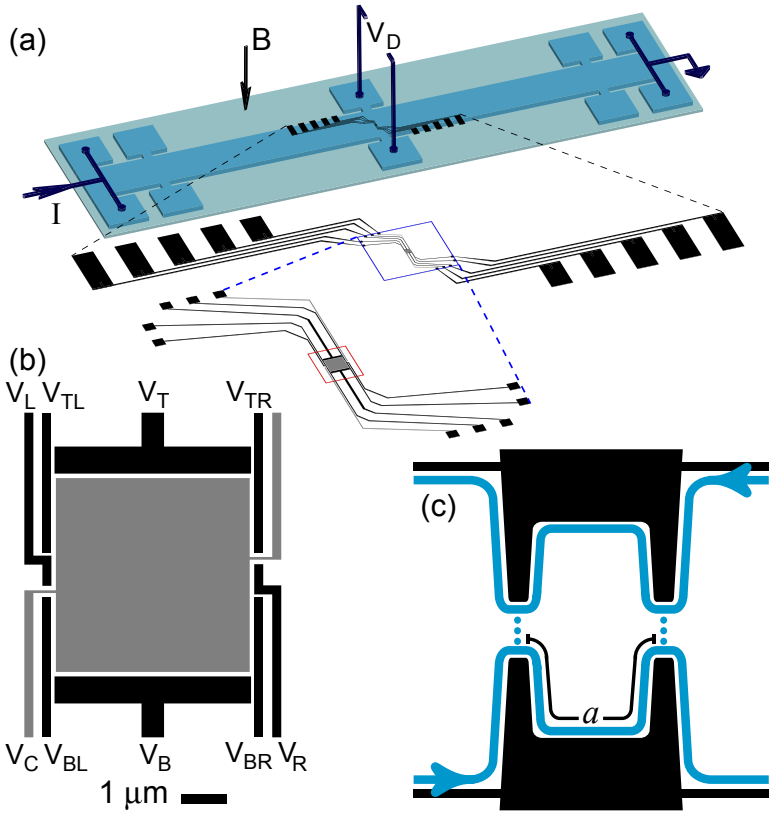

Figure 3.1: Measurement setup and the electronic Fabry-Perot device (a) With a current bias I applied at one end of the Hall bar, voltage V_{D} is measured directly across its width. Surface gates are shown in increasing detail, with a red box indicating the region shown in (b). (b) Gate layout of the 18 μm^2 device, which is operated as an interferometer by depleting all gates except V_{C}. (c) Schematic diagram of possible transmission paths through the device in the quantum Hall regime.

across the device, measured directly across the width of the Hall bar [Fig. 1(a)]. Lock-in measurements of diagonal conductance, $G_{\mathrm{D}} \equiv dI/dV_{\mathrm{D}}$, are used to study changes in interferometer transmission as a function of both V_{D} and perpendicular magnetic field B. As shown in Fig. 1(c), the current-carrying chiral edge states can be partially reflected at each constriction, leading to interference between the different possible trajectories as a function of the phase accumulated by encircling the interferometer.

3.3 Checkerboard pattern and interpretation

A typical measurement of G_{D} as a function of B and V_{D} in the 18 $\mu\mathrm{m}^2$ device is shown in Fig. 2(a). A checkerboard-like pattern of oscillations periodic in both B and V_{D} is observed, with reduced amplitude at high bias. A smoothly-varying background, most likely resulting from energy dependence of the tunnel rates at the constrictions, is also seen; to facilitate comparison to our model, which does not include this effect, we subtract this background, obtaining Fig. 2(b). Similar patterns are seen at fields $B = 0.22 - 1.26$ T; over this range the Landau level index, N, of the tunneling edge ranges from 4 to 1, but the field period of oscillations is always $\Delta B \approx 0.25$ mT, independent of both field and bias. Small gate-voltage adjustments of the relative tunnel rates at the two constrictions, used to maximize the overall amplitude of the oscillations at different fields, do not change the degree of bias dependence.

Magnetoconductance oscillations in this device reflect AB interference of partially transmitted edge states [125], with a phase shift $\Delta\varphi = 2\pi\Phi/\Phi_0$, where $\Phi = BA$ is the flux enclosed (in area A) by the interfering edge, and $\Phi_0 \equiv h/e$ is the magnetic flux quantum. The observed field period corresponds to $A \approx 17$ $\mu\mathrm{m}^2$, consistent with the dot area after subtracting a depletion length of roughly the 2DEG depth. The sinusoidal lineshape of the oscillations seen here suggests that coherent transport is dominated by two trajectories that differ in length by one traversal of the dot perimeter.

When a dc bias is added to V_{D}, an additional phase shift appears between interfering trajectories, associated with the energy-dependent wave vector of the contributing edge-state electrons; we will refer to this as the Fabry-Perot phase. The wave vector changes with energy as $\delta k = \delta\varepsilon/\hbar v$, where v denotes the edge-state velocity. Following the analysis of non-interacting electrons in Ref. [75], in which bias is assumed to affect mainly the chem-

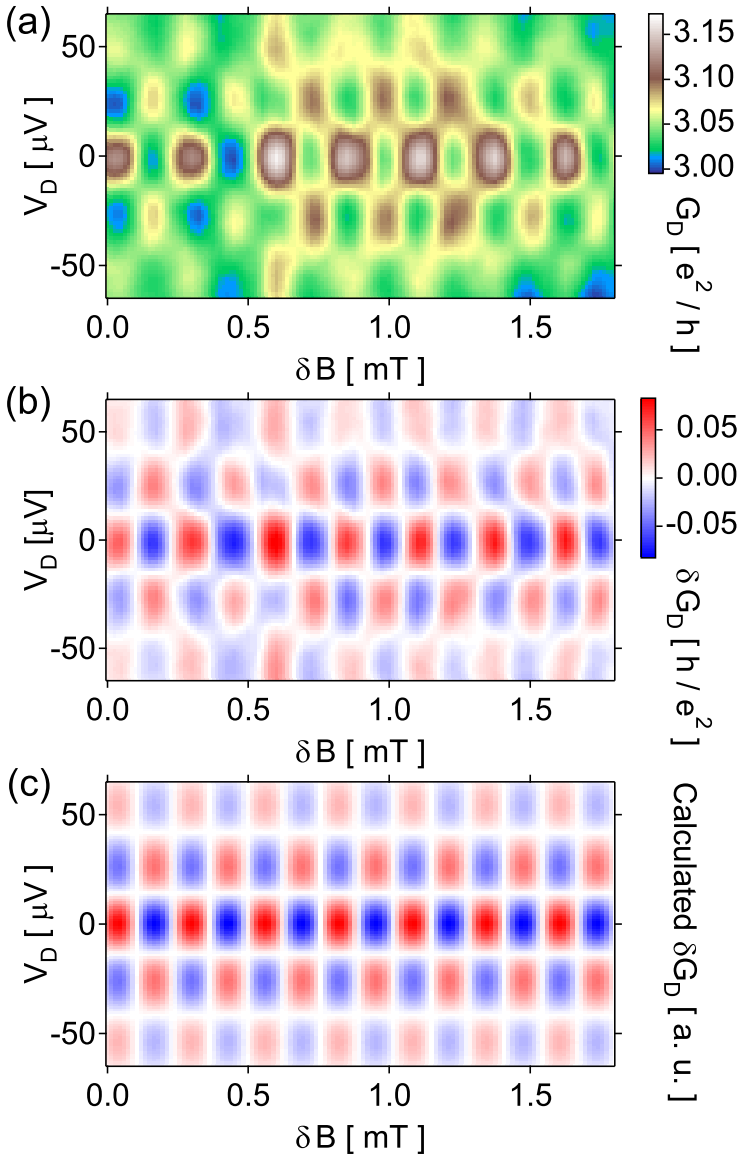

Figure 3.2: (a) G_{D} as a function of B and V_{D} in the 18 μm^2 device near $B = 0.47$ T. (b) Result of subtracting a smooth background from the data in (a). (c) δG_{D} calculated from Eq. (1), multiplied by the damping factor from Eq. (2), with $\Delta B = 0.25$ mT, $\Delta V_{\mathrm{D}} = 56$ μV, and $\alpha = 0.2$.

ical potential, we assign an additional relative phase $2a\varepsilon/\hbar v$ to an electron traversing the perimeter at energy ε above the zero bias Fermi level, where $a \sim 2\sqrt{A} = 8.2$ μm denotes the path length between constrictions [Fig. 1(c)]. For a symmetrically applied dc bias (relative

to the gate voltages), and neglecting contributions from multiply-reflected trajectories, the expected differential conductance has the form

$$\delta G_{\rm D}(\Phi, V_{\rm D}) = \delta G_0 \cos(2\pi\,\Phi/\Phi_0)\cos(eV_D a/v\hbar), \tag{3.1}$$

where the amplitude δG_0 does not depend on field or dc bias. Note that in this model, the contributions of AB and Fabry-Perot phase separate into a product of two cosines, yielding a checkerboard pattern, as observed in the experimental data, Fig. 2(b). Ref. [75] predicts that when the bias is only applied to one contact, with the other contact held at ground (again, relative to the gates), the two phase contributions from bias and field instead appear as arguments of a single cosine, yielding a diagonal stripe pattern. Experimentally, the bias is always applied only at one end of the Hall bar, with the other end grounded; however, interaction effects within the dot are likely to effectively symmetrize the applied bias [137]. Alternatively, a model in which the bias mainly affects the electrostatic (rather than chemical) potential [138] also yields Eq. (1) without the need for a symmetric bias. In either interpretation, the bias period corresponds to the edge velocity via $\Delta V_{\rm D} = (h/e)(v/a)$.

We account for the reduced amplitude of oscillations at high bias by multiplying the right side of Eq. (1) by a damping factor, $e^{-2\pi\alpha\,|V_{\rm D}|/\Delta V_{\rm D}}$, where $(2\pi\alpha)^{-1}$ gives the number of periods over which the amplitude falls to $1/e$ of its zero-bias value. Lacking theory for edge-state dephasing in FPI's, this form is motivated by the observation in related experiments of a dephasing rate proportional to energy [130, 108]. We thus identify a voltage-dependent dephasing rate, $\tau_\varphi^{-1}(V_{\rm D}) = \alpha|eV_{\rm D}|/2\hbar$, which reduces amplitude by $e^{-2t_{\rm o}/\tau_\varphi}$, where $2t_{\rm o} = 2a/v$ is the time of flight around the interferometer. To extract interference and dephasing parameters, the form

$$\delta G(V_{\rm D}) = \delta G_0 e^{-2\pi\alpha\,|\delta x|}\cos(2\pi\,\delta x), \tag{3.2}$$

where $\delta x = (V_{\rm D} - V_{\rm off})/\Delta V_{\rm D}$ and $V_{\rm off}$ is a bias offset, is fit to cuts of the data in Fig. 2(b),

which yields a period $\Delta V_{\mathrm{D}} = 56\ \mu$V and dephasing parameter $\alpha = 0.2$. These values, along with $\Delta B = 0.25$ mT are then used to produce the plot shown in Fig. 2(c). Figures 3(a) and 3(b) show vertical cuts from data along with fits of Eq. (2) at $B = 0.22$ T and 1.26 T, respectively, representing a trend toward smaller ΔV_{D} and larger α at higher fields, the details of which we now study.

3.4 Edge state velocities and dephasing

The black circles in Fig. 3(c) indicate the best-fit ΔV_{D} (right axis) and corresponding edge velocity (left axis) as a function of $1/B$. The velocities appear roughly proportional to $1/B$ before saturating at $v \sim 1.5 \times 10^5$ m/s for $1/B \gtrsim 2\ T^{-1}$. Red curves indicate calculations based on single-particle models of edge velocities in two regimes. In the high-field limit, where the cyclotron radius is much smaller than the length scale on which the confining potential changes by the cyclotron gap, $\vec{E} \times \vec{B}$ drift gives a velocity $v_{\mathrm{d}} = E/B$, where E is the local slope of the confining potential. The data in this regime are consistent with a value $E \sim 8 \times 10^4$ V/m, which is reasonable given device parameters. At low fields, where the cyclotron radius exceeds the length scale set by E, electron velocities can be estimated from a skipping-orbit model. For hard-wall confinement, the skipping velocity would be proportional to the cyclotron frequency and radius: $v_s \sim \omega_c r_c$. Here, we have performed a detailed semi-classical calculation assuming a more realistic confining potential that vanishes in the bulk and grows linearly near the edge. In this regime, the predicted velocity depends on not only B and E but also on the Landau level index, N, resulting in a discrete jump in velocity for every change in N. Since the density in the constrictions (which along with B determines N) varies over the course of the experiment, two theoretical curves are plotted in this regime: the top one corresponds to the lowest observed constriction density

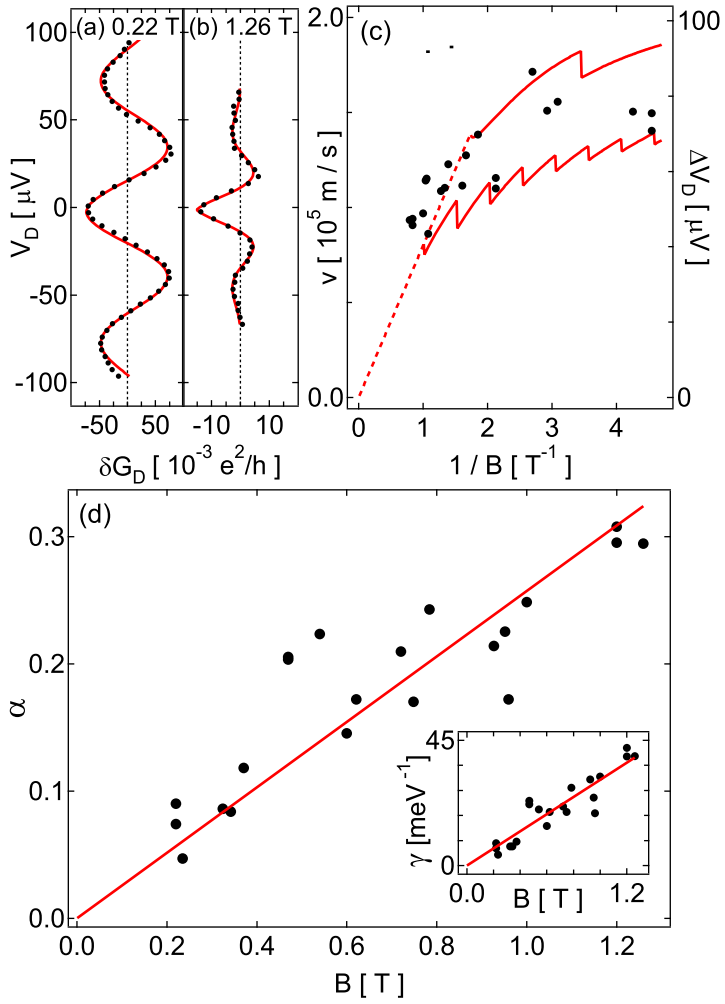

Figure 3.3: (a) G_{D} as a function of V_{D} (black dots) at a field of $B = 0.22$ T, with a fit of Eq. (2) (red curve) yielding $\Delta V_{\mathrm{D}} = 76$ μV and $\alpha = 0.063$. (b) Same as (a) but at $B = 1.26$ T and yielding $\Delta V_{\mathrm{D}} = 47$ μV and $\alpha = 0.34$. (c) Black dots indicate edge velocities (left axis) determined from measured ΔV_{D} (right axis) as a function of $1/B$. The red curves indicate theoretical calculations: at low $1/B$, the diagonal dashed line indicates the drift velocity corresponding to $E = 8 \times 10^4$ V/m; at high $1/B$, the top and bottom solid curves indicate the predicted skipping-orbit velocities corresponding to the lowest and highest constriction densities, respectively. (d) Best-fit damping parameter α as a function of B, with a linear fit of slope 0.26 T^{-1} constrained through the origin. Inset: $\gamma = 2\pi\alpha/e\Delta V_{\mathrm{D}}$ as a function of B, with a linear fit of slope 31 $(\mathrm{meV} \cdot \mathrm{T})^{-1}$ constrained through the origin.

of 2.8×10^{14} $\mathrm{m}^{-2}2$, and the bottom one corresponds to the highest, 9.5×10^{14} $\mathrm{m}^{-2}2$, both estimated from G_{D} and B.

Figure 3(d) shows the best-fit damping parameter α as a function of B, revealing rough proportionality: a straight line constrained to cross the origin describes the data well with a best-fit slope of 0.26 T^{-1}. In analogy to dephasing in 2D diffusive systems [139], we suggest that coupling to compressible regions in the bulk may lead to dephasing with the V_D-dependence $\tau_\varphi^{-1} \propto R_\square V_D$, where $R_\square$ is the resistance per square in the bulk. Over the field range of our data, the bulk longitudinal resistivity R_{xx} (not shown) is on average roughly proportional to B; taking R_{xx} as an estimate of $R_\square$ would then lead to a predicted dephasing rate proportional to both energy and magnetic field, consistent with the data. Despite this agreement, we emphasize that Ref. [139] was not developed for edge states or FPI's, and a theory of dephasing in this regime remains lacking.

Alternatively, defining the damping factor as simply $e^{-\gamma|eV_D|}$, one also finds rough proportionality between γ and B, as shown in the inset of Fig. 3(d). Here the best-fit slope for a straight line constrained through the origin is 31 $(\mathrm{meV}\cdot\mathrm{T})^{-1}$. The damping parameter γ is related to α and to the dephasing length, $\ell_\varphi = v\tau_\varphi$, by $\gamma = \alpha t_\mathrm{o}/\hbar = 2a/|eV_D|\ell_\varphi$; therefore, since t_o varies with field, at most one of α and γ can be proportional to B. Physically, the latter case would correspond to ℓ_φ^{-1} being the quantity that is linear in B instead of τ_φ^{-1}. Experimental scatter prevents us from distinguishing these two possibilities.

3.5 Nonlinear magnetoconductance in a 2 $\mu\mathrm{m}^2$ device

Measurements on a 2 $\mu\mathrm{m}^2$ device of similar design do not yield regular oscillations as a function of bias. Figure 4 shows G_D as a function of B and V_D in a regime of weak forward-tunneling, where diamond-like features appear. The field period $\Delta B \approx 1$ mT is roughly half that expected for pure AB interference in a device of this size, consistent with the Coulomb-dominated behavior previously observed at zero bias in this device [125].

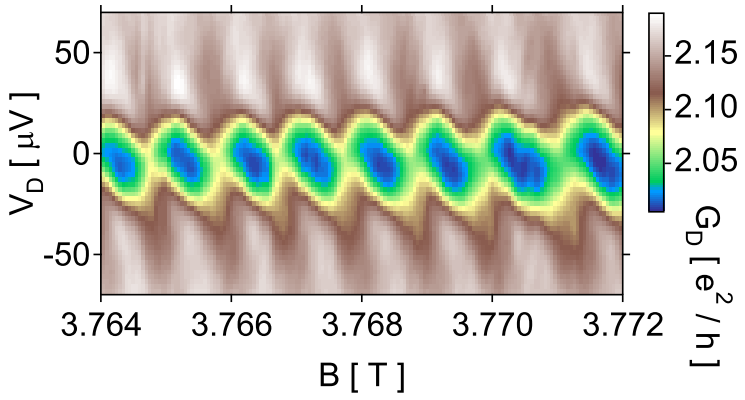

Figure 3.4: G_{D} as a function of B and V_{D} in the 2 μm^2 device.

Interpreting the finite-bias features as standard Coulomb blockade diamonds yields a charging energy of roughly 25 μeV, reasonable given the device size, 2DEG depth, and the large capacitance afforded by the top gate. In regimes of stronger forward tunneling, the diamonds become more smeared out, but unlike in the 18 μm^2 device, periodic oscillations as a function of dc bias are not seen.

3.6 Conclusion

In conclusion, quantum Hall FPI's large enough that Coulomb charging is negligible are found to display both AB and Fabry-Perot conductance oscillations. The combination of these two effects yields a checkerboard-like pattern of oscillations from which the edge-state velocity and dephasing rate can be extracted, and both are found to be consistent with theoretical calculations. Although this pattern resembles that seen in Mach-Zehnder interferometers, the dependence of its characteristics on magnetic field is evidently quite different from what has been observed in those devices [97, 109], providing experimental evidence that the underlying mechanisms for oscillations with bias in the two types of devices may be quite different.

3.7 Acknowledgments

We are grateful to R. Heeres for technical assistance and to B. I. Halperin, M. A. Kastner, C. de C. Chamon, A. Stern, I. Neder, R. Gerhardts, J. B. Miller and I. P. Radu for enlightening discussions. This research has been funded in part by Microsoft Corporation Project Q, IBM, NSF (DMR-0501796), Harvard University, and the Heisenberg program of DFG. Device fabrication at Harvard Center for Nanoscale Systems.

3.8 Epilogue

Since this work was published, we observed similar checkerboard patterns in more devices, fabricated on a variety of wafers. In all devices, including one on a wafer with only 1/3 the density of the one on which this study was done, the extracted velocities increase with decreasing field until reaching an upper bound somewhat less than the Fermi velocity. Although we anticipated that the confining potential differences resulting from different styles of gating (e.g. trenches) might affect the edge velocity in a measurable way, any such effect turned out to be negligible. While surprising, this result is nonetheless consistent with the fact that the depletion length inferred by comparing the effective area to the lithographic area does not depend on the style of gating either. On the other hand, the style of gating is seen to have a significant effect on the shape of the potential in the constrictions: for example, 750 nm constrictions formed by etching can have an electron density matching that in the bulk and can support all but the weakest FQH states, while similar-sized constrictions depleted by surface gates have a significantly reduced electron density and few if any FQH states. Evidently further study in this area would be useful; see ideas in Section 6.4.2.

Chapter 4

Dynamic nuclear polarization in the fractional quantum Hall regime

A. Kou, D. T. McClure, C. M. Marcus
Department of Physics, Harvard University, Cambridge, Massachusetts 02138, USA
L. N. Pfeiffer, K. W. West
Department of Electrical Engineering, Princeton University, Princeton, New Jersey 08544, USA

We investigate dynamic nuclear polarization in quantum point contacts (QPCs) in the integer and fractional quantum Hall regimes. Following the application of a dc bias, fractional plateaus in the QPC shift symmetrically about half filling of the lowest Landau level, $\nu = 1/2$, suggesting an interpretation in terms of composite fermions. Polarizing and detecting at different filling factors indicates that Zeeman energy is reduced by the induced nuclear polarization. Mapping effects from integer to fractional regimes extends the composite fermion picture to include hyperfine coupling.[1]

[1]This chapter is adapted with permission from Phys. Rev. Lett. **105**, 056804 (2010).

4.1 Introduction

An appealing physical picture of the fractional quantum Hall (FQH) effect is the composite fermion model [12, 26, 27], in which an even number, $2m$, of flux quanta ($\phi_0 = h/e$) bind to each electron, creating a composite fermion (CF) that feels an effective field, $B^* = B - 2mn\phi_0$, where B is the applied field perpendicular to the plane of the electron gas and n is the electron density. The effective field quantizes the CF energy spectrum into the analogue of electronic Landau levels; the FQH effect becomes the integer quantum Hall (IQH) effect of CFs. At filling factor $\nu = 1/2$, corresponding to $B^* = 0$ for CFs with two attached flux quanta ($m = 1$), the CFs form a Fermi sea that can have ground states with different degrees of spin polarization [140, 141]. Composite fermions at other filling factors also have non-trivial spin-polarized ground states. For example, $\nu = 2/3$ ($\nu_{CF} = -2$) and $\nu = 2/5$ ($\nu_{CF} = 2$) have been observed to have both spin-polarized and spin-unpolarized ground states [59, 142].

Dynamic nuclear polarization (DNP) has been used to investigate both the IQH and the FQH regime using transport measurements [65, 143, 58, 144, 145, 146, 147, 141, 148, 149, 150, 63, 151, 152, 153, 64, 154]. In both regimes, electron spin flips are accompanied by opposite nuclear spin flops. In gate-confined GaAs microstructures in the IQH regime, Wald *et al.* [65] showed that scattering from the lowest (spin-up) Landau level to the second (spin-down) Landau level flops a nuclear spin from down to up, which in turn increments the Overhauser field, B_{N}, opposite to the applied field, B. The resulting reduction in total effective Zeeman field was then detected in transport [65]. DNP in a quantum point contact (QPC) with only Zeeman splitting has also been observed [155]. In bulk two-dimensional (2D) geometries, breakdown of the IQH and FQH effects at high bias can also induce DNP [147, 148, 63, 152, 64, 154]. In this case, the direction of the resulting Overhauser field

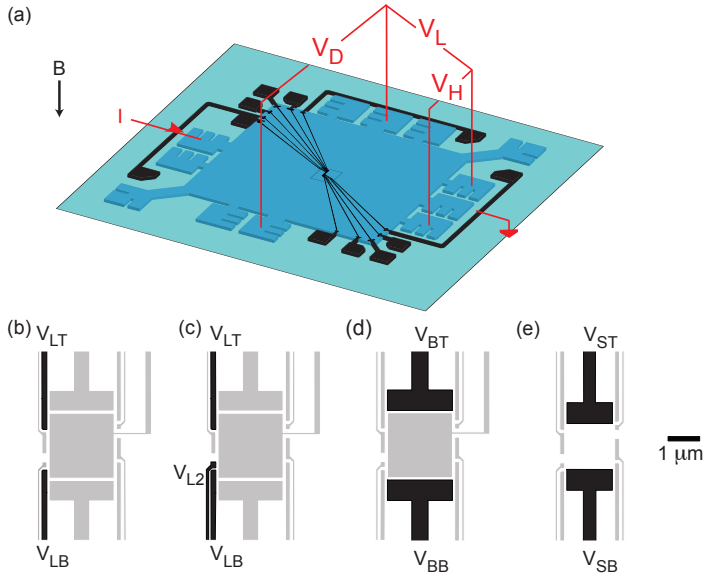

Figure 4.1: (a) Schematic of device layout on square mesa, with current bias, indicating positions of ohmic contacts where diagonal voltage, V_{D}, across the device, as well as bulk Hall voltage, V_H and longitudinal voltage, V_L, are measured. Gate layouts of (b) 1 μm, (c) 750 nm, (d) 2 μm, and (e) 1.4 μm constrictions are shown, with 1 μm scale bar. Depleted gates shown in black, grounded gates shown in gray.

depends on experimental details. In the FQH regime, much of the work—in bulk and in microstructures—has focused on $\nu = 2/3$ [144, 145, 146, 150], where DNP is attributed to spin-flip tunneling between spin-unpolarized and spin-polarized domains. Bulk 2D studies using DNP and nuclear relaxation at $\nu = 1/2$ were used to investigate the degree of spin polarization of the metallic CF state as a function of applied field [141, 151, 153]. Despite the extensive literature on this topic, on both bulk and confined devices, no explicit connection between DNP in the IQH and FQH regimes—creation or detection—has been drawn to our knowledge.

In this Letter, we investigate DNP in a gate-defined QPC and identify surprising correspondences between the IQH and FQH regimes, which we interpret within a composite fermion picture. In contrast to the situation in bulk FQH systems, where DNP may change the spin configuration at a given filling factor, we find that DNP in the vicinity of a QPC

can evidently induce changes in density (hence local filling factor) within the constriction. Resistance plateaus as a function of B in both IQH and FQH regimes shift and change in length following application of a nonzero dc bias. Using resistively detected nuclear magnetic resonance (NMR), we demonstrate that the applied bias induces nuclear polarization. Interestingly, the pattern of shifting plateaus is symmetric about the the half-filled first Landau level, $\nu = 1/2$. Comparable shifts are also found in the IQH regime. We determine the sign of the induced Overhauser field to be opposed to the applied field in all cases, and estimate the magnitude of the Overhauser field by observing its effects at large filling factors, where the Overhauser field can exceed the applied field and effectively reverse the sign of the Zeeman field. Finally, we interpret related DNP effects in the IQH and FQH regimes in terms of simple Zeeman-split CF edge states.

4.2 Devices and measurement

Measurements were carried out on four devices [Figs. 1(b-e)], showing similar behavior. Data presented are from devices in Figs. 1(b,c). The devices were fabricated on a two-dimensional electron gas (2DEG) in a symmetrically Si-doped GaAs/AlGaAs 48 nm quantum well structure located 400 nm below the wafer surface with density $n = 7.8 \times 10^{14}$ m^{-2} and mobility $\mu = 1{,}300$ m^2/V·s measured in the dark. Similar behavior was observed on a different wafer with roughly twice the density. Square mesas were wet-etched [Fig. 1(a)], and Ti/Au (5 nm/15 nm) surface gates were patterned using electron-beam lithography. Depleted gates except V_{L2} were set to ~ -1.5 V. Gate V_{L2}, when used, was set to ~ -0.8 V. Other gates were grounded.

Measurements were made using a current bias, I, with dc component, I_{dc}, up to 100 nA and an ac component of 0.4 nA at 153 Hz. The electron temperature was $\sim$50 mK.

We typically measure the diagonal voltage, $V_{\rm D}$, which is the voltage difference between incoming edge states on opposite sides of the QPC. Lock-in measurements of the diagonal resistance, $R_{\rm D} \equiv dV_{\rm D}/dI$, were used to determine the local filling factor within the QPC, $\nu_{\rm D} \equiv h/R_{\rm D}e^2$. Two procedures were used to apply $I_{\rm dc}$ to the QPC. In the first procedure ("holding"), $I_{\rm dc}$ was set to a value $I_{\rm hold}$ for a time $t_{\rm hold}$ before being set back to 0. Unlike in less symmetric geometries [147], results did not depend on the sign of $I_{\rm hold}$. In the second procedure ("sweeping"), $I_{\rm dc}$ was swept from a positive value ($I_{\rm max}$) to a negative value ($-I_{\rm max}$) and then swept back to 0; sweep direction made no difference. The two procedures lead to similar overall behavior, as well.

Figure 2(a) shows $R_{\rm D}$ as a function of B and $I_{\rm dc}$ in the 750 nm constriction [Fig. 1(c)], acquired using the sweeping procedure at each field then stepping the field downward. Comparing zero-bias data taken prior to sweeping (red) with the zero-bias cut through data (black) shows that sweeping causes the $\nu_{\rm D} = 1/3$ plateau to extend to lower field, just past the high-field edge of the $\nu_{\rm D} = 2/5$ plateau in (red) data taken prior to sweeping $I_{\rm dc}$ (red). The transition region between $\nu_{\rm D} = 1/3$ and $\nu_{\rm D} = 2/5$ becomes abrupt after sweeping dc bias; in the prior data, the transition is seen to be gradual. Figure 2(b) shows similar extensions of plateaus for $\nu_{\rm D}$ between 2/5 and 2/3 in the 1 μm constriction [Fig. 1(b)]. Here, the bias was applied using the holding procedure applied at each field, then the field stepped downward. The black trace shows $R_{\rm D}$ after the return to zero dc bias at each field while the red trace was measured with no dc bias applied.

The pattern of shifts and extensions of plateaus of $R_{\rm D}$ [Fig. 2(b)] exhibits a striking symmetry about $\nu_{\rm D} = 1/2$: applying then removing dc bias at each field causes all plateaus to shift toward $\nu_{\rm D} = 1/2$, which, as a symmetry point, does not change position[2]. Bulk

[2]On the high-field side of the symmetry point ($\nu_{\rm D} < 1/2$) shifts and extensions of plateaus require that the bias is applied between plateaus, while on the low-field side ($1/2 < \nu_{\rm D} < 2/3$) shifting occurs regardless of where $I_{\rm dc}$ is applied.

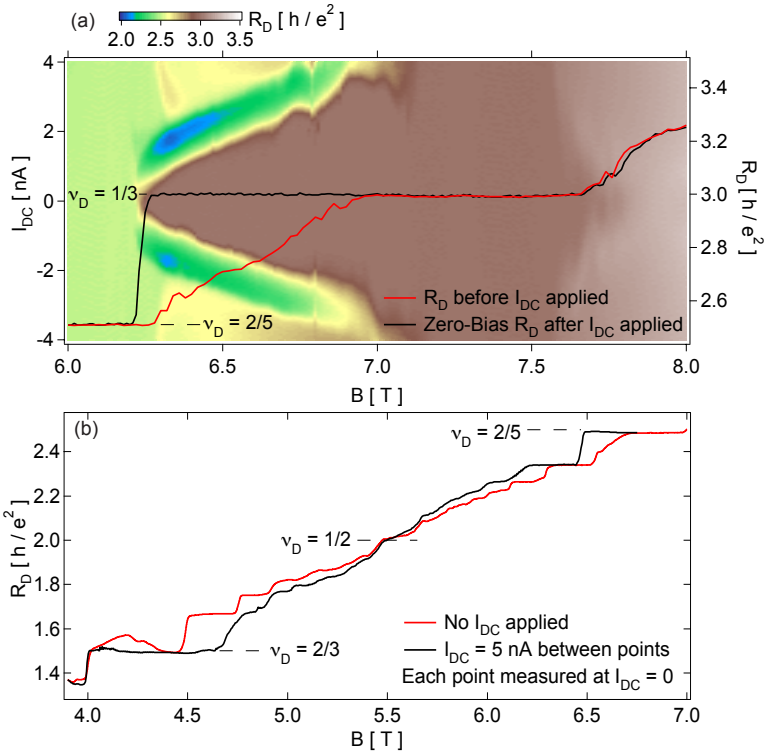

Figure 4.2: (a) R_{D} as a function of B and I_{dc} in the 750 nm constriction. Red trace indicates R_{D} as a function of B before I_{dc} has been applied to the constriction. Black trace indicates R_{D} as a function of B at $I_{\mathrm{dc}} = 0$ after applying a nonzero I_{dc} to the constriction. (b) R_{D} as a function of B in the 1 μm constriction. Red trace indicates R_{D} before I_{dc} has been applied to the constriction. Black trace indicates R_{D} measured at $I_{\mathrm{dc}} = 0$ after $I_{\mathrm{dc}} = 5$ nA has been applied to the constriction.

Hall and longitudinal resistances do not exhibit any change in behavior after applying I_{dc}.

Similar shifts and extensions of plateaus occur when the bias is applied at a different filling factor from where its effects are observed. Changes in filling factor can be accomplished by either changing field or QPC gate voltage. This is illustrated in Figs. 3(a-c), which show R_{D} as a function of time, measured at the same field and gate settings, following application of I_{dc} at three different filling factors. Field and gate voltages were first set to give a well-quantized $\nu_{\mathrm{D}} = 3/5$ plateau in the 1 μm constriction prior to application of I_{dc}. Then, either field or gate voltage was used to change ν_{D}, where dc bias

sweeping procedure was applied. Field or gate voltage values were then returned to the settings where $\nu_D = 3/5$ was originally observed. In all cases—regardless of where I_{dc} is applied—after a transient (due to residual heating from I_{dc}) R_D settles at a value indicating $\nu_D = 2/3$ for tens of minutes before suddenly returning to its original $\nu_D = 3/5$ value.

Plateau shifting with characteristic symmetry about $\nu = 1/2$ is also observed when I_{dc} is applied at a single filling factor rather than at each value of B. In Fig. 3(d), the I_{dc} sweeping procedure applied once, just below $\nu = 1/3$ ($B = 7.50$ T), before sweeping field downward to $\nu = 2/3$ ($B = 4.00$ T) with I_{dc} at zero. Symmetry about $\nu = 1/2$ is evident despite the asymmetry of where the dc bias was applied. Similar behavior is seen when I_{dc} is applied once at $\nu = 3/5$ ($B = 4.50$ T) before sweeping the magnetic field upward toward $\nu = 1/3$ ($B = 7.80$ T) with $I_{dc} = 0$ [Fig. 3(d)]. From these data, we conclude that the observed symmetry about $\nu = 1/2$ reflects the *response* of the system to a common, roughly field-independent, physical mechanism.

4.3 Role of nuclear spins

The slow relaxation seen in Figs. 3(a-c) suggests DNP as the origin of the effects of applied bias. This is confirmed using resistively detected NMR. Following sweeping application of I_{dc}, an ac magnetic field pulse at frequency f_{NMR} is applied using a six-turn coil that orients the ac field predominantly in the plane of the electron gas. When f_{NMR} matches one of the expected NMR frequencies, R_D returns to the value measured before applying I_{dc}. Figures 4(a,b) show depolarization signatures in R_D for ^{75}As NMR at $\nu_D = 1/3$ and $\nu_D = 3/5$. Similar signatures are also observed for ^{69}Ga and ^{71}Ga NMR frequencies (not shown).

Following DNP at $\nu_D = 3/5$, ramping the field to the edge of the $\nu_D = 1$ plateau

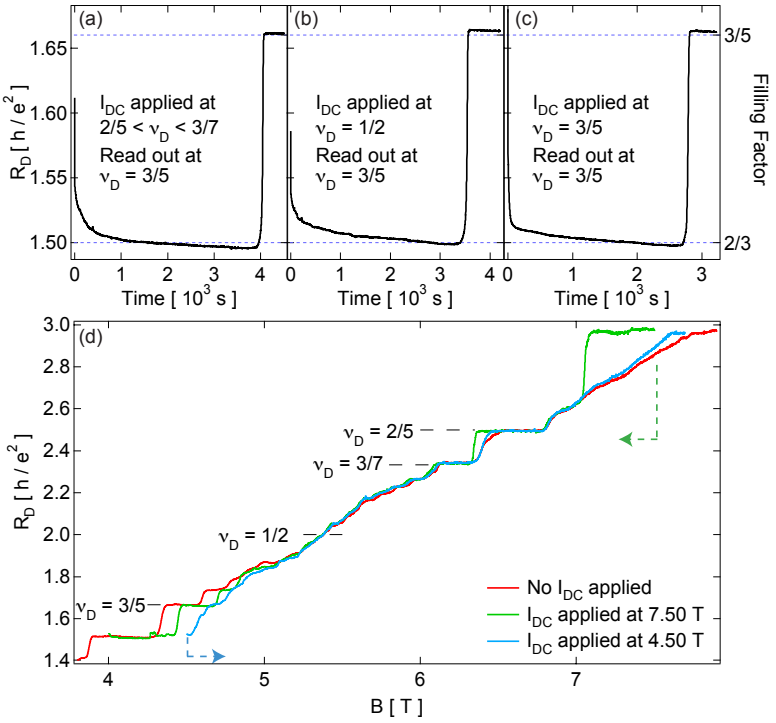

Figure 4.3: (a-c) R_D as a function of time measured in the 1 μm constriction at $\nu_D = 3/5$ after $I_{dc} = 10$ nA was applied at $2/5 < \nu_D < 3/7$, $\nu = 1/2$, and $\nu_D = 3/5$. (d) R_D as a function of B in the 1 μm constriction. Red trace indicates R_D before I_{dc} has been applied. Green trace indicates R_D after $I_{dc} = 20$ nA has been applied at $B = 7.50$ T. Blue trace indicates R_D after $I_{dc} = 34$ nA has been applied at $B = 4.50$ T.

causes all plateaus to return to their unpolarized positions. This rapid depolarization can be understood by the presence of skyrmions near $\nu = 1$, which are known to cause relaxation of nuclear polarization [156, 67, 68].

4.4 Magnitude of the Overhauser field

At lower fields, plateau shifts and extensions in the IQH regime are seen following DNP from I_{dc} applied between (not directly on) IQH plateaus. Following DNP, spin-split plateaus at $\nu_D = 3$ and $\nu_D = 5$ disappear for several minutes [Fig. 4(d)]. NMR confirms the DNP interpretation [Fig. 4(c)]. The sign and magnitude of the Overhauser field can also be

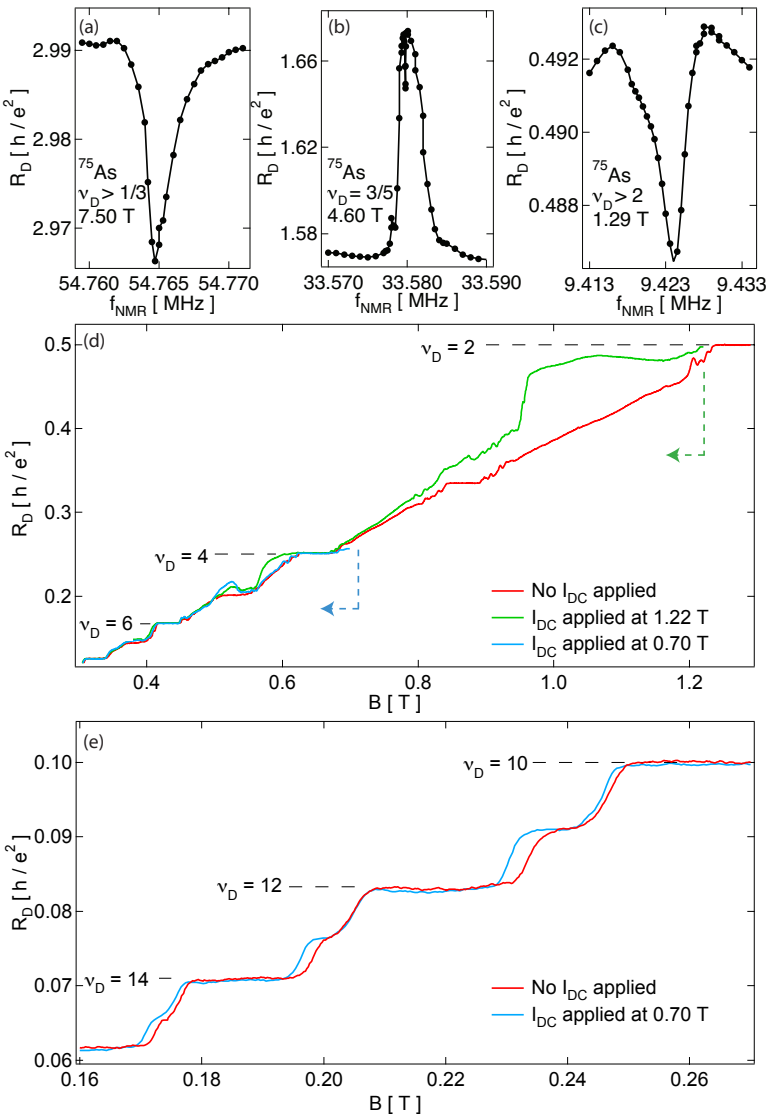

Figure 4.4: (a-c) R_D as a function of f_{NMR} in the 1 μm constriction at B = 7.50 T, 4.60 T, and 1.29 T[3]. (d,e) R_D as a function of B in the 1 μm constriction. Red trace indicates R_D before I_{dc} has been applied. Green trace indicates R_D after I_{dc} = 54 nA has been applied at B = 1.22 T. Blue trace indicates R_D after I_{dc} = 95 nA has been applied at B = 0.70 T.

deduced in the IQH regime. For B_N along B, ($B_N > 0$), spin splitting will always increase with DNP; for B_N opposing B, spin splitting will decrease for mild DNP, reach zero for $|B_N| = B$ and again increase when $|B_N| > B$ (with reversed spin splitting). Comparing

Figs. 4(d,e), we see that for $B \sim 0.5 - 1$ T, the odd (spin-split) plateaus are weakened by DNP, whereas for $B \sim 0.2$ T, odd plateaus are enhanced by DNP. We conclude that B_{N} induced by DNP is directed opposite to B and is between 0.2 and 0.5 T in magnitude.

To connect DNP effects between IQH and FQH regimes, we polarize in the one regime and read out in the other. For instance, we apply I_{dc} using the sweeping procedure at $\nu_{\mathrm{D}} = 2$, followed by ramping to a value of field where $\nu_{\mathrm{D}} = 3/5$ before polarization. Depolarization from skyrmions upon passing through $\nu_{\mathrm{D}} = 1$ are avoided by fully depleting the QPC during the field ramp. We find that R_{D} initially indicates $\nu_{\mathrm{D}} = 2/3$ value before sharply returning to the $\nu_{\mathrm{D}} = 3/5$ value after several minutes. Reversing the order—polarizing at $\nu_{\mathrm{D}} = 3/5$ and reading out at $2 < \nu_{\mathrm{D}} < 3$—yields analogous results. We conclude from both procedures that the direction of induced Overhauser field opposes the applied field in both IQH and FQH regimes. We also conclude that the relevant DNP occurs in the QPC (not downstream) since depolarization by skyrmions was eliminated by depleting only the electrons in the QPC constriction.

4.5 Discussion

In the IQH regime, DNP presumably occurs by spin-up electrons at high-bias entering the QPC flipping into empty spin-down states, accompanied by a nuclear flop from spin down to spin up. Because dc bias exceeds Zeeman splitting but not cyclotron energy, the opposite mechanism, involving flip-flop spin relaxation between different Landau levels, which would would tend to align B_{N} and B, does not occur.

Evidently, a similar mechanism appears to occur in the FQH regime. Within a CF

[3]The expected NMR frequencies for $B = 1.29$ T, 4.50 T, and 7.50 T are 9.406 MHz, 33.540 MHz, and 54.685 MHz, respectively. We attribute this difference to a slight offset in zero value of our magnet, equal to roughly 8 mT at zero field.

picture, even filling factors can have spin-unpolarized ground states while odd filling factors are always at least partially polarized [12]. Hence, similar to electrons, CFs can be excited from a spin-up to a spin-down state. Within this model, for example, exciting CFs from a spin-up subband of $\nu = 3/5$ ($\nu_{\mathrm{CF}} = -3$) to a spin-down subband of $\nu = 4/7$ ($\nu_{\mathrm{CF}} = -4$) will result in $B_{\mathrm{N}} < 0$. Excitations from spin-down to spin-up states may also be possible, however, since the CF Zeeman energy is comparable to the CF cyclotron energy [12].

We interpret the effect of B_{N} on plateau structure as depending on ground-state spin configurations at successive filling factors. If successive states have different degrees of spin-polarization, B_{N} will change the length of the associated plateaus. If successive states are both spin-polarized, then B_{N} will shift plateau positions. In the IQH regime, odd filling factors are spin-polarized while even filling factors are spin-unpolarized, hence B_{N} causes plateaus at even filling factors to lengthen at the expense of plateaus at odd filling factors. In the FQH regime, the more spin-polarized state will also be destabilized by B_{N}, leading to a shorter plateau. We observe the destabilization of more spin-polarized plateaus in favor of less spin-polarized plateaus in both regimes: at $3/5 \leq \nu_{\mathrm{D}} \leq 2/3$ ($-3 \leq \nu_{\mathrm{CF}} \leq -2$) in Fig. 2(b) in the FQH regime and at $2 \leq \nu_{\mathrm{D}} \leq 3$ in Fig. 4(d) in the IQH regime. The changes in the lengths of the plateaus observed in Fig. 2(b) are analogous to those observed in Fig. 4(d), suggesting that CF's in the FQH regime are exhibiting the same behavior as electrons in the IQH regime. Within this picture, shifts in plateau position can only occur in the FQH regime, where successive states can both be spin-polarized. A change in Zeeman energy will not affect the size of the gap between spin-polarized CF Landau levels but will shift the energies of the levels equally. When the Zeeman energy is decreased, the energy of each spin-polarized level increases, causing a local depopulation of electrons in the QPC. Each energy level will then be filled at a lower magnetic field; the start of each plateau will then appear at a lower field than before DNP. We observe this shifting of the plateaus

at $1/3 < \nu < 2/5$ [Fig. 2(a)]. Finally, while DNP is found to readily occur at $\nu_D = 1/2$, it leaves little or no signature in R_D at $\nu_D = 1/2$, by symmetry, but can be observed by moving to another filling factor after DNP, as seen in Fig. 3(b).

4.6 Acknowledgments

We thank J. P. Eisenstein, B. I. Halperin, I. Neder, M. S. Rudner, and K. von Klitzing for enlightening discussions. Research funded by Microsoft Corporation Project Q, IBM, NSF (DMR-0501796), and Harvard University. Device fabrication at Harvard's Center for Nanoscale Systems.

4.7 Epilogue

Although these phenomena did not initially appear to be directly related to the interference effects that motivated our experiments, recent observations by Angela Kou suggest that interference in an anti-dot in the FQH regime can be affected by DNP. In particular, local polarization of the nuclei by the methods described in this chapter can suppress oscillations at certain fractional filling factors. The exact reasons for the suppression remain unclear, but the fact that it happens at some filling factors and not others may provide greater insight into edge structures and processes limiting interference. The related possibility that DNP might actually enhance oscillations at some filling factors could open doors to additional experiments.

Chapter 5

Fabry-perot interferometry with fractional charges

D. T. McClure, W. C. Chang, C. M. Marcus
Department of Physics, Harvard University, Cambridge, Massachusetts 02138, USA
L. N. Pfeiffer, K. W. West
Department of Electrical Engineering, Princeton University, Princeton, New Jersey 08544, USA

Resistance oscillations in electronic Fabry-Perot interferometers near fractional quantum Hall (FQH) filling factors $1/3, 2/3, 4/3$ and $5/3$ in the constrictions are compared to those near integer quantum Hall (IQH) filling factors in the same devices and at the same gate voltages. Two-dimensional plots of resistance versus gate voltage and magnetic field indicate that all oscillations are Coulomb dominated. A charging-model analysis of gate-voltage periods yields an effective tunneling charge $e^* \approx e/3$ for all FQH states and $e^* \approx e$ for IQH states. Temperature decay of the oscillations appears exponential, qualitatively consistent with a recent prediction, and the surprising filling-factor dependence of the associated energy scale may shed light on edge structure.[1]

[1]This chapter has been accepted for publication in Physical Review Letters. A pre-print is available at `http://arxiv.org/abs/1112.0538`.

5.1 Introduction

Like their optical analogs, electronic Fabry-Perot interferometers allow quantum interference to be probed via tunable parameters that induce periodic transmission oscillations. Moreover, working with charged excitations in quantum Hall edge states, these devices feature an interplay of coherence, interaction, and magnetic effects; notably, such devices could demonstrate anyonic [75] and non-Abelian [79, 118, 119, 81] statistics and potentially comprise topologically protected qubits [80]. In the integer quantum Hall (IQH) regime, recent experimental [103, 121, 125, 105] and theoretical [87, 82] work has extended the results of initial experiments [89, 90, 126, 91, 92] and clarified the role of Coulomb interactions. Behavior consistent with Aharonov-Bohm (AB) interference of non-interacting electrons was recently observed [125, 105], and can be qualitatively distinguished from the Coulomb-dominated (CD) type using a 2D plot of resistance versus magnetic field and gate voltage.

In the fractional quantum Hall (FQH) regime, signatures of fractional charge [87] and both Abelian [75, 82] and non-Abelian [79, 81] statistics have been predicted in both the CD [79, 87, 81, 82] and AB [75, 79, 81, 82] regimes, but few experimental results have been published. Resistance oscillations generally occur when the interferometer resistance deviates slightly from a plateau, indicating weak tunneling through an IQH or FQH state in the constrictions; we will classify oscillations according to f_c, this state's rational filling factor. Camino et al. [49] first observed oscillations at $f_c = 1/3$ consistent with CD-regime tunneling of charge-$e/3$ quasi-particles, though other explanations may be possible [49, 125]; Ofek et al. [105] later reported a similar result that included a 2D plot justifying a CD-regime explanation. Weaker oscillations have been reported [106] near $f_c = 7/3$ and $5/2$, though apparent device instability hampers their interpretation. This experiment [106],

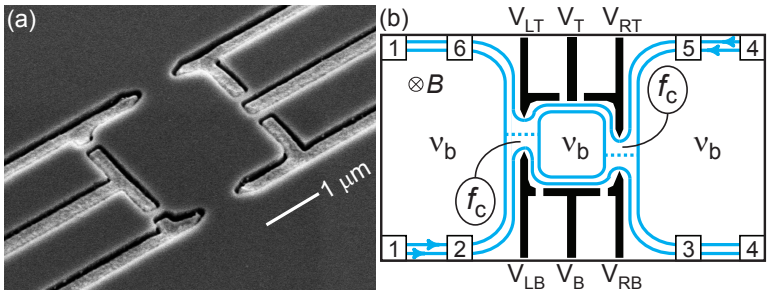

Figure 5.1: (a) Scanning electron micrograph of a typical interferometer. (b) Gate layout of the 4 μm^2 device with schematic diagram of edge state paths, filling factors, and ohmic contacts. A current bias applied between contacts 1 and 4 allows measurement of diagonal resistance $R_{\rm D}$ (contacts $2-5$) and Hall resistance $R_{\rm xy}$ (contacts $3-5$). This picture assumes that only one edge is partially transmitted by the interferometer, while others are fully transmitted or reflected. For clarity, only one fully-transmitted edge and no fully-reflected edges are shown.

shot-noise measurements near FQH states in the first [43, 44] and second [45] Landau levels, and related theoretical work [46, 47] suggest the possibility of tunneling mediated by quasi-particles with a larger charge than expected. Analysis of CD oscillations can reveal the charge of tunneling quasi-particles, but such measurements have not been reported for $f_{\rm c}$ other than 1/3, where experiments have consistently found the expected charge.

In this Letter, we report measurements of CD oscillations near the low-magnetic-field edges of quantized plateaus associated with several IQH and FQH states: $f_{\rm c} = r = 1, 2, 3, 4$ and $f_{\rm c} = r/3 = 1/3, 2/3, 4/3, 5/3$. The dependence of gate-voltage periods on $f_{\rm c}$ is well described by a charging model [87, 82], allowing extraction of effective charges consistent with $e^* \approx e/3$ for fractional $f_{\rm c}$ and $e^* \approx e$ for integer $f_{\rm c}$. Magnetic-field periods are roughly proportional to $1/r$ in both the integer and fractional regimes, also consistent with the model. The oscillation amplitudes decay exponentially with temperature, as anticipated theoretically [82], but with a surprising pattern: the associated temperature scale is different for the IQH and FQH regime, but otherwise independent of $f_{\rm c}$ and device area.

5.2 Device and measurement details

Interferometers were fabricated using e-beam lithography on GaAs/AlGaAs heterostructures with a two-dimensional electron gas (2DEG) of density $n_b = 1.7 \times 10^{11}$ cm^{-2}2 and mobility $\mu = 2 \times 10^7$ cm^2/Vs in a 40-nm quantum well centered 290 nm below the surface. A BCl_3 reactive ion etch formed 150 nm deep trenches[2] into which Ti/Au gates were deposited in the same lithographic step [Fig. 1(a)]. Measurements on two devices are reported, one with lithographic area $A_{lith} = 4\ \mu$m^2 and 750 nm constrictions [identical to the device in Fig. 1(a), and shown schematically in Fig. 1(b)] and the other with $A_{lith} = 2\ \mu$m^2, 600 nm constrictions, and a single gate V_B in place of gates V_{LB}, V_B, V_{RB}. Devices were cooled in a dilution refrigerator with base temperature $\lesssim 10$ mK[3]. The interferometer's diagonal resistance R_D [24] and the bulk Hall resistance R_{xy} were measured simultaneously using LI-75A pre-amplifiers from NF Corporation followed by a lock-in with ac current bias $I = 0.25$ nA [Fig. 1(b)] and time constant ~ 0.5 s.

Figure 2(a) shows R_{xy} and R_D of the 4 μm^2 device as a function of perpendicular magnetic field B, covering filling factors from 2/3 to 3 in both constrictions and bulk. Voltages of ~ -200 mV on gates V_{LT}, V_{RT}, V_{LB}, and V_{RB} reduced electron density in both constrictions by $\sim 10\%$ compared to the bulk, while preserving several FQH plateaus. Oscillations in R_D (Fig. 2 insets) were observed at the low-field edges of several IQH and FQH plateaus, where presumably the only forward transmission of the interfering edge occurs via weak forward tunneling through the f_c quantum Hall state [Fig. 1(b)]. Gate-voltage adjustments allowed variation of the magnetic field (and thereby the bulk filling

[2]The trenches improve device performance in two ways: their steep confining potential allows the formation of sub-micron constrictions with $f_c \approx \nu_b$, and the elimination of the donor layer between the gates and the 2DEG enhances stability.

[3]Evidence that the 2DEG also reaches this temperature is presented in Fig. 5 and the associated discussion.

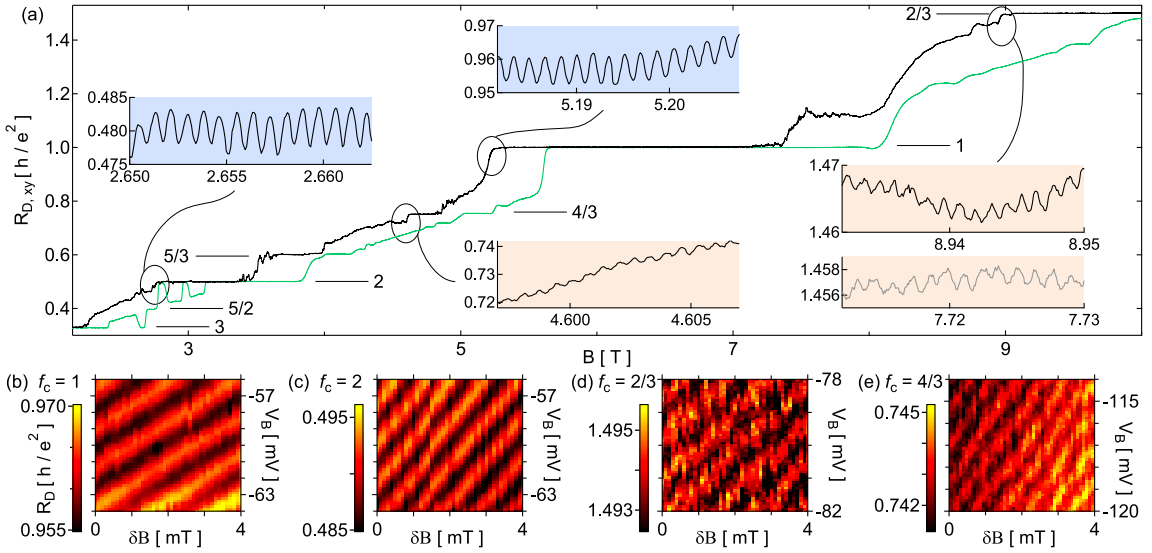

Figure 5.2: (a) Resistances R_{D} (black) and R_{xy} (green) as a function of perpendicular magnetic field B, with V_{T} and V_{B} near -100 mV and all other gate voltages near -200 mV. Numbered horizontal lines indicate filling factors of notable quantum Hall plateaus. Insets: detail views of R_{D}, revealing oscillations at $f_{\mathrm{c}} = 1$ (top), 2 (left), 2/3 (right), and 4/3 (bottom). For the lower panel in the $f_{\mathrm{c}} = 2/3$ inset, constriction gate voltages are near -500 mV. All features are independent of the field sweep rate (typically ~ 20 mT/min) and direction. Here and throughout, blue (orange) indicates integer (fractional) f_{c}. (b-e) Plots of R_{D} in the $B - V_{\mathrm{B}}$ plane, with gate voltages comparable to those in (a); $B = B_0 + \delta B$, with $B_0 = 5.200$ T, 2.670 T, 8.831 T, and 4.684 T, respectively.

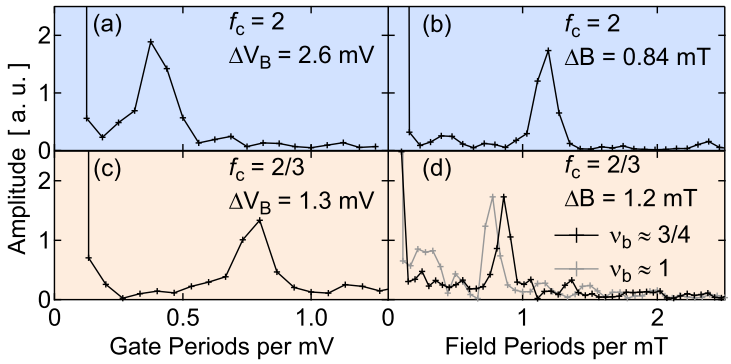

Figure 5.3: Sample FFT's of oscillations with respect to V_{B} and B, for $f_{\mathrm{c}} = 2$ and 2/3. Raw data for (b) and (d) are shown in the corresponding Fig. 2(a) insets, while raw data for (a) and (c) are vertical cuts from 2D plots as in Figs. 2(c,d) but with a larger gate-voltage range for greater frequency resolution.

factor $\nu_b = n_b h/eB$) where each plateau and its associated oscillations appeared; as in the lower panel of the $f_c = 2/3$ inset. Even as ν_b was thus tuned through a range of compressible and incompressible states, the magnetic-field and gate-voltage periods at each f_c remained nearly constant. The slight period difference between the two $f_c = 2/3$ inset panels [more apparent as a frequency difference in Fig. 3(d)] is consistent with reduced device area at more negative gate voltages. Two-dimensional sweeps of magnetic field and gate voltage [Figs. 2(b-e)] show positively sloped constant-phase lines, indicating CD oscillations [125].

Field and gate periods were extracted from fast Fourier transforms (FFT's) [Fig. 3], which all show a sharp peak at a single frequency. A gaussian fit to the peak gives the center frequency f_0 and full width at half-maximum δf, with periods ΔB or ΔV_g given by $1/f_0$. For FFT's over N_{osc} oscillations, we find $\delta f \sim 1/N_{osc}$, indicating that the uncertainty results from the finite data range.

5.3 Full data sets and analysis

Similar oscillations appeared in the 2 μm^2 device, and at $f_c = 1/3, 5/3, 3$ and 4. The remaining figures present three data sets, with the same gate voltages used at all integer and fractional f_c within each. Gate periods [Fig.. 4(a)] are normalized by their values at $f_c = 1$, allowing comparison of periods from all four gates common to both devices. A steady increase in ΔV_g with f_c appears in the FQH regime, with a similar but weaker trend in the IQH regime. Field periods [Fig. 4(b)] appear proportional to $1/r$, where $f_c = r$ in the IQH regime and $f_c = r/3$ in the FQH regime. Separate fit lines of the form $\Delta B \propto 1/r$ agree with data from each regime in each data set, with slightly larger slopes in the FQH regime than in the IQH regime.

We next summarize the theoretical charging model [87, 82] used to analyze the

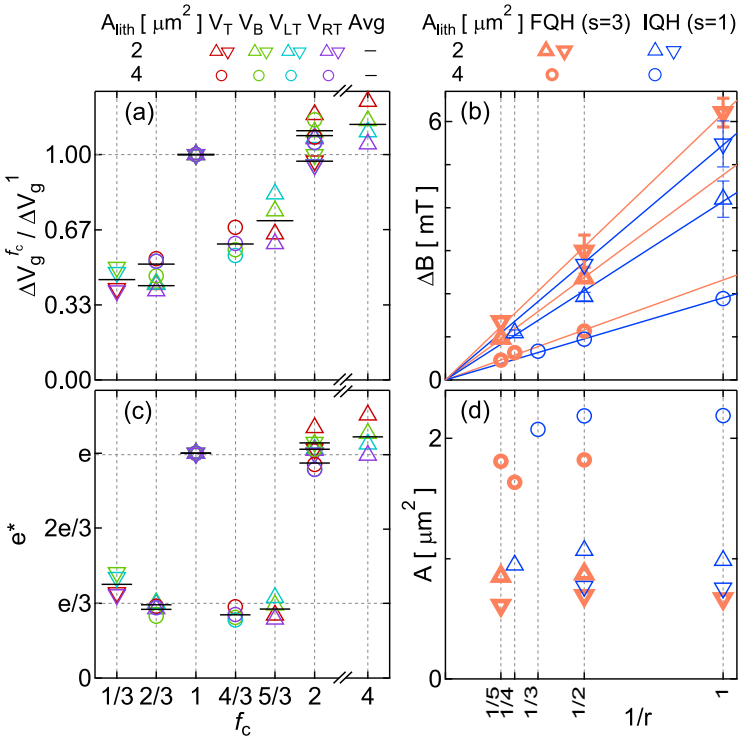

Figure 5.4: (a) Gate periods $\Delta V_{\rm T}$ (red), $\Delta V_{\rm B}$ (green), $\Delta V_{\rm LT}$ (aqua) and $\Delta V_{\rm RT}$ (purple), and their average (horizontal black lines), as a function of $f_{\rm c}$, normalized by their values at $f_{\rm c} = 1$. Throughout Figs. 4 and 5, two data sets are taken from the 2 μm^2 device (triangles) and one from the 4 μm^2 device (circles). (b) Field periods of IQH ($f_{\rm c} = r$) [thin, blue] and FQH ($f_{\rm c} = r/3$) [thick, orange] oscillations versus $1/r$. Error bars, corresponding to FFT peak widths, are omitted when smaller than markers. Fit lines have slopes $1.9, 2.3, 4.1, 4.8, 5.4$, and 6.2 mT from bottom to top. (c) Effective charges e^* extracted from the gate periods shown in (a) using Eq. 1, assuming $e^* = e$ at $f_{\rm c} = 1$. (d) Effective areas calculated using Eq. 2 from the values of ΔB shown in (b).

data[4]. In this model, oscillations can arise from charge balancing in a nearly isolated island of charge, coupled to the leads via weak forward tunneling, with charging events occurring in units of the quasi-particle charge e^* in the constrictions. This charge is expected to depend not on the identity of the partitioned edge, but instead on the state $f_{\rm c}$: for integer $f_{\rm c}$, $e^* = e$, and for $f_{\rm c} = r/s$, the composite fermion model [157] predicts $e^* = e/s$. The charge on the island is $N_{\rm L}e^*$, with $N_{\rm L}$ quantized to an integer value. The 2DEG in this

[4]In the regime of our oscillations, Ref. [82]'s terminology relates to ours as follows: $\nu_{\rm out} = f_{\rm c}$ and $\nu_{\rm in} \lesssim \nu_{\rm b}$.

area also contains continuous negative charge $N_\phi f_c e$ from the lower-energy electrons, where $N_\phi = BA/\phi_0$ is the (non-quantized) number of quanta of flux, $\phi_0 = h/e$, in the area A enclosed by the interfering edge. To minimize energy, the total negative charge must balance the background positive charge $N_{\rm BG}|e|$ from ionized donors (positive) and gate voltages (negative), yielding the charge neutrality equation $N_\phi f_c e + N_{\rm L} e^* \approx N_{\rm BG} e$, where quantization of $N_{\rm L}$ prevents exact equality. Expressing N_ϕ and $N_{\rm BG}$ in terms of gate voltage and magnetic field, and finding the change in these parameters needed to induce a unit change in $N_{\rm L}$, allows calculation of oscillation periods.

Gate voltages affect the charge balance in three ways: through the enclosed flux via area, with $\beta_{\rm g} \equiv dN_\phi/dV_{\rm g} = (B/\phi_0)(dA/dV_{\rm g})$, and through the background charge via both density $n_{\rm BG}$ and area. Summing the two background charge effects gives $\gamma_{\rm g} \equiv dN_{\rm BG}/dV_{\rm g} = n_{\rm BG}(dA/dV_{\rm g}) + A(dn_{\rm BG}/dV_{\rm g})$, which is assumed B-independent [82]. For fixed magnetic field, the charge neutrality equation then yields the gate-voltage period

$$\Delta V_{\rm g} = \frac{e^*/e}{\gamma_{\rm g} - \beta_{\rm g} f_c}. \tag{5.1}$$

This result reflects the Coulomb-blockade intuition that $\Delta V_{\rm g} \propto e^*$, but here the gating effect of the lower-energy electrons, represented by $\beta_{\rm g} f_c$, may cause the lever-arm to depend on f_c: although $\beta_{\rm g} \propto B$ and $f_c \sim 1/B$, the second relationship is inexact since plateau widths are non-zero and f_c is discrete. Considering oscillations at the low-field edges of plateaus, those near weaker plateaus will have larger $\beta_{\rm g} f_c$, hence larger $\Delta V_{\rm g}$, consistent with the data in Fig. 4(a). An f_c-independent lever-arm would be obtained for $dA/dV_{\rm g} = 0$, i.e. for an ideal back gate, but both the geometry of our device and the observed f_c-dependence of $\Delta V_{\rm g}$ suggest that the gates mainly affect the area.

Assuming ideal side gates (i.e. $dn_{\rm BG}/dV_{\rm g} = 0$) and an infinitely steep confining potential allows consolidation of $\gamma_{\rm g}$ and $\beta_{\rm g}$: $\gamma_{\rm g} - \beta_{\rm g} f_c = \eta_{\rm g}(B_1 - B f_c)$, where $\eta_{\rm g} = \beta_{\rm g}/B$

is the only free parameter and $B_1 = n_b\phi_0$ is the field at which $\nu_b = 1$. Then η_g may be extracted from ΔV_g measured at a single f_c with known e^* (we choose $f_c = 1$), and finally used at all other f_c to calculate e^* from each ΔV_g. Performing this calculation for each gate and each data set yields the values shown in Fig. 4(c), approximately e/s for all f_c.

A similar analysis of the charge neutrality equation, assuming fixed gate voltages instead of fixed B, predicts

$$\Delta B = \frac{\phi_0}{rA}, \tag{5.2}$$

where dependence on e^* has been absorbed by taking $e^* = e/s$ (justified by the gate-voltage analysis), leaving A as the only fit parameter. As apparent from Fig. 4(d), where Eq. 2 has been used to extract A from each period in Fig. 4(b), fractional f_c consistently have slightly smaller areas than integer f_c within the same data set, similar to a previous result [49]. The area difference between the two data sets in the 2 μm^2 device reflects the use of less-negative gate voltages for the data set with larger areas.

5.4 Temperature dependence

To study factors that may limit oscillation amplitudes, oscillations as a function of B were measured at a series of mixing chamber temperatures T, and the average frequencies and amplitudes of the oscillations at each f_c were extracted at each temperature. The frequencies are T-independent, but the amplitudes depend strongly on T, as shown in Fig. 5, where each data set is normalized by its value at the lowest temperature. Each data set can be characterized by an exponential decay of the form De^{-T/T_0}, where T_0 represents a characteristic temperature scale. The continuation of this behavior down to the lowest temperatures confirms that the 2DEG was well thermalized to the mixing chamber even for $T \lesssim 10$ mK; furthermore, IQH regime data up to 100 mK (not shown) remain consistent

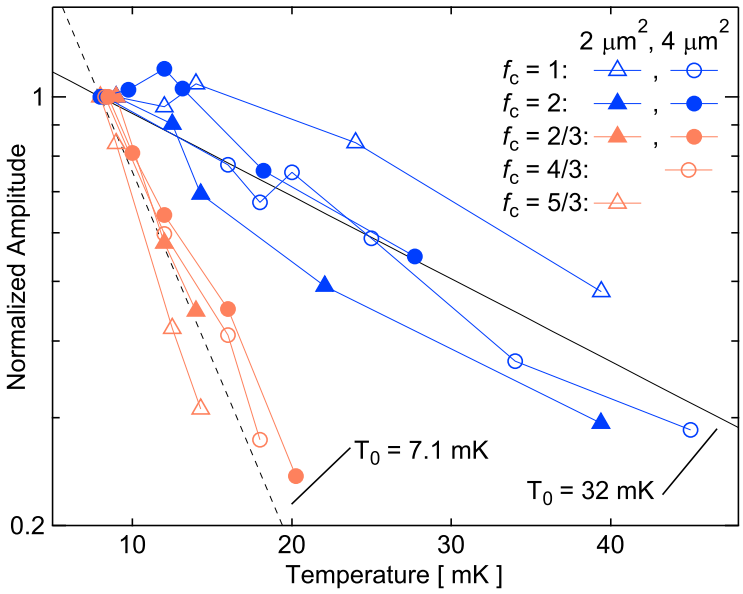

Figure 5.5: Temperature dependence of oscillation amplitude at several filling factors in the IQH (blue) and FQH (orange) regimes. Lines are given by De^{-T/T_0}, with T_0 representing the average value obtained from fits to the individual data sets in each regime. Integer f_c have an average $T_0 = 32$ mK and standard deviation 7.0 mK, while fractional f_c have average $T_0 = 7.1$ mK with standard deviation 1.8 mK; in both cases, any dependence on filling factor or device size is smaller than the measurement uncertainty. Data at $f_c = 4$ were similar to those at $f_c = 1, 2$ and therefore omitted for clarity; data at $f_c = 1/3$ were unobtainable because of device drift. Above 20 mK, FQH-regime oscillations were immeasurably small.

with an exponential dependence, different from the power-law behavior observed in the IQH regime at higher temperatures [96]. The T_0 values differ significantly between the IQH and FQH regimes but otherwise appear insensitive to both f_c and area.

Ref. [82] hints at a physical interpretation of the exponential dependence and the difference in T_0 between the two regimes: T_0 is related to an effective charging energy $E_m = (e^*)^2/C_{\text{eff}}$, where C_{eff} is determined by both the capacitance of the island and edge-structure details[5]. Using this expression with $e^* = e/s$, the measured T_0 yield C_{eff} twice

[5]Specifically, Ref. [82] predicts decay as $e^{-2\pi^2 k_B T/E_m}$; comparison to our model-neutral form gives $E_m = 2\pi^2 k_B T_0$. The large prefactor may explain our ability to resolve $T_0 < eV/k_B$, where $V = R_D I$.

as large in the IQH regime as in the FQH regime. Since T_0 appears insensitive to area, this difference cannot be attributed directly to the area difference between the two regimes; instead, both likely result from a more general structural difference between the IQH and FQH regimes.

5.5 Conclusion

In summary, analysis of gate-voltage periods reveals a quasi-particle charge close to $e/3$ at all FQH states studied, a result that agrees with previous work at $f_c = 1/3$, adds to a complicated story at $f_c = 2/3$, and constitutes the first published value at $f_c = 4/3$ and $5/3$. Magnetic-field periods imply slightly different effective areas for fractional and integer f_c. The temperature scales on which the oscillations decay suggest the existence of further structural differences between the two regimes.

5.6 Acknowledgments

We acknowledge useful discussions with A. Kou, B. I. Halperin, B. Rosenow, and I. Neder, and funding from Microsoft Corporation Project Q, IBM, NSF (DMR-0501796), and Harvard University. Device fabrication at Harvard Center for Nanoscale Systems.

5.7 Epilogue

Temperature dependence measurements in additional devices are discussed in Chapter 6; these results shed light on factors affecting the visibility of both AB and CD oscillations, including a possible role of neutral modes associated with certain FQH states.

Chapter 6

Additional results and closing remarks

This chapter presents additional results and discussions, with a focus on trying to understand and overcome whatever factors limit the strength of the interference.

6.1 Tunneling processes and phase coherence

A challenging aspect of these experiments has been the absence of a clear indication of what tunneling processes are occurring at the constrictions, particularly in cases where oscillations are not observed. As the magnetic field is decreased just past the low-field edge of a plateau, the drop in R_{D} indicates that the outermost fully reflected edge state is starting to be transmitted via a process that should resemble weak forward-tunneling [Figure 6.1(b)]; likewise, at the high-field edge of the plateau, the initial increase in resistance can be expected to arise from a process resembling weak backscattering of the innermost fully transmitted edge state [Figure 6.1(a)].

Somewhere along the riser between each set of plateaus, a crossover between these

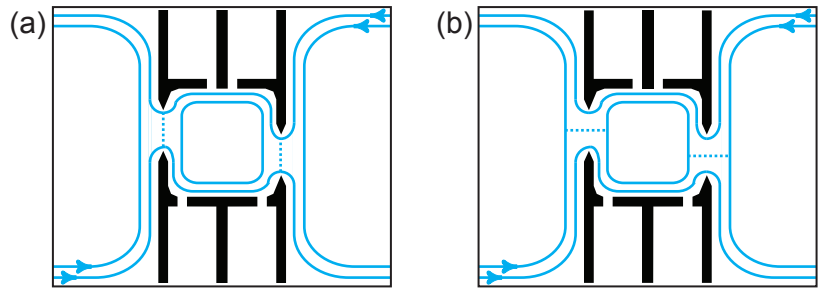

Figure 6.1: Weak backscattering (a) and weak forward-tunneling (b) processes. Process (a), in which the interference would be destroyed by phase-randomization during tunneling, is expected to dominate transport at the high-magnetic-field edges of plateaus in R_{D}, where oscillations are difficult to see; process (b), in which interference should be unaffected by the nature of the tunneling processes, is expected to dominate at the low-magnetic-field edges of plateaus, where oscillations tend to be the strongest.

regimes is expected, but the details of where and how such a crossover occurs remain unknown. Even in the limiting cases, however, there is no guarantee that transport occurs via direct tunneling from one edge to another; instead, a hopping process consisting of several tunneling events may occur, possibly facilitated by disorder. While direct inter-edge tunneling would be expected to preserve phase, hopping via localized states could lead to phase randomization if multiple intermediate states are available, as suggested in Section 1.3.3. Phase-randomization during tunneling processes has strikingly different consequences for the two types of interference processes shown in Figure 6.1: in Figure 6.1(a), phases accumulated at the tunneling sites would affect the relative phase of the interfering trajectories, while in Figure 6.1(b), they would not do so. As a result, phase randomization during tunneling can be expected to reduce the visibility of oscillations arising from a weak backscattering process much more than those arising from a weak forward-tunneling process.

In practice, CD oscillations tend to occur most strongly near the low-field edges of plateaus, where the process of Figure 6.1(b) is expected to dominate. On the other hand, AB oscillations tend to be weaker in this region and stronger in regions where the process of

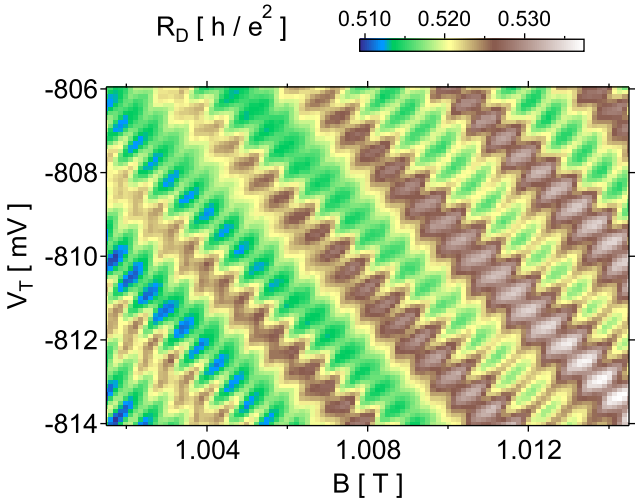

Figure 6.2: Simultaneous AB and CD oscillations in a 2 μm^2 surface-gate-defined device with screening and helper gates (see Section A.2) and 500 nm constrictions.

Figure 6.1(a) is expected to be relevant. These observations and the above considerations appear to suggest that dephasing at the constrictions may play a role in explaining why the AB oscillations are so difficult to see, particularly in the FQH regime.

6.2 When AB, when CD, when both?

Whether AB and/or CD oscillations can be observed depends strongly on wafer parameters and device design. These considerations are discussed in detail in Section A.2. In general, however, the main difference in requirements for observation of AB vs. CD oscillations is that AB oscillations occur only when the constrictions are quite pinched off. In fact, we have never seen AB oscillations in a configuration where the zero-field R_{D} value was less than 1 kΩ, though such a resistance is far from being a guarantee that AB oscillations will appear.

In devices where AB oscillations appear, they are often accompanied by CD oscillations unless Coulomb effects are suppressed by having a large device area and/or a

screening gate. Examples of simultaneous AB and CD oscillations are shown in Figures 6.2 and 6.3. In Figure 6.2, the negatively sloped constant-phase lines with large periods correspond to AB oscillations, while the positively sloped constant-phase lines with small periods correspond to CD oscillations.

In Figure 6.3, the FFT amplitudes associated with AB oscillations (bright features below the red dashed line) remain relatively constant in frequency over the field range of the plot, while those associated with CD oscillations (bright features above the red dashed line) vary significantly in frequency; both behaviors are consistent with the results of Chapter 2. More interestingly, evolution of the oscillation amplitudes with magnetic field can also be observed: the AB features weaken with increasing magnetic field, while the CD features strengthen. In this device and in general, AB behavior tends to be dominant at low magnetic fields ($B \lesssim 1$ T), CD behavior dominates above $B \gtrsim 2$ T, and coexistence of the two is seen primarily in the intermediate field range of $1 - 2$ T. Temperature-dependence results presented in the next section may help explain these observations.

6.3 Additional temperature-dependence studies of interference amplitude

In addition to the measurements presented in Section 5.4, temperature-dependence measurements of oscillations in the IQH and FQH regimes in other devices have recently yielded interesting results.

6.3.1 CD oscillations

It has been suggested that neutral edge modes, expected to propagate much more slowly than charged modes, may reduce the visibility of the CD oscillations associated with

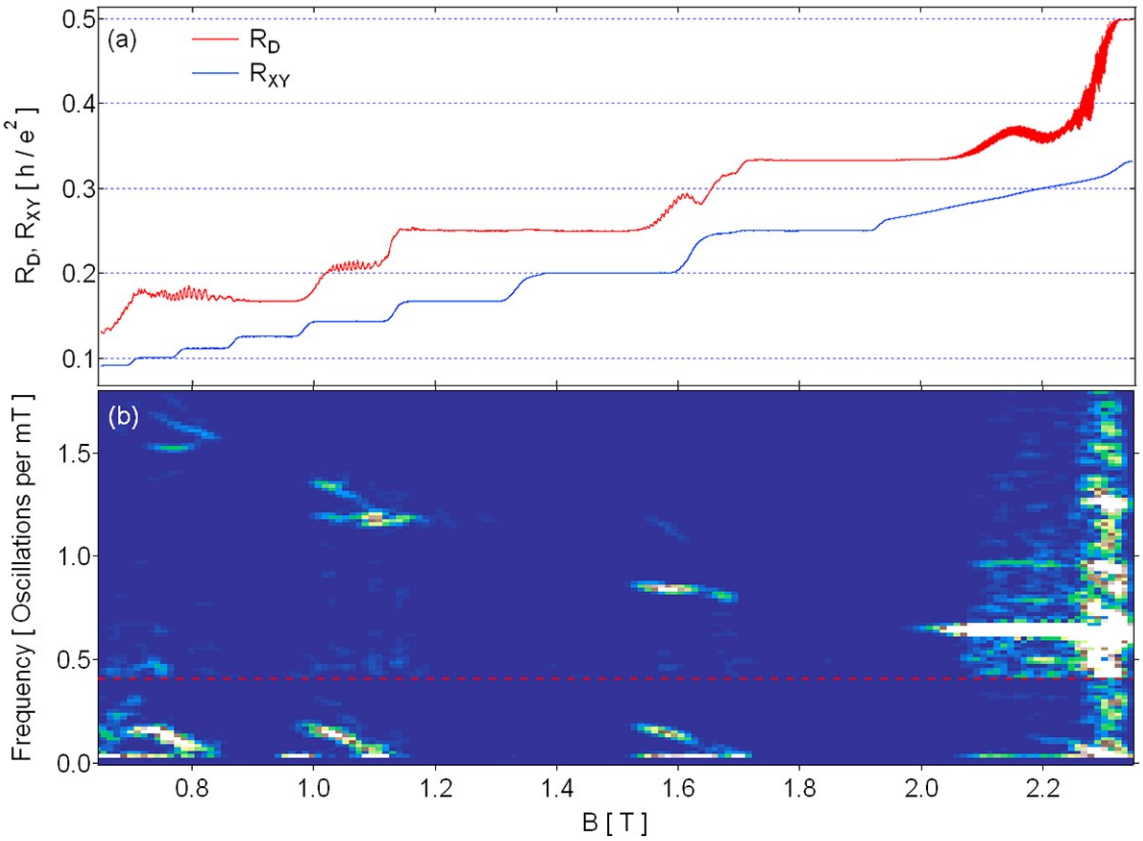

Figure 6.3: AB and CD oscillations in a 2 μm^2 trench-gate-defined device with 600 nm constrictions, with FFT analysis. (a) Diagonal and Hall resistances versus magnetic field; the diagonal resistance shows oscillations with various periods. The horizontal axis is commensurate with that in the bottom panel. (b) Sliding FFT analysis of the diagonal resistance trace in (a), showing simultaneous CD (above the red dashed line) and AB (below the red dashed line) features and their evolution in strength and frequency as a function of magnetic field. Each vertical slice is an FFT performed over a range of approximately 20 mT, with brighter colors indicating larger FFT amplitudes. The amplitude of all data above the dashed red line has been doubled to improve its visibility. The bottom two rows of data have been set to zero since otherwise low-frequency, non-oscillatory features (e.g. corresponding to the relatively gradual increases of R_D between plateaus) would dominate; the features in the third row correspond to the tail end of the non-oscillatory behavior.

the FQH states at which they are present. One signature of this effect would be a difference in the temperature scale T_0 (see Chapter 5) between oscillations at $f_c = 1/3$, where neutral modes should be absent, and those at other f_c such as 2/3, where they may be present. The experiment is complicated by the fact that observation of $f_c = 1/3$ oscillations in our

devices requires more-negative gate voltages than typically used; hence, care must be taken to disentangle the effect of f_c from any effect of the significant change in gate voltage. Preliminary measurements, some of which are shown in Figure 6.4, reveal two main facts: (a) more-negative gate voltages lead to higher T_0, as seen here for $f_c = 2/3$; and (b) even in the same gate-voltage configuration, T_0 is much higher at $f_c = 1/3$ than at 2/3, possibly a signature of neutral modes at 2/3. If this interpretation is correct, the similarity of T_0 across all measured fractional f_c other than 1/3, a feature seen both here and in Chapter 5, would suggest that all support neutral modes, at least for the wafer and devices used for these measurements. Other explanations may be possible though, and so further studies, such as reproducing this result in devices with a variety of areas and constriction sizes, would be useful. Concerning the increased T_0 that appears to result from more-negative gate voltages, a more-detailed study looking at each gate's individual effect on T_0 would be useful for interpreting this result and possibly learning how to improve T_0 even further.

6.3.2 AB oscillations

Like CD oscillations, AB oscillations also decay exponentially in amplitude as a function of temperature. The characteristic temperature associated with this decay has been found to depend on magnetic field in a way similar to the energy scale associated with the decay in Chapter 3. In particular, both data sets are consistent with a $1/B$ dependence of the relevant energy scale, as shown in Figure 6.5, though more data would be useful to confirm the functional form. An understanding of the reason for this magnetic field dependence would likely be a critical step toward observing AB oscillations in the FQH regime if possible.

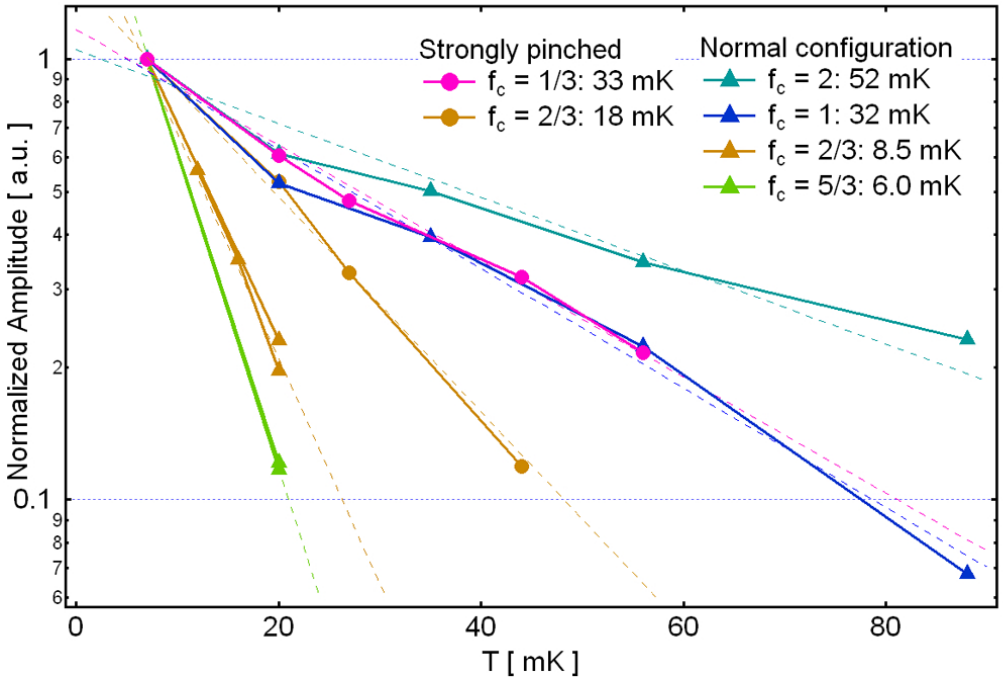

Figure 6.4: Temperature dependence of CD oscillations in two configurations of the same device: a normal configuration with moderate gate voltages, and a configuration in which the gates are pinched off more strongly to allow observation of oscillations at $f_c = 1/3$. The values of T_0 associated with each f_c are calculated using the method of Chapter 5.

6.4 Outlook

Although much attention is rightly focused on the possibility of observing non-Abelian statistics at the $\nu = 5/2$ state, it is clear that the behavior of electronic Fabry-Perot interferometers still holds many other secrets. These unknowns not only stand in the way of using these devices to study the 5/2 state, but also represent compelling physics problems in their own right. The work presented in this thesis sets the stage for additional experiments addressing these questions, some of which are now discussed.

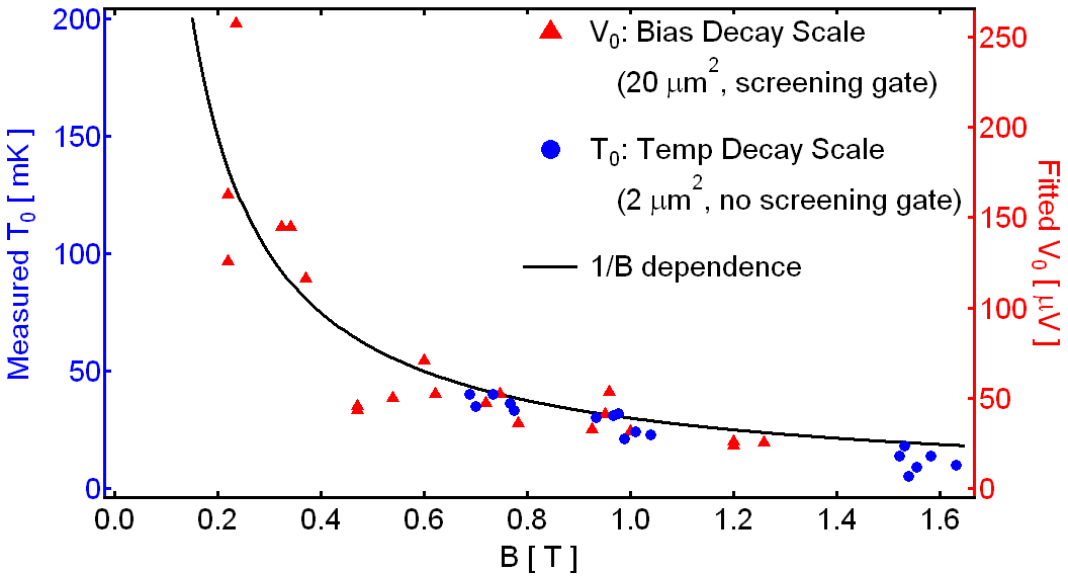

Figure 6.5: Temperature and bias scales on which AB oscillations decay plotted as a function of magnetic field. The similarity of the behavior is particularly notable given the fact that the two data sets are taken from very different devices.

6.4.1 Parameter-space explorations

Although AB oscillations have not yet been confirmed at any FQH states, and CD oscillations have been seen over a fairly narrow range of device and material parameters, the devices and materials studied so far represent a small sliver of vast, many-dimensional space of possible parameters. Even a partial list of such parameters is daunting: device area and shape; constriction length and width; possible use of helper or screening gates of various shapes and positions; possible use of trenches of various depths; positive or negative gate bias during cooldown; 2DEG density, mobility and thickness; use of doping wells, screening wells and extra donor layers; use of illumination; and even use of non-GaAs 2DEG or even 2DHG systems. While some of these potential avenues for exploration would be unlikely to lead directly to the observation of new AB or CD oscillations in the FQH regime, almost all of them could lead to an improved understanding of existing oscillations

and their limitations.

Exploring such a large parameter space requires a careful strategy. The most conservative would be to start from known good parameters (e.g. those used for the devices in Chapter 5) and try slight variations in one or two continuous parameters at a time (e.g. trench depth and constriction width) in an attempt to optimize the existing interference and possibly observe interference at additional FQH states; this local-optimization approach would likely be useful in understanding which parameters limit the amplitude of the oscillations, but by itself would be unlikely to lead to groundbreaking discoveries. A slightly more aggressive strategy would be to make a more dramatic change in a certain device or wafer parameter (e.g. make a device with both trenches and helper gates) and evaluate the resulting effect on the oscillations. Perhaps the most aggressive strategy would be to change a fundamental aspect of the experiment, such making the devices on graphene or measuring them using high-frequency techniques; such methods might be incompatible with $\nu = 5/2$, but could potentially lead to dramatic improvements in observing FQH-regime interference, possibly even of the AB type.

6.4.2 Physics of AB oscillations

The behavior of AB oscillations observed to date is troubling from the point of view of hoping to see them in the FQH regime: they weaken significantly at high magnetic fields, and they require strongly pinched-off constrictions. In short, they appear best in configurations incompatible with FQH states. The good news is that the reasons for both of these constraints are not understood, and further study might lead to ways to circumvent them. It seems clear that the shape of the potential in the constrictions plays an important role in determining the amplitude of AB oscillations and the degree of pinch-off needed to observe them, but the specifics remain unclear. Careful studies of the temperature-

and field-dependence of the AB oscillation amplitude, as a function of each of the various parameters affecting the shape of the potential in the constrictions, could potentially lead to significant improvements in both the strength of AB oscillations and our understanding of them.

The ability to measure edge velocities from the AB oscillations provides a rare quantitative measurement of the slope of the confining potential. Our measurements so far have yielded negligible dependence of the inferred confining potential slope on the presence or absence of screening gates, doping wells and trenches, in apparent contradiction to the observations that a) trench-defined constrictions have an electron density much closer to the bulk's than do gate-defined constrictions of the same lithographic size, especially in doping-well materials, and b) constrictions with grounded helper gates are much more difficult to pinch off than ones without helper gates. A possible explanation for the discrepancy is that the observation of AB oscillations has always required significant negative voltages on the side gates, and so in the regime where velocities can be measured, these gates have the a dominant effect on the shape of the confining potential. To test this hypothesis, one could take our standard trench-defined design and modify it in one of two ways: either make one with small enough constrictions that minimal gate voltages are needed to induce AB oscillations, or make one in which the gates defining the constrictions have a negligible impact on the confining in the rest of the device. In either device, the edge velocity could be extracted from AB oscillations in two regimes: at minimal side-gate voltages, where the confining potential is expected to be dominated by the trenches, and at more negative side-gate voltages, where the confining potential is expected to be dominated by the gates. A difference in inferred velocity between the two regimes would not only provide further evidence for the model presented in Chapter 3 but would also shed light on processes limiting coherence: if the edge velocity is a limiting factor, then higher velocities should be

correlated with larger visibilities.

6.4.3 FQH-regime complications

In the FQH regime, expanding the set of fractions at which CD oscillations are observed should be relatively straightforward once the limiting factors are understood. Possible limiting factors include the charging energy (proportional to the square of the quasi-particle charge), presence of neutral modes, and FQH-state energy gaps. A major step toward understanding the relative importance of each of these factors would be achieved by observing CD oscillations (and most importantly their temperature dependence) at $f_c = r/5$ for $r = 1$ (where neutral modes should be absent) and at least one of $r = 2, 3, 4$. Observation of oscillations at $f_c = r/3$ and $f_c = r$ in the same device and with the same gate-voltage settings would be ideal, and should be possible.

Observation of AB oscillations in the FQH regime might be prevented not only by the factors uncovered in the IQH regime, but also fluctuations in the number of enclosed anyonic quasi-particles on timescales faster than those on which measurements are performed. Measurements on much faster timescales using high-frequency techniques might shed light on whether such fluctuations are an issue.

Finally, given the strong temperature dependence of CD oscillations in the FQH regime, it would be very interesting to perform similar measurements in a dilution refrigerator with an adiabatic nuclear demagnetization stage, in which 2DEG temperatures on the order of 1 mK or less can in principle be achieved. Recent progress in this field suggests that such measurements could be feasible soon.

Appendix A

Device fabrication: considerations and techniques

When everything is working perfectly, the process of creating a chip with finished devices from a bare wafer is fast, enjoyable, and satisfying (see the nice example in Figure A.1). Unfortunately that often isn't the case, since there are many steps and many things that can go wrong at each step. In the end, the fabrication process almost always works, but it requires careful attention up to the very last step. In the following sections, I will explain not only the fabrication recipes I used, but also various failure modes that I encountered and how to spot and avoid them. Many of these procedures are based on ones used by Jeff Miller, described in great detail in his thesis [158]. Additional information about the physics of GaAs ohmic contacts can be found in Look [21], and more information about that subject and many other aspects of these procedures can be found in Williams [159]. I recommend all three references for anyone just starting to process and measure GaAs wafers.

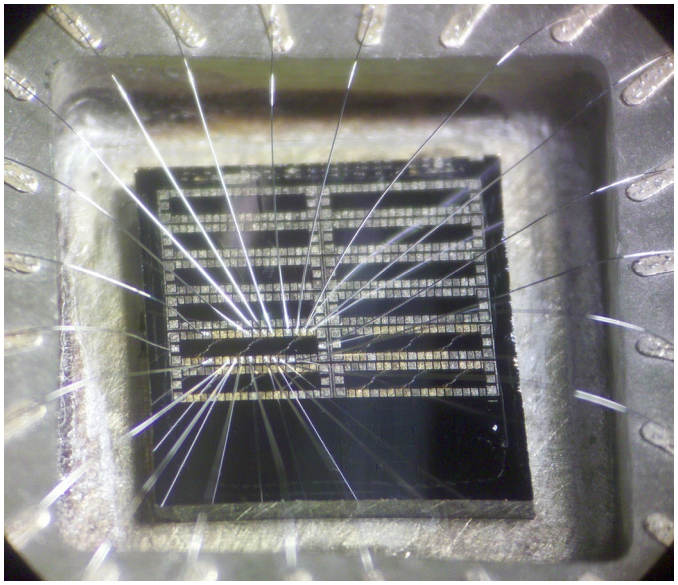

Figure A.1: Close-up view of a GaAs chip after wire-bonding, illustrating the high density of Hall bar mesas (up to 16 on a typical chip) and devices (up to 3 per mesa) achieved using the fabrication recipes described in this appendix.

A.1 Wafer parameters

As illustrated back in Figure 1.3, all modern high-mobility GaAs 2DEG heterostructures look fairly similar to some extent. In fact, all of the 2DEG's used for these experiments reside in structures resembling one of the two shown in Figure 1.3(d): modulation-doped [160] quantum-well (QW) structures with or without doping wells. Of course, there are still many growth parameters that can be varied within either of these designs: the thickness of the QW, the distance between the donors and the QW, the density of the donors, and the fraction of Al used in the AlGaAs layers (which need not be constant throughout) are some of the main parameters. In some recent structures, additional doping layers or narrow GaAs wells have been added in order to improve screening of the 2DEG from sources of disorder, chiefly the surface and donor layers.

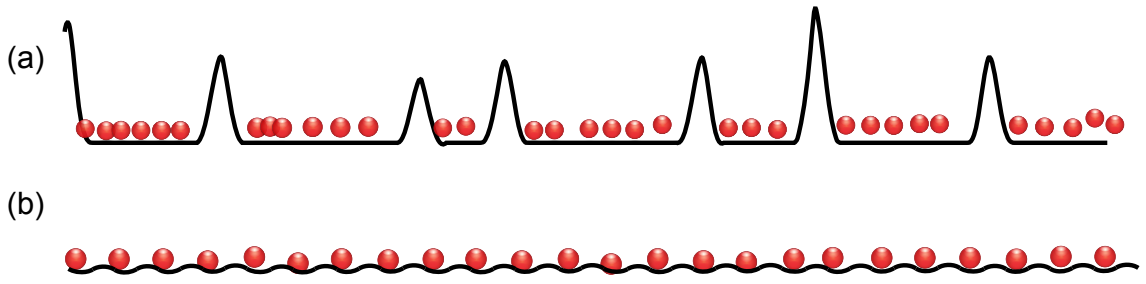

Figure A.2: A cartoon drawing indicating the effects of different types of impurities on the disorder landscape in high-mobility 2DEG's. (a) Background impurities are relatively spread out but lead to strong backscattering. (b) Ionized donors create a relatively shallow potential, but occur with greater regularity, resulting in a shorter correlation length.

A.1.1 Mobility and FQHE quality

The great progress made in the study of the FQHE and especially the 5/2 state over the last few decades has been possible mainly because of concurrent progress in techniques for growing GaAs heterostructures, which can now support 2DEG's with mobilities approaching 40×10^6 cm^2/V $\cdot$ s. As discussed in Section 1.2.3, the mobility is limited by scattering, which may in principle occur at defects, background impurities, donors, other electrons, interfaces, and thermal phonons, though thermal phonons are negligible in the temperature range of interest.

In modern high-mobility 2DEG's, defects and background impurities appear to limit the mobility [22], but growing evidence [20] suggests that they no longer limit the strength of FQHE states. Instead, it has been suggested [20, 161] that the disorder potential from the donors may be a limiting factor: as illustrated in Figure A.2, the mobility could be limited by relatively infrequent large-angle scattering from background impurities, while the inter-electron correlations leading to the FQHE could be limited by shallow-angle scattering on shorter length scales associated with the donors.

A.1.2 Doping wells vs. illumination

One ingredient that has proved essential for the observation of weak FQH states like the one at $\nu = 5/2$ is the presence of delocalized electrons in the donor layers, which facilitate screening. When Si donors are placed directly in the AlGaAs spacer, many of the electrons they donate are tightly bound by DX centers [162], resulting in poorer screening and a lower 2DEG density than would be achieved if these electrons were mobile. To overcome this problem, it has become common practice to illuminate the sample with a red LED at some point during the cooldown in order to excite the electrons out of these deep levels. As an alternative strategy, however, the Si donors can be placed in ultra-narrow GaAs layers ("doping wells"), in which case the donated electrons are mobile even without the use of illumination. In these samples, the sensitive FQHE and RIQHE features in the second Landau level can approach the quality of those seen in illuminated samples without doping wells. One benefit of this approach is that it seems to allow more stable gating, a critical property for creating tunable, confined geometries. Un-illuminated samples without doping wells, though, have by far the most stable gate responses, and can still be used for studies of strong FQH states in the lowest Landau level.

A.1.3 Choice of wafers for these experiments

Since doping wells provide a balance of decent gating and good FQH states, most of the wafers measured in the experiments presented in this thesis used doping wells. The only exception is the set of experiments presented in Chapter 4; in fact, for reasons that remain unclear, these DNP effects appear to be weaker and shorter-lived in materials with doping wells than in those without. A detailed list of wafers and devices used for all experiments is presented in Appendix D.

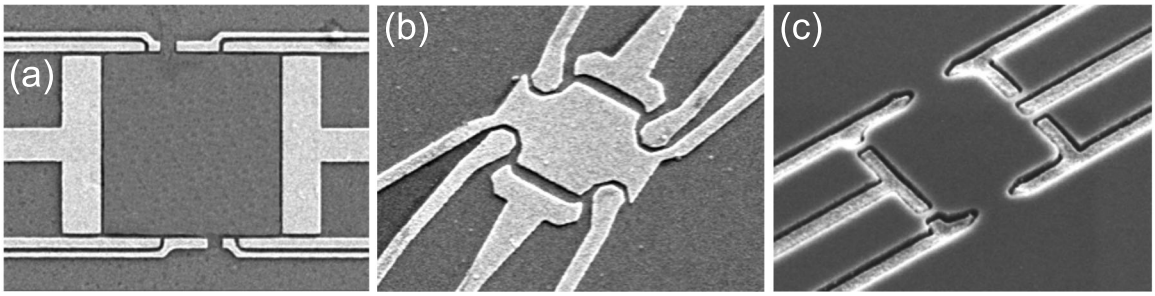

Figure A.3: Sample images of a few different styles of devices. (a) A surface-gate defined interferometer with "helper" gates over the constrictions. (b) A surface-gate defined interferometer with a large "screening" gate. (c) A trench-gate defined interferometer.

A.2 Device parameters

Though the fabrication is fairly straightforward, design of electronic Fabry-Perot interferometers requires careful consideration of many parameters including device area and shape, constriction size and shape, presence or absence of "helper" [Figure A.3(a)] or "screening" [Figure A.3(b)] gates, and depth of trenches, if any [Figure A.3(c)]. Several factors affect the choice of device parameters: type of interference desired, strength of relevant quantum Hall states, and wafer structure. In this section we discuss these considerations.

A.2.1 Benefits and limitations of trenches

Since high-mobility GaAs 2DEG's are typically located 200 nm or more below the wafer surface, surface gates are generally unable to create a 2DEG confining potential that changes significantly over length scales much smaller than that [163], as illustrated in Figure A.4. This limitation, which makes it difficult to create micron-scale devices in which the electron density matches that in the bulk, can be overcome by depositing the gates in etched trenches rather than on the surface, bringing them closer to the 2DEG. Empirically, we find that etching just past the upper donor layer in doping-well materials allows the formation of constrictions as small as about 750 nm in which the density matches

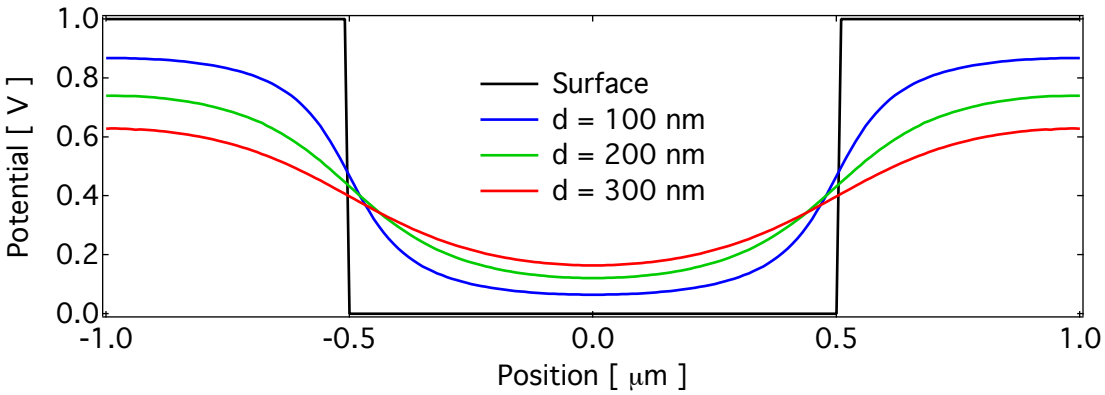

Figure A.4: Calculated confining potential produced by surface gates at 1 V for several values of 2DEG depth d. This calculation does not take into account screening from the 2DEG, and assumes that the surface potential in the region between the two gates is 0 V.

that in the bulk and good FQH plateaus are observed. Similar-sized constrictions defined by surface gates generally show a much lower density and poor or no FQHE features once the gates are depleted. In non-doping-well materials, trench gates reduce the density and FQHE quality in constrictions slightly, though not nearly as much as surface gates.[1]

An additional benefit of trenches appears to be improved stability. In un-illuminated doping-well materials with surface gates, significant drift and hysteresis are observed, as well as frequent sudden switching events (every few minutes, particularly after gates have been tuned significantly), and in illuminated non-doping-well materials with surface gates, switching has been so frequent that we have been unable to observe periodic oscillations. The use of trenches improves the performance in both materials: in un-illuminated doping-well materials, some drift is observed, but very few sudden switches; in illuminated non-doping-well materials, significant drift and occasional switches still occur, but periodic oscillations are readily observed.

[1] As an alternative to trenches, "annealing" surface gates on doping-well materials by depleting them at 4 K can also produce constrictions in which the density and the FQHE quality nearly match that of the bulk [35]. Unlike trenching, annealing has no effect on non-doping-well materials in our experience.

Although trenches thus appear to be beneficial, they are not a panacea, and their exact effect on the confining potential remains poorly understood. We have found that a potential favorable for CD oscillations in the FQH regime is created by etching just past the upper donor layer, but only in materials with densities ranging from $1.5 - 2 \times 10^{11}$ cm^{-2} and 2DEG depths between 200 and 300 nm, and only in materials with doping wells. We have not seen these oscillations for any other combination of material or device parameters. Further study of the confining-potential effects of parameters such as 2DEG density and depth, trench depth, and the presence of absence of doping wells, would likely shed light on possible ways to extend the parameter range over which these oscillations can be observed, potentially at even weaker fractions. Measurements of the shape of the confining potential are of course difficult, but some clues can be gleaned from measurements of edge velocities in the drift regime [164], depletion lengths inferred from IQH- and FQH-regime oscillations [165], and imaging studies [96].

A.2.2 Effect of device dimensions on type of interference

In our experience, pure AB interference, which is seen only in the IQH regime, can be observed in devices as large as 20 μm^2 (the largest we've measured), but requires the constrictions to be quite small: less than about 500 nm, or slightly larger if trenches are used. If helper gates are used, then even more negative side-gate voltages and/or even smaller constrictions are needed. No other systematic dependence of the strength of the AB oscillations on any other device parameters has been established.

Coulomb-dominated interference is readily observed in devices smaller than about 10 μm^2, though the presence of a screening gate reduces the allowed device area somewhat. In the IQH regime, these oscillations tolerate a variety of constriction types, and sizes ranging from 250 nm up to almost 1 μm. In the FQH regime, however, a smaller range of

constriction sizes, typically $500 - 750$ nm, is required, in addition to the trench-depth and wafer-structure constraints mentioned in the previous section.

A.3 Mesa and ohmic contact formation

To begin processing, a nearly square chip with sides of about 5.7 mm is cleaved off of a wafer. Cleaving GaAs is easiest along certain crystal axes; typically we cleave along the same axes as the major and minor flats of the wafer.

A.3.1 Mesa patterning and etching

The mesa patterning and etching process is well-suited for photolithography: the mesa features are micron-sized or larger, and the etch solution does not attack photoresist. Our initial recipe called for etching to a target depth just past the donor layer immediately below the 2DEG, but further testing revealed that a shallower etch, e.g. just past the donor layer immediately above the 2DEG, was sufficient to isolate the mesas at low temperatures and provided the added benefit of much lower room-temperature gate resistances (tens of kΩ instead of tens of MΩ), reducing the likelihood of device damage from electrostatic discharge. A target depth roughly 1.2 times the depth of the donor layer immediately above the 2DEG seems to work consistently well. Our standard procedure is as follows:

1. Solvent clean: 5 min each in trichloroethylene (TCE), acetone, isopropanol (IPA), and deionized water (DI), with sonication, then blow dry with nitrogen
2. Bake: 5 min at 180° C to drive off any remaining moisture
3. Spin: Microposit S1813 photoresist for 45 s at 5000 rpm
4. Bake: 2 min at 115° C
5. Align and expose: 4 s on the AB-M mask aligner

6. Develop: Microposit MF CD-26 for 20 s in one beaker and 25 s in a second beaker, with agitation throughout, followed by 15 s rinse in DI water
7. UV-ozone clean: 45 s in Samco UV & Ozone Stripper
8. Measure: height of resist using Dektak Profilometer
9. Etch: in 240 mL DI water, 8 mL H_2O_2 and 1 mL H_2SO_4, aiming to reach about 3/4 of the way to the target depth assuming an etch rate of 3 nm/s
10. Measure: height of resist again, compare with original height, and continue etching and measuring until within about 10% of the target depth
11. Strip resist: 10 min in acetone, with sonication, followed by IPA rinse and nitrogen blow dry

Potential problems

This is a very reliable process, but there are a few things to watch out for. Photoresist edge-bead can prevent the mesas along the chip edges (especially at the corners) from being fully isolated. This problem can be avoided by slightly increasing the chip size, but chips larger than 5.7 mm on both sides are difficult to remove from the sample holder. With careful alignment, 5.7 mm on a side should be adequate. A second pitfall is the occasional formation of bubbles at the spots where the tweezers touch the chip, which can prevent adjacent regions of the chip from being etched. One should be wary of this possibility not only during this etch process, but whenever the chip is held in a liquid using tweezers.

A.3.2 Contact patterning, evaporating, and annealing

After mesa patterning, the next step is to pattern the ohmic contacts and gate bonding pads, mainly since these features need to be annealed at temperatures that would smear out the small features defining the interferometers. Although the contact and bond

pad features are comparable in size to the mesa features, the need for a lift-off process instead of an etching process complicates the choice of lithography method. Since previous work in our group revealed that the standard photolithography lift-off process reduced the 2DEG mobility [158], we adopted an electron-beam lithography recipe despite the large feature size.

1. Standard solvent clean and bake as described in Section A.3.1.
2. Spin: MicroChem PMMA 495 C6
3. Bake: 4 min at 180° C
4. Spin: MicroChem PMMA 495 C6
5. Bake: 6 min at 180° C
6. Spin: MicroChem PMMA 950 A4
7. Bake: 8 min at 180° C
8. Pattern in the Elionix ELS-7000: acceleration voltage 100 kV, beam current 25 nA, 600 μm write field, 20,000 dots, dose 1400 uC/cm^2 for alignment marks and 1200 uC/cm^2 for the ohmic contacts and gate pads
9. Develop: 90 s in 1:3 MIBK:IPA developer, then 15 s rinse in IPA followed by nitrogen blow dry
10. UV-Ozone clean: 80 s in Samco UV & Ozone Stripper
11. Prepare evaporator: vent, check crystal life, and insert metals for the appropriate recipe (see discussion of evaporator and annealer recipes below)
12. Remove oxide: dip in NH_4OH for 5 s, then rinse in DI water for 10 s
13. Evaporate: immediately, following an appropriate recipe for the wafer
14. Lift off: in acetone for a few hours or more
15. Finish liftoff: sonicate in short pulses until unwanted metal is removed, then rinse

with acetone and IPA, then blow dry with nitrogen

16. Anneal: using the appropriate recipe in the Modular Process Technology RTP-600xp rapid thermal annealer

Evaporator and annealer recipes

We have used two main contact recipes with good success, one involving e-beam evaporation of Pt-Au-Ge and the other involving thermal evaporation of Ni-Au-Ge. The Ni-Au-Ge process seems slightly more reliable, but the Pt-Au-Ge process tends to produce lower-resistance contacts. Regardless of the evaporation recipe used, the deposited metal is annealed (*after* liftoff) in a forming gas atmosphere in a Modular Process Technology RTP-600xp, at the time and temperature listed below the evaporation recipe.

Pt-Au-Ge Pt-Au-Ge contacts are deposited using e-beam evaporation. The following recipe, developed by Jeff Miller, has provided good contact to 2DEG's with densities ranging from $1.5 - 3 \times 10^{11}$ cm^{-2} and located from $150 - 300$ nm below the wafer surface.

1. Pt, 5 nm
2. Au, 200 nm
3. Ge, 100 nm
4. Pt, 73 nm
5. Au, 100 nm
6. Ge, 50 nm
7. Pt, 55 nm

Anneal at 530° C for 100 s.

Ni-Au-Ge Pt-Au-Ge contacts are deposited using e-beam evaporation. The following recipe, acquired from Vivek Venkatachalam, has provided good contact to 2DEG's with densities ranging from $1.5 - 3 \times 10^{11}$ cm^{-2} and located from $150 - 300$ nm below the wafer surface.

1. Ni, 6 nm
2. Ge, 135 nm
3. Au, 270 nm
4. Ni, 40 nm
5. Au, 25 nm

Anneal at 460° C for 60 s.

For 2DEG's deeper than 300 nm below the surface, which typically have electron densities less than 1.5×10^{11} cm^{-2}, we have had success doubling the thickness of every layer of the Ni-Au-Ge recipe, and annealing for 25% longer.

Potential problems

We have experienced several problems with these recipes over the years. Since e-beam evaporators use crucibles shared by many users, contamination can be and has indeed been a problem. We have not had any problems attributable to contamination since switching from crucibles shared by all cleanroom users to ones shared just by Marcus Lab members. In the thermal evaporation recipes, Ni can be problematic. If the same boat is used for more than a couple of evaporations, alloying of the Ni with the tungsten may cause the boat to break. Even if an alumina-coated boat is used, holes also appear after a couple of evaporations. Since Ni and boats are both extremely cheap compared to the other evaporator metals, the GaAs wafers, and the time spent in the cleanroom, we adopted a

standard procedure of using a fresh Ni boat for each Ni-Au-Ge evaporation. Finally, with all of these recipes, it is important to use an evaporator with a chilled sample holder, since the length of the evaporations will otherwise heat the sample significantly, causing the resist to flow and possibly even hard-bake.

In addition to evaporation-related problems, we have also experienced chemical-related problems, generally in the form of residue on the surface that becomes impossible to remove. Usually this residue does not pose a problem, but it can if it is located where a device or other feature would go. Regularly inspecting chips in a scanning electron microscope (SEM), even when things appear to be going well, can be useful for detecting changes in chemical-residue contamination levels. Since the SEM beam can also deposit contaminants onto the chip, it is best to image at low magnifications and in areas far from devices to be measured.

A.3.3 Minimal processing: soldered indium contacts

Since chemicals used in processing may damage or leave residue on the GaAs wafer, it is sometimes useful to make ohmic contacts to a chip without the use of such chemicals. Furthermore, while alloyed contacts can achieve resistances as low as 20 Ω, each particular alloyed-contact recipe will work for some 2DEG's but not others. Considering both of these factors, when evaluating a new wafer it is often useful to make contacts using soldered indium, which has the advantages of working for all GaAs 2DEG's and not requiring the use of any chemicals besides acetone and isopropanol.

After cleaving the chip, this recipe has only three steps. The first is a solvent clean, typically just acetone for $10 - 15$ min followed by a quick rinse in isopropanol or methanol, then blow dry with nitrogen gas. While the chip is cleaning, place pure indium wire, or indium-tin alloy, in HCl to remove any oxide on the surface. When the rate of

bubble formation on the wire becomes negligible, rinse it with DI water and then blow dry with nitrogen gas.

Use a dedicated soldering iron with a gold-plated tip[2] and adjustable low power to melt the wire onto a glass slide in order to make it easy to pick up a small amount at a time. Use the minimum amount of power needed to get the indium to flow. Mount the chip onto a sample holder that can be easily clamped under a low-power microscope with a long working distance; I use a drop of PMMA to attach it to an aluminum block. Again using the minimum amount of power needed, pick up a small amount of indium from the slide and transfer it to an edge or corner of the chip. Repeat as needed to make all of the contacts desired. It should be possible to keep the contact size less than 200 μm across. Sometimes the indium does not wet the GaAs very well; in that case the contacts may pop off entirely when the chip is handled. Prodding each contact with tweezers before putting the soldering iron away is therefore useful; if a contact does fly off, re-do it, possibly with higher power and longer time.

Once all the contacts have been placed and seem to be well attached, remove the chip from the block, do a quick solvent rinse and blow dry, and then anneal at 440° C for approximately 5 min. Minor discoloration of the contacts during annealing is normal. Wire-bonding to these contacts may be difficult, as indium is very soft and will be compressed by the force from the tip. Persistence will pay off, however, as it can only be compressed so far before providing sufficient resistance.

Potential problems

The main difficulties are associated with trying to make contacts on small samples (less than about 4 mm on either side). Smaller samples require the contacts themselves to

[2]If previously used, the tip should also be cleaned in the HCl.

be kept proportionally smaller and better-aligned in order to prevent mixing of R_{xx} into R_{xy}. In attempting to achieve the required precision, one tends to hold the soldering iron on the GaAs surface for a shorter amount of time than would be ideal, possibly resulting in poor wetting of the GaAs surface by the indium. Good wetting of the surface, necessary for the formation of good contacts, is usually signaled by a shallow contact angle between the indium and the chip.

A.4 Interferometer fabrication recipes

The interferometer fabrication recipe underwent more changes than any other aspect of the wafer processing over the course of my research. The initial procedure, described in Jeff Miller's thesis, required careful attention to the e-beam dose, especially for devices involving a screening gate. A second generation, using a cold-developing procedure to improve the reliability of patterning such fine features, had a tendency to leave a layer of resist on the chip surface, leading (somehow) to sudden pinch-off of gates on wafers known to have good gating properties. The version presented here has been extremely reliable, giving a yield near 100% for surface-gate devices, trench-gate devices, and even hybrid devices in which the surface gates, written in a subsequent e-beam step, must be aligned to the trench gates with precision on the order of 10 nm.

A.4.1 Surface gates

1. Standard solvent clean and bake as described in Section A.3.1
2. Spin: MMA (8.5) MAA EL 6 for 45 s at 4000 rpm, with 4000 rpm/s acceleration
3. Bake: 8 min at 180 ° C
4. Spin: a prepared 1:1 mixture of ZEP 520 and Anisole for 45 s at 5000 rpm, with

1500 rpm/s acceleration and dynamic spin-on at 100 rpm

5. Bake: 5 min at 180 ° C
6. Optional (but I usually do this): Spin and bake a second ZEP/Anisole layer if etching $\sim$ 100 nm or more. In this case, the bake after the first ZEP/Anisole layer can be reduced to 4 min.
7. Pattern in the Elionix ELS-7000:
   - Small features: acceleration voltage 100 kV, beam current 25 pA, 75 μm write field, $60,000$ dots, dose 475 uC/cm^2
   - Large features: acceleration voltage 100 kV, beam current 300 pA, 300 μm write field, $60,000$ dots, dose 475 uC/cm^2
8. Alternatively, pattern both large and small features in one step in the Elionix ELS-F125: acceleration voltage 125 kV, beam current 500 pA, 600 μm write field, $240,000$ dots, dose 600 uC/cm^2
9. Develop: for 20 s in o-xylene (to develop ZEP), then 40 s in 1:3 MIBK:IPA (to develop MMA), and then rinse for 15 s in IPA and blow dry with nitrogen
10. Evaporate: 5 nm Ti or Cr followed by 15 nm Au. E-beam evaporation produces somewhat nicer-looking gates than thermal evaporation.
11. Lift off: in a mixture of acetone and TCE for at least a few hours
12. Finish liftoff: sonicate in short pulses until unwanted metal is removed, then rinse with acetone and IPA, then blow dry with nitrogen

Potential problems

When writing on the ELS-7000, the large features span multiple write-fields. Occasionally the stitching is not quite good enough to connect the features in adjacent write-

fields, so we typically include a layer of patches at the write-field boundaries. The patch layer is of course written with different write-field boundaries, typically with the new write-fields centered on the corners of the old ones.

A.4.2 Trenched gates

Since the lateral spacing between gates is typically of the same order of magnitude as the desired etch depth, isotropic etching would cause the trenches to run together, and therefore anisotropic etching is preferable. Anisotropic etching of GaAs/AlGaAs is most easily accomplished using a reactive ion etch (RIE), which can give trenches with vertical walls and flat bottoms under the right conditions. Since the RIE may leave a rough surface and even embed impurity atoms into the wafer, both of which could adversely affect the device performance, we follow the dry etch with a shorter wet etch before depositing metal. Being isotropic, the wet etch has the added benefit of facilitating lift-off since it creates a slight undercut profile rather than a vertical one.

The process is identical to the surface gate lithography process except for the addition of the dry and wet etch steps and the deposition of a thicker metal stack. To start, clean the chip, spin the resist, write the pattern, and develop the features exactly as described in Section A.4.1. Prior to metal deposition, perform a dry etch followed by a wet etch as described below. Then deposit 10 nm of Ti or Cr followed by enough Au that the metal stack fills about 80% of the expected trench depth. Finally, lift off as usual.

Dry etch

The reactive ion etch is performed in the Unaxis Shuttleline Inductively Coupled Plasma RIE machine. Prior to sample insertion, an O_2 plasma clean should be performed using the machine's standard O_2 plasma recipe for at least 15 min, and the sample holder

should be allowed to cool to a temperature that will not cause the resist to flow when the chip is placed on it. Cooling of the sample holder can be sped up greatly by removing it from the machine and placing it on a flat surface. Once the sample holder is ready, a small blob of silicone gel should be placed in the middle of it, and the chip placed on top of the blob and pushed down until nearly flush with the sample holder. Any silicone gel that has oozed out from between the sample and the sample holder should be removed, since the RIE process can splatter it onto the chip.

The etch itself uses a mixture of BCl_3, Ar and N_2, flowed at 15, 7.5 and 3.75 SCCM, respectively, with a target pressure of $2.5 - 3$ mTorr. Substrate cooling should be active to maintain the sample holder near room temperature. The gas flow should be allowed to stabilize for 30 s before turning on the acceleration power to 150 W and igniting the plasma with 500 W. The etch rate is typically about 4 nm/s, so for typical samples we etch for on the order of 30 s. After both power sources are turned off to stop the etch, the chamber should be purged with Ar for 3 min before transferring the sample out.

Wet etch

The wet etch is done using a mixture of 200 mL DI water, 6 mL H_3PO_4, and 2 mL H_2O_2. The etch rate seems to vary significantly with temperature, so it is often helpful to prepare the mixture at least 15 min in advance since the air temperature tends to vary less than the DI water temperature in the CNS cleanroom. With an expected etch rate of 20 nm/min, the chip is typically etched for approximately 45 s, then rinsed in DI water for 30 s before being blown dry with nitrogen.

Potential problems

If the desired etch depth is short enough that it requires an etch time of less than 20 s, reproducibility may suffer from the fact that the ramp-up of the two power supplies happens over a few seconds and seems to vary a bit over time. If precise control over the etch depth is desired, a possible strategy might be to consider the use of a recipe that selectively etches GaAs but not AlGaAs or vice versa. For example, addition of SF_6 to the BCl_3 mixture is known to reduce its ability to etch AlGaAs dramatically.

The variability of the wet etch rate seems mostly related to the temperature of the etch solution, but other factors, such as the precise composition of the etch solution and the material being etched (GaAs vs. AlGaAs, and Al concentration in AlGaAs) may also be relevant. Assuming the wet etch is nearly isotropic and the dry etch is perfectly anisotropic, the wet etch rate can be estimated from the undercut distance, i.e. the gap between the metal traces and the trench walls.

A.4.3 Connecting gates

The final step is to connect the gates to the appropriate annealed bonding pads with metal traces that overlap both features. These connecting features need to be tall enough to climb above the mesa walls, so the depth of the mesa etch should be known before proceeding with this step.

The e-beam-lithography recipe used to pattern the ohmic contacts also works well for this step: the write time is fairly quick, and lift-off is very reliable. The same exact recipe can be followed up to and including the UV-ozone clean, with one important exception: *no sonication during the solvent clean*, since extensive sonication is likely to damage the devices and a pristine surface is not critical for this step anyway. After the UV-ozone clean, the next step is to evaporate 150 nm of Ti or Cr followed by enough Au that the total metal

height is at least 10% greater than the mesa etch depth. Lift-off can then be accomplished as in the ohmic-contact recipe, though here it helps to leave the chip in acetone for a longer period of time.

Potential problems

This step has been quite reliable. On very rare occasions, metal between adjacent bondpads may not lift off all the way, even with a reasonable amount of sonication. In that case, the best strategy seems to be to finish liftoff anyway, then put the chip in the wire-bonder, make some test bonds to other parts of the chip, tuning the power so that when the bonds are pulled off, no metal is left behind. Then bond to the spot where the extra metal is shorting the two bondpads, orienting the bonder so as to cover as much of the extra metal as possible with the bond, and finally pull off the bond. In most cases, the bond and the extra metal underneath it will both come off, un-shorting the contacts.

Appendix B

Dilution refrigerator wiring and other enhancements

As evident in many places throughout this thesis, thermalization of the 2DEG at temperatures on the order of 10 mK is an essential ingredient for these experiments. The experiments described in this thesis were all performed in an Oxford Instruments Kelvinox MX-400 dilution refrigerator ("fridge") with a mixing chamber base temperature of about 7 mK. Many such fridges are commercially available, and all share the same basic principles of operation, developed over a half-century ago. Of course, one is typically interested in using the fridge to cool a sample of interest to a temperature reasonably close to that of the mixing chamber, which is a non-trivial task for reasons to be explained later in this appendix. Since different thermalization techniques are appropriate for different experiments, this task is typically left to the user of the fridge.

For the experiments presented in this thesis, which involve electronic transport measurements of low-impedance devices at low frequencies, low powers and high magnetic fields, relatively few components are required, but they must perform well and reliably.

Specifically, the electrical wires connecting the sample to room temperature need to be heat-sunk and/or filtered at several stages of the cryostat, most critically at the mixing chamber, in order to minimize radiative and conductive heat flows to the device. The sample itself must be held in the center of a magnetic field roughly a foot below the mixing chamber using a low-vibration, radiation-tight "coldfinger" made of materials that facilitate fast thermal equilibration and tolerate fast magnetic field sweeps without heating. This appendix describes the design and fabrication of the heat-sinks, filters, and coldfinger used for the experiments presented in this thesis. Many of the concepts and techniques presented in this section are explained in more detail in texts by Lounasmaa [166] and Pobell [167]. An extremely useful and practical guide to working with cryogenic systems is contained in a free, downloadable booklet published by Oxford Instruments [168].

B.1 Heat-sinking strategies from 300 K to 10 mK

Thermalizing a 2DEG to the mixing chamber is essentially a game of maximizing the thermal conductivity of the links between the 2DEG and the mixing chamber while minimizing the thermal conductivity of the links between the 2DEG and room temperature. While this exercise sounds straightforward in principle, the physics of thermal conductivity renders it difficult in practice: in order to perform transport measurements, the 2DEG typically must be connected to room temperature via many metallic wires, which generally conduct heat somewhat well at low temperatures, while the link to the mixing chamber must be made of insulating materials, which generally conduct heat somewhat to very poorly at low temperatures. With a careful choice of materials based on an understanding of the physics of low-temperature heat transport, this difficulty can be overcome, at least for a system designed for the low-frequency measurements used for these experiments. The high-

magnetic-field environment below the mixing chamber stage introduces some additional considerations, to be discussed in Section B.2.

Treating thermal conductivity, denoted κ, using the framework of diffusive heat transport [167], one finds $\kappa \propto Cv\lambda$, where C is the specific heat of the heat-carrying particles per unit volume, v is their velocity, and λ is their mean free path. In solids, the principal heat-carrying particles are phonons and free electrons. Free electrons travel at speeds close to the Fermi velocity, while phonons travel at the speed of sound; both speeds are nearly temperature-independent at low temperatures, leaving the specific heat and the mean free path to determine the low-temperature scaling of κ versus T. At low temperatures (well below the Debye temperature for phonons and well below the Fermi temperature for electrons), the specific heat of phonons scales as T^3 and the specific heat of electrons scales as T. While these results arise from general thermodynamic considerations, the mean free paths of both electrons and phonons depend on material properties. At low temperatures, scattering of either type of particle from thermal phonons is negligible, and so the mean free path is limited by scattering from crystal imperfections. For electrons in metals and for phonons in reasonably crystalline solids, the mean free path is temperature independent, and can be quite large for both electrons in high-conductivity metals and phonons in nearly perfect crystals. One class of high-conductivity metals breaks the rule, however: in superconductors well below their critical temperature, where most electrons are bound in non-heat-transporting Cooper pairs [8] and the density of free electrons is negligible, heat transport is dominated by phonons, as in an insulator. Another class of materials that requires special treatment is strongly disordered insulators, where the phonon mean free path can be small and temperature-dependent even at the lowest temperatures; such materials can pose difficulties if they have large heat capacities, as discussed in Section B.2.3. Table B.1 summarizes the low-temperature heat-transport properties of various classes of

Material Type	T-scaling	Lower-κ Examples	Higher-κ Examples
Normal Metals	$\kappa \propto C_{\rm el} \propto T$	stainless steel, Cu-Ni	Ag, Cu
Superconductors	$\kappa \propto C_{\rm ph} \propto T^3$	NbTi	Nb
Crystalline insulators	$\kappa \propto C_{\rm ph} \propto T^3$		sapphire
Disordered insulators	$\kappa \propto C_{\rm ph}\lambda_{\rm ph} \propto T^2$	Apiezon N	VGE-7031

Table B.1: Comparison of characteristic thermal conductivity scaling for relevant classes of solids for $T \lesssim 4$ K. In all cases except disordered insulators, the mean free path ($\lambda_{\rm ph}$ or $\lambda_{\rm el}$) is nearly constant in the low-temperature limit.

materials important in cryogenic systems.

B.1.1 Heat-sinking at 4 K

The 24 electrical wires running from room temperature to the mixing chamber are narrow-gauge (0.1 mm diameter) constantan (Cu-Ni) twisted pairs woven into a loom, available from Oxford Instruments. The choice of material and gauge minimizes the heat conduction, while the packaging facilitates handling and minimizes noise pickup from electrical radiation. The loom wires carry a small enough heat load relative to other sources of heat on the helium bath that no special heat-sinking is needed above the fridge's 4 K stage. At 4 K, heat conduction through phonons is still strong enough that simply wrapping the loom wires around copper posts and securing them with thinned VGE-7031[1] (colloquially known as "GE varnish") provides good thermal contact, as well as mechanical stability. Since there is plenty of space at this stage of the MX-400, we use a rather large copper post to ensure complete thermalization, as shown in Figure B.1.

[1]A common preparation is $20 - 40\%$ VGE-7031, depending on desired viscosity, diluted in equal parts toluene and methanol.

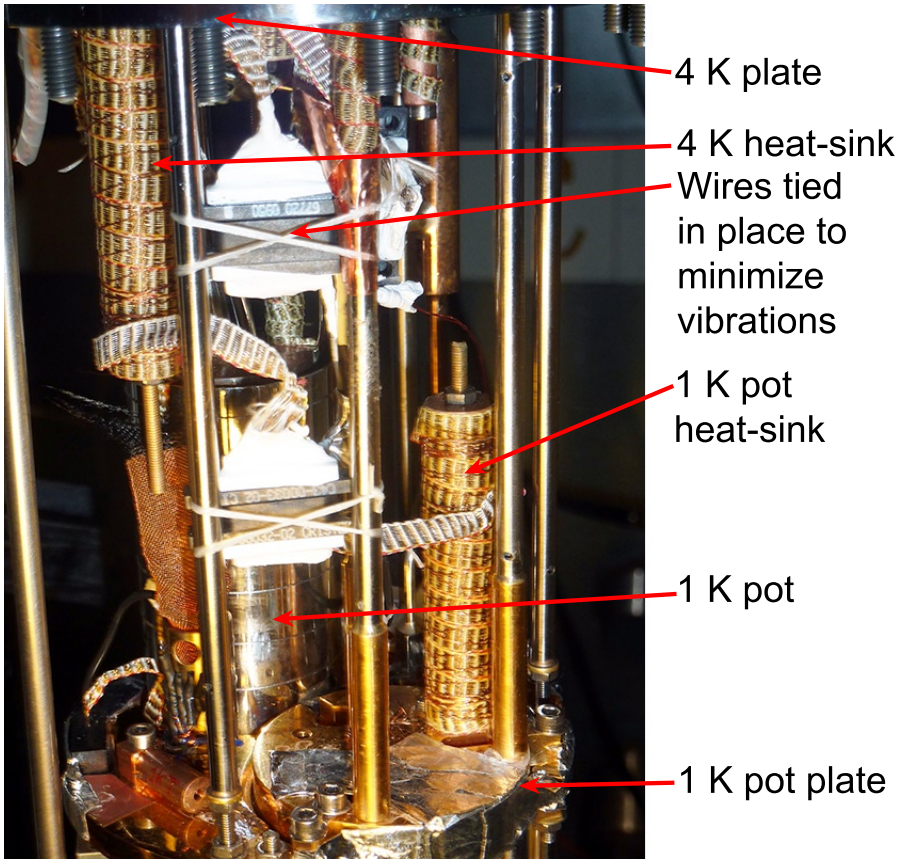

Figure B.1: Heat-sinking at the 4 K and 1.6 K stages. The loom wire is wrapped around a copper post, tied in place with larger-gauge wire and dental floss, and then thermalized to the copper post with GE varnish. Between posts, loom is kept fairly taut and tied down with dental floss to prevent vibrations.

B.1.2 Heat-sinking at 1.6 K (1 K pot)

Heat-sinking at the "1 K pot," which in the MX-400 typically runs between 1.6 and 1.7 K, is also straightforward, and is accomplished using a similar method to that at 4 K. In addition to another copper post, however, we also use a sapphire-based heat-sink box, the details of which are given in Section B.3. This particular heat sink has a relatively high line resistance, on the order of 800 Ω, which accounts for most of the line resistance between room temperature and the sample. In combination with each line's stray capacitance of $\sim$ 500 pF to ground, most of which lies below the 1 K pot, this resistance

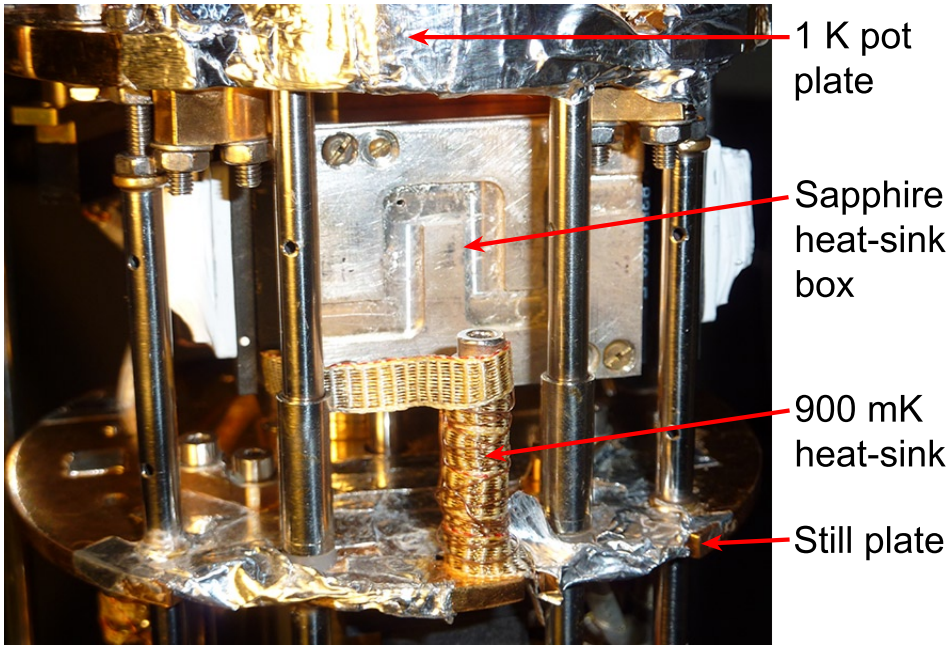

Figure B.2: Heat-sinking at the 1.6 K and 900 mK stages.

creates a low-pass filter that limits the bandwidth of each line to a few MHz in order to prevent unwanted high-frequency noise from heating the sample. It would likely be possible to achieve the same 2DEG temperature even with higher-bandwidth lines, but we have not explored this possibility since the current setup provides more than enough bandwidth for our measurement frequencies of less than 1 kHz.

B.1.3 Heat-sinking at 900 mK (still)

Below the 1 K pot sits the still, which typically runs at temperatures just under 1 K (certainly closer to that temperature than the 1 K pot itself). Since there is limited space at this stage and extensive heat-sinking at the higher stages, here the loom wire is simply wrapped around a copper post like the ones at the higher stages, except smaller because of the limited space.

B.1.4 Filtering at 100 mK (cold plate)

The cold plate of the MX-400 sits between the continuous heat exchanger and the set of five sintered heat exchangers, and runs at a temperature of about 100 mK during normal operation. A copper can known as the radiation shield attaches to this stage and prevents 4 K radiation from reaching the lower stages. Since the wires are also carrying radiation, it seemed natural to filter out most of that radiation at the entry point of the wires into the radiation-shielded volume. Many strategies [169] for filtering exist, but our desire for a "plug-and-play" box that could be easily swapped out, as well as our need to thermalize an entire set of 24 dc wires, suggested the use of a circuit board with discrete surface-mount filters.

Our initial tests showed that except for their bulky size, the VLFX-80 filters from Mini-Circuits were very effective for our purposes. As an alternative, we first pursued the use of Thermocoax (Section B.4). In the meantime, however, Ferdinand Kuemmeth found that each VLFX-80 contains three surface-mount chip filters covering different frequency ranges (models LFCN-80, LFCN-1450, and LFCN-5000), and designed a PC board [Figure B.3(b)] incorporating these components to effectively perform the function of 24 VLFX-80 filters in a fraction of the space. The PC board can be enclosed in a copper box [Figure B.3(a)], allowing easy mounting on the fridge. Not shown in the figure, connection to the loom wire is accomplished using right-angle micro-D connectors with pins soldered into the holes at each end of the board. This approach was found to work as well as both the Thermocoax and the actual VLFX-80 filters, at least in the sense that all approaches led to the same apparent 2DEG temperature.

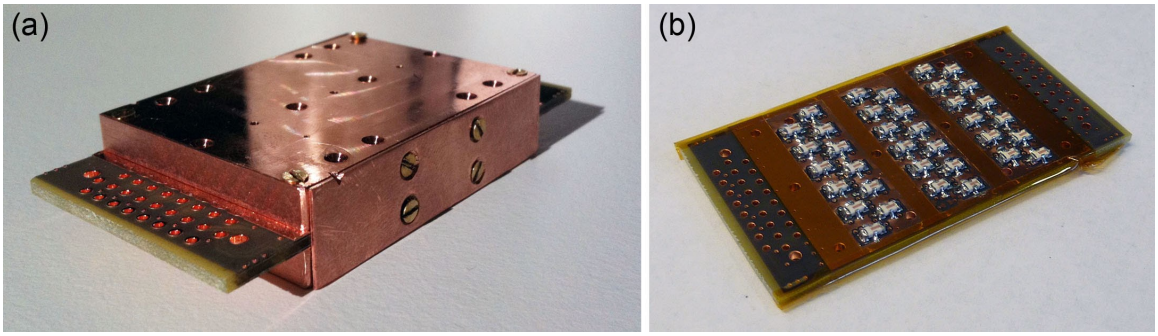

Figure B.3: (a) Copper box enclosing circuit board for RF filtering at 100 mK. Loom wires are connected at each end using right-angle micro-D connectors with pins soldered at each of the holes at the end of the board. (b) Circuit board containing three stages of surface-mount RF filters. The top and bottom of the board each provide 12 lines, yielding 24 total. This board is wrapped in Kapton tape in order to prevent oxidation of the copper ground plane until it is mounted in a copper box.

B.1.5 Heat sinks at 7 mK (mixing chamber)

After all of these stages of heat-sinking and filtering, the total heat flux at the mixing chamber stage from the 24 Cu-Ni wires is likely below 1 nW, much less than the MX-400's cooling power of 10 μW at 10 mK. Despite the large cooling power, the steep temperature scaling of heat transport via phonons means that the thermal conductivity of most insulators drops by at least a factor of $10,000$ between 1 K and 10 mK. Thermal resistances at material interfaces, also known as Kapitza resistances, become significant as well, in some cases requiring large interfacial surface areas or large forces to achieve acceptable thermalization. A notably high boundary resistance, and the first one that needs to be bridged, occurs at the interface between liquid He and most solids. This resistance is typically mitigated by making contact using a layer of sintered silver, which has an extremely large surface area relative to its macroscopic dimensions. The inside of the MX-400 mixing chamber, shown in Fig. B.4, uses several copper fins with sheets of silver sinter soldered onto each side in order to achieve thermal contact between the cold helium mixture and the copper plate onto which the experimental apparatus is mounted.

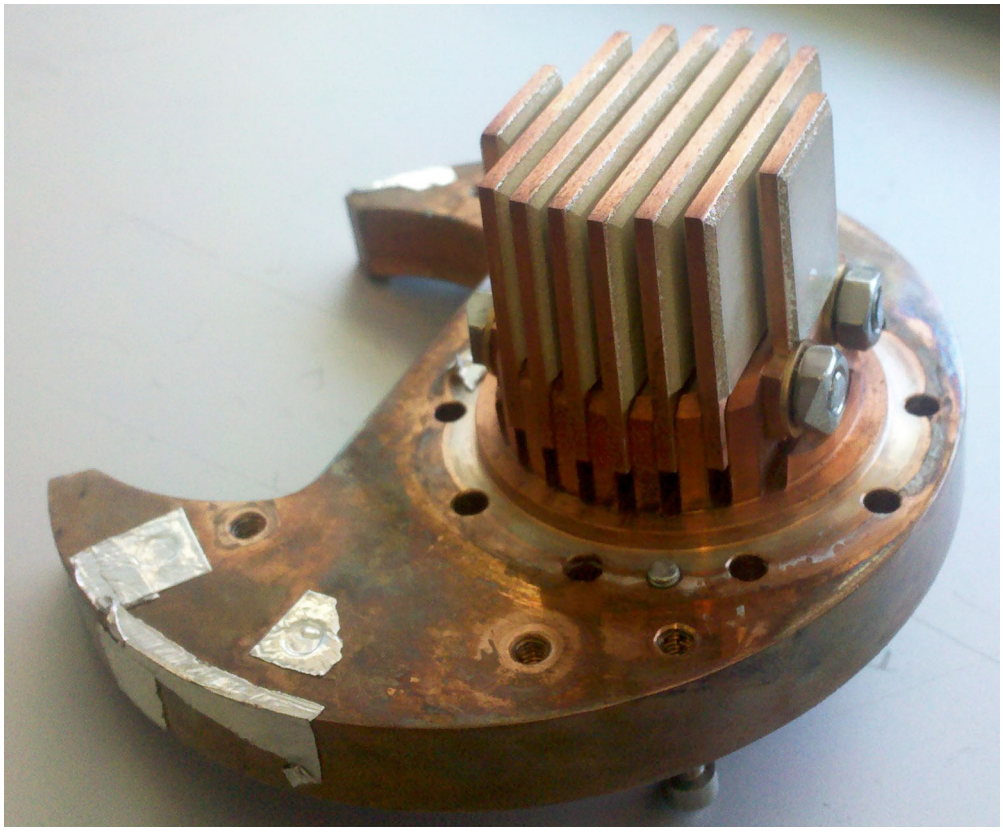

Figure B.4: Heat sinks inside the mixing chamber of the MX-400 fridge, designed and fabricated by Oxford Instruments but included here for educational purposes. The copper plate that forms that bottom of the mixing chamber uses a set of copper fins to enhance thermal contact with the cold helium mixture. A slab of silver sinter on each fin maximizes the surface area of the metal-helium interface in order to reduce the Kapitza resistance. During normal operation, this plate remains attached to the body of the mixing chamber via an indium seal; the failure of that seal led to this photo being taken. The coldfinger mounts on the bottom of the plate.

As apparent from Figure B.4, the mixing chamber makes good thermal contact to a large copper plate; the coldfinger (to be discussed in Section B.2) mounts at the bottom of this plate. While copper is an excellent conductor of heat at low temperatures, surface oxides can increase its thermal boundary resistance. Any visible oxidation is removed by sanding prior to mounting the coldfinger, which is then screwed in tightly at as many points as possible to ensure that this first thermal link is not the weak one. Molybdenum washers,

which have a low coefficient of thermal expansion, cause the connections to tighten as they cool.

Aside from wrapping the loom around another copper post mounted on the mixing chamber plate, which is likely not very effective given the low thermal conductivity of phonons in non-crystalline insulators at mixing chamber temperatures, the main heat-sinking is accomplished inside the radiation-tight environment of the coldfinger itself. We initially used a sapphire-based heat sink at this stage, but switched to a diamond-based one for reasons described in Section B.3. The fabrication of both types of heat sinks is described in Section B.3.1, and their installation on the coldfinger is described in Section B.2.4.

B.2 Coldfinger and sample holder design

In addition to providing good, fast thermalization, the coldfinger used for these experiments must be compatible with high magnetic fields and should minimize vibrations. Magnetic-field sweeps can lead to heating via eddy currents and nuclear magnetization effects [167], both of which typically become significant heat sources at temperatures on the order of 25 mK or less. Equilibration times can also start to become significant below this temperature, generally as a result of "virtual heat leaks" caused by components that take hours or even days to thermally equilibrate, slowly releasing heat over this time. This section explains each of these concerns and then presents the coldfinger and sample holder used for these measurements.

B.2.1 Eddy currents

Eddy currents are a manifestation of Faraday's Law of Induction, according to which a changing magnetic flux Φ induces an emf $\mathcal{E} \propto d\Phi/dt$. The resulting power dissipation along any closed conducting loop in the plane perpendicular to the flux is given

by $\mathcal{E}^2/R$, where R is the resistance of the loop, and it is worth noting that for a uniform magnetic field density, $\mathcal{E}$ is proportional to the area of the loop. These considerations suggest that eddy current heating can be minimized by avoiding large-area closed loops of low-resistance materials in the plane normal to the field direction. In practice, given typical thermal conductivities and values of dB/dt, "large-area" corresponds to a radius of larger than ~ 1 in, and relevant "low-resistance" materials to watch out for include copper and silver, but not brass or stainless steel.

B.2.2 Nuclear magnetization effects

In addition to heating the coldfinger and sample holder via electronic means, magnetic fields can also heat these components via their nuclear spins: starting from equilibrium at a certain magnetic field and temperature, an increase in the magnetic field leads to a larger nuclear Zeeman splitting, resulting in greater alignment of nuclear spins. This configuration has a lower heat capacity, and so the material becomes warmer. Conversely, lowering the magnetic field cools the sample, as heat is transferred from lattice vibrations back into nuclear entropy. Such behavior can be avoided by choosing materials with small or zero nuclear spin, low gyromagnetic ratio, and/or low atomic density (the last two properties are relevant only if the nuclear spin is non-zero). For our coldfinger, we chose silver instead of copper in order to avoid nuclear magnetization issues. Where lower-conductivity metal was needed to prevent eddy-current heating, we used brass, which did not appear to cause significant nuclear magnetization effects in the small amounts used.

B.2.3 Virtual heat leaks

By analogy with a traditional "virtual leak," in which a near-vacuum-tight component slowly releases a volume of trapped helium gas into the vacuum space of the fridge,

a virtual heat leak is said to occur when a component with a high heat capacity and low thermal conductivity slowly releases its heat to the rest of the system. The presence of such components can lead to equilibration times of several hours when attempting to vary the 2DEG temperature in the range of $10 - 100$ mK, and even as long as several days to reach the lowest temperatures after initial cooldown from room temperature.

A common source of virtual heat leaks is the use of certain disordered insulators such as polymers not specially designed for cryogenic applications. It seems best to consider materials in this category as guilty until proven innocent. Indeed, we reduced our equilibration times substantially by replacing a sample holder made of unknown plastic with one made of brass and FR-4, as discussed in Section B.2.5.

In addition to these problematic materials, which are relatively easily identified, well-behaved materials can also act as virtual heat leaks or otherwise misbehave as a result of processing. A common example is the possible incorporation of hydrogen molecules during annealing of copper and other metals commonly used for cryogenic hardware. These molecules have two possible nuclear spin states, ortho- and para-H_2, whose energy difference is on the order of 150 K. When cooled to dilution refrigerator temperatures, eventually all molecules should occupy the lower-energy para-H_2 state, but for a variety of reasons this process can take days, during which the gradually released heat may be significant, particularly at temperatures below 10 mK [167]. A thorough discussion of this and other such time-dependent effects is beyond the scope of this thesis, but the main point is that in general it is important to consider not only the materials to be used, but also what processes they have undergone.[2]

[2]Another noteworthy and surprising effect of processing, though not related to virtual heat leaks, is the magnetization of stainless steel as a result of being cold-worked [170].

B.2.4 Coldfinger details

In addition to meeting the criteria laid out in the previous sections, our coldfinger was designed to allow easy attachment and removal of heat-sinks and other hardware potentially needed for these experiments. The backbone [Figure B.5(a)] is a long, thin silver plate with mounting holes that allow boxes containing any needed heat-sinks and electronic components to be attached from both sides. The top of this plate is vacuum-brazed to a round silver disk that can be fastened to the mixing chamber plate at several points. The bottom is vacuum brazed to a round ring [middle of Figure B.5(c)] with two sets of threads: an inner set for attaching the sample holder, and an outer one for attaching the can that encloses the sample holder. Since this ring and the can that attaches to it both have diameters $\gtrsim 1$ in and sit in a region of strong magnetic field, potential eddy-current heating is mitigated by making several slits in the ring and using a brass can. The top of this ring also has grooves for inserting metal plates that enclose the upper part of the coldfinger on all four sides; to avoid eddy-current heating, two of the four plates are brass, as visible in Figure B.5 (the front silver plate has been removed in order to show the inside of the coldfinger). The four seams are sealed using aluminum tape. Since the geometry of this structure resembles a diving board, vibrations in certain frequency ranges could cause it to resonate. To avoid that possibility, it is stabilized by L-shaped brackets that screw into both the mixing chamber plate and the edges of the backbone. Although the use of brass components could in principle lead to nuclear magnetization effects, we find that any such effects are negligible at typical magnetic field sweep rates.

As mentioned above, circuit boxes can be mounted on either side of the backbone of the coldfinger. For these experiments, only one circuit box is needed, and so the space on the other side of the backbone is empty except for a ruthenium oxide resistor (discussed in Section B.5.1) attached to the backbone with silver paint, and a fiber-optic cable used

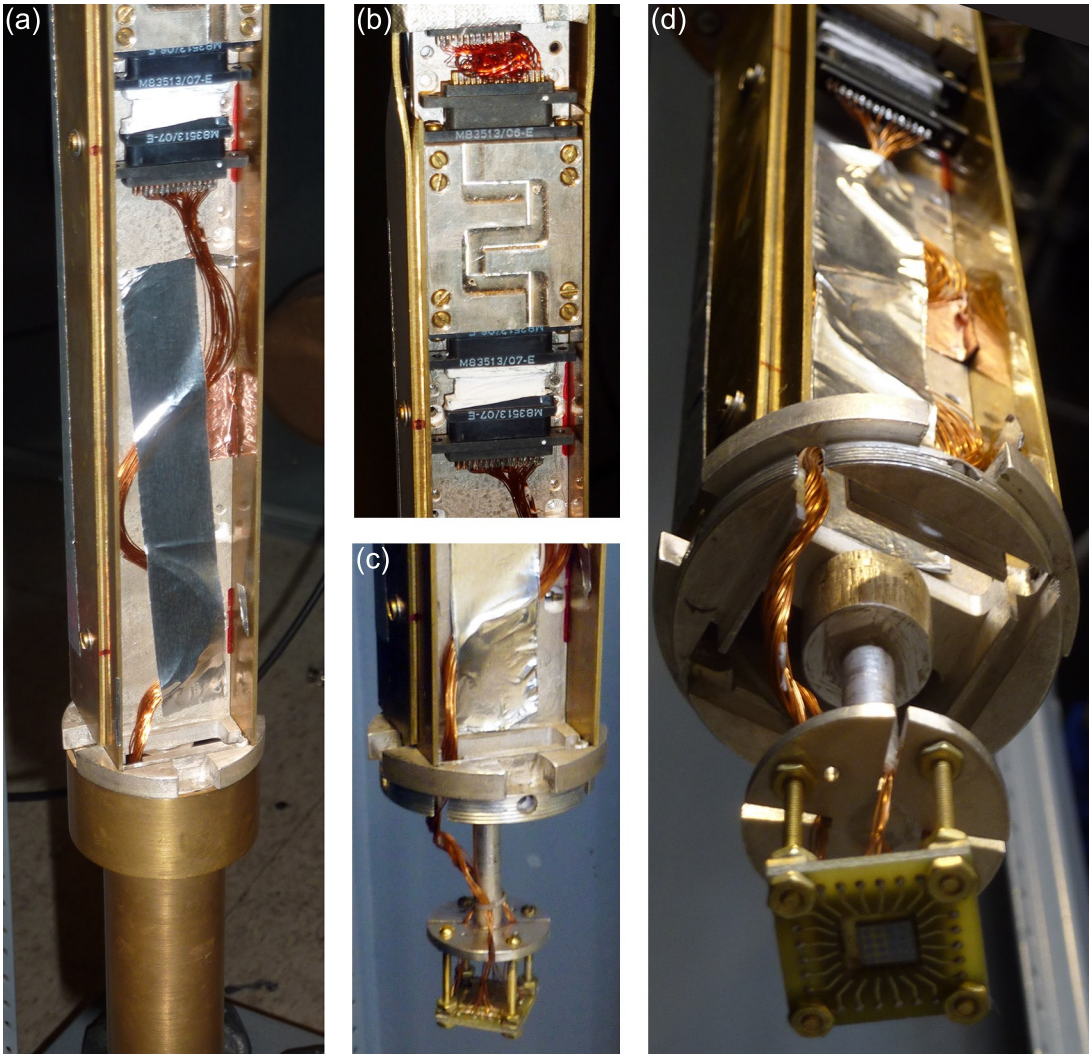

Figure B.5: Several views of the coldfinger used for these experiments. (a) Section from the heat-sink box to the bottom, showing the connection from the heat-sink box to the sample-holder wires, and the taping of the wires to the backbone to prevent vibrations. During normal operation, a silver plate seals off the region containing the wires. (b) Detail view of the heat-sink box. The meandering groove on the box cover facilitates pump-down of the lower region, which would otherwise be nominally sealed when the silver plate is attached. (c) Detail view of the sample-holder region. The braiding and taping of the wires reduces the effect of vibrations. (d) View from below the sample holder, showing a mounted sample and the path of the wires all the way up to the heat-sink box.

occasionally to illuminate the sample (discussed in Section B.6). To block radiation, a silver plate covers this side as well, and the opening at the top is covered with metal tape.

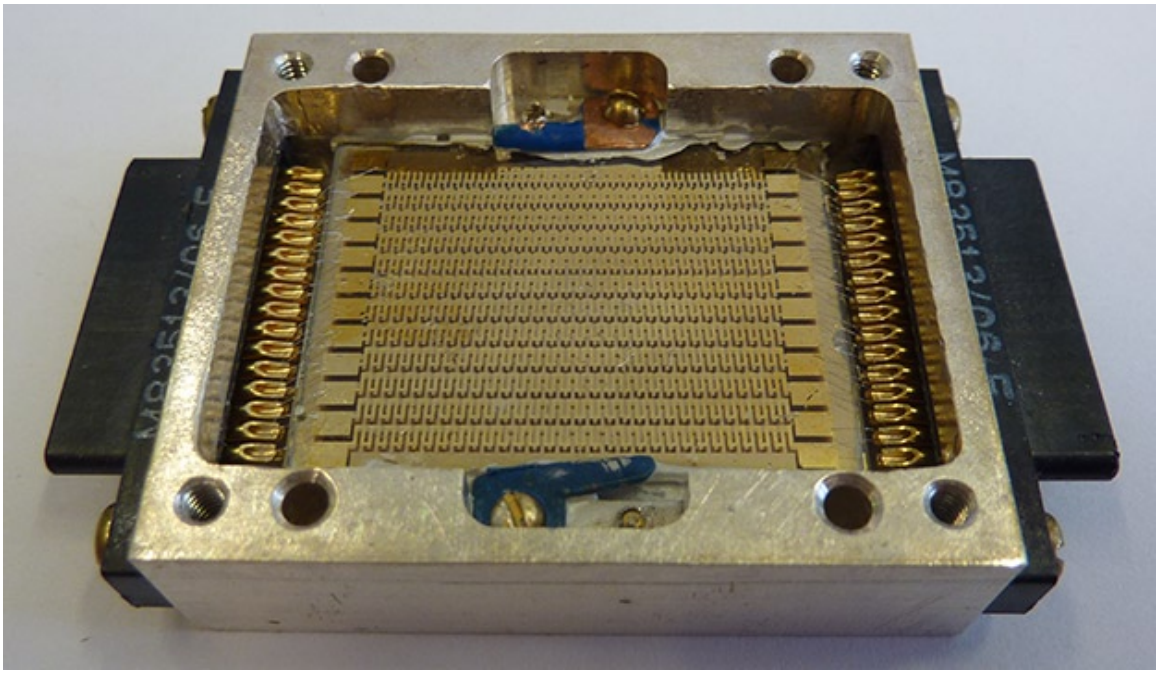

Figure B.6: Close-up view of silver circuit box containing sapphire heat sink. Another sapphire heat sink is mounted identically on the other side of the center plane of the box.

Circuit boxes

Circuit boxes that mount on the coldfinger [Figure B.5(b)] are also silver, and maximize the density of components by including a center plane onto which components can be mounted from both sides. Boxes for both dc and high-frequency circuits were developed, but the only boxes used for these experiments were those housing heat sinks for dc wires. The original sapphire heat sinks (Figure B.6) were mounted on each side of the center plane using silver paint or silver epoxy, while the diamond-on-molybdenum heat sinks that replaced them mount by screwing the two heat sinks together through two holes in the center plane. In either case, connection to the loom wire is made using plastic micro-D connectors with solder cups. Given the high density of connections to be made from these connectors to the heat sinks, wire-bonding is used rather than soldering. Wire-bonding to the solder cups is straightforward with practice, particularly on cups with flat "ledges" on

the two sides. Wire-bonding to sapphire heat sinks is also straightforward. The wire-bonds to diamond heat sinks tend to be quite weak, and often require a small dab of silver paint ("High Purity Silver Paint," type 05001-AB, from SPI Supplies), placed using a 25 gauge needle or a whittled-down toothpick, to hold them in place.

Once the circuit is assembled, a plain cover is attached to the side of the box that will contact the backbone of the coldfinger, and a cover with a meandering groove and two vent holes is attached to the other side, allowing easy pump-down of the interior of the box and the space below it. The flat cover is finely sanded (600 grit or finer) to remove any surface contaminants that might impede thermal contact with the coldfinger; to maintain flatness of the surface, the sandpaper is placed face-up on a flat table, and the box is moved around it in circles using gentle pressure. The box is then attached to the coldfinger using brass screws, with molybdenum washers to help the connections tighten rather than loosen as they cool.

B.2.5 Sample holder details

The sample holder initially used for these experiments was a plastic block with embedded metal pins onto which a ceramic chip carrier was mounted. Although 2DEG temperatures $\lesssim 10$ mK were achieved with this sample holder, thermal equilibration times were long, with the last 5 mK or so taking days after the initial cooldown from room temperature. This problem was overcome by designing a new sample holder using materials with known thermal properties. In the new sample holder, visible in Figure B.5(c,d), the sample sits on a brass plate and is surrounded by an FR-4 circuit board with copper traces. The copper traces allow wire-bonding to the sample, and at the outer end have holes through which wires are soldered. The wires are 0.012"-diameter, 99.99% copper wire from the California Fine Wire Company. All 24 wires coming from the sample holder are

terminated on a plastic micro-D connector that connects to the heat-sink box mounted on the coldfinger. The sample holder is supported by four brass screws attached to a silver spindle. The silver disc to which the screws attach serves as a final radiation shield, as its diameter nearly matches the inner diameter of the brass can around it; the slits cut in the disc serve to prevent eddy-current heating and provide a path for the wires. To change samples, the silver spindle is unscrewed from the rest of the coldfinger.

B.3 Meander-line heat sinks

Even at 10 mK, the large mean free path of phonons in crystalline insulators such as quartz, sapphire, and diamond makes them much better thermal conductors than amorphous insulators such as polyimide, GE varnish, or FR-4. Our initial heat sink used a 500 μm thick sapphire substrate with photolithography-defined meander lines on the top and a ground plane on the bottom, both made from evaporated Cr/Au (30/300 nm). This sapphire plate was attached to the center plane of a circuit box (see Section B.2.4) using silver paint or silver epoxy, which provided good thermalization (yielding a 2DEG temperature $\lesssim 10$ mK) for approximately three cooldowns, after which it yielded a 2DEG temperature of approximately $15 - 20$ mK. We discovered that differential contraction of the sapphire plate and the silver box caused the silver paint to crack after a few thermal cycles, preventing the sapphire plate from being well thermalized to the silver box after that point. The use of a clamp to push the sapphire plate against the silver box did not seem to help. To solve this problem, we switched from sapphire substrates to diamond films grown on molybdenum substrates, which can be screwed into the silver boxes with plenty of force to ensure good thermal contact.

One of my most surprising discoveries of the last six years concerns the choice of

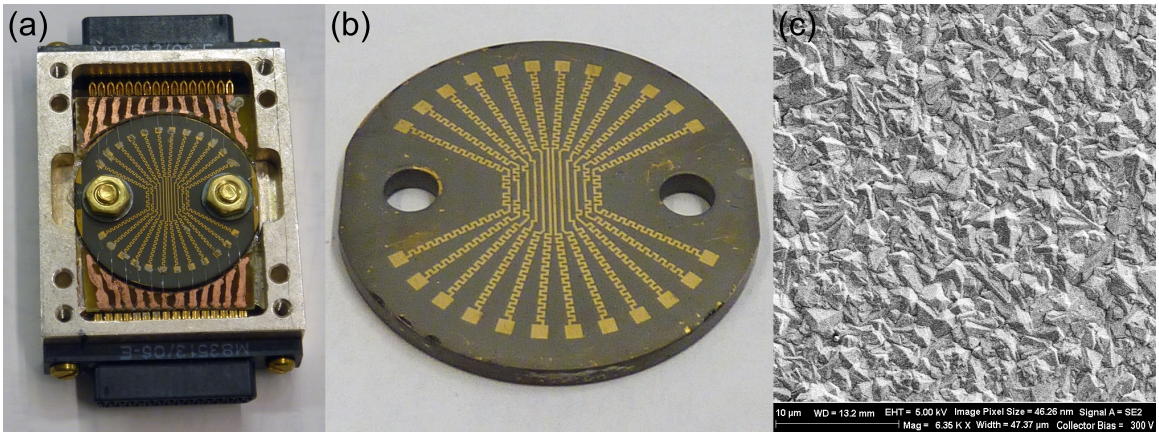

Figure B.7: Diamond heat sinks at various levels of magnification. (a) Heat sink mounted in a silver box. The two small copper/FR-4 PC boards at top and bottom facilitate wire-bonding from the connectors to the heat sink. A similar heat sink is mounted on the underside of the center plane of the box, and brass screws hold the two heat sinks firmly against the center plane. (b) Close-up of diamond heat sink. The diamond film is quite robust, but can flake off near the edges if not held carefully, as seen in the lower left. (c) SEM micrograph of the diamond surface.

sticking-layer metal for the heat sinks. For a long time, we were regularly able to achieve a 2DEG temperature of about 20 mK, but only sometimes reached 10 mK. It eventually became apparent that the first sapphire heat sink we[3] ever made somehow worked better than subsequent ones, a fact that remained a mystery until we made the first generation of diamond heat sinks and found that they also cooled the 2DEG to nearly the exact same temperature ($20 - 25$ mK) as all of our sapphire heat sinks except the first. At this point it became impossible to overlook the one obvious, yet seemingly negligible, difference between the first sapphire heat sink and all subsequent heat sinks: the first one used a chromium sticking layer, and all subsequent ones used titanium. Sure enough, after making a new set of diamond heat sinks with a Cr sticking layer, we consistently obtained electron temperatures of ~ 10 mK or less.

[3]Actually, Vivek Venkatachalam made this one.

B.3.1 Detailed recipes

Obtaining sapphire substrates

Suitable sapphire substrates are relatively easy to come by, since there are few specific requirements. We used rectangular plates roughly 23 mm wide, 31 mm long, and 0.5 mm thick. Since the thermal conductivity is not significantly anisotropic, any crystal orientation is fine. We originally used double-side-polished pieces, but the more readily available single-side-polished seem to work comparably, at least when the polished side is used for the ground plane and the non-polished (fine-lapped) side is used for the meander lines. Depending on the availability of different sizes, it may be tempting to cut a sapphire plate into smaller pieces. We did so several times using a Disco DAD-321 Dicing Saw, but caution that this process can be slow and arduous.

Growing diamond substrates

Diamond films can be grown using a plasma-enhanced chemical vapor deposition (PECVD) process, as implemented in the Seki Technotron AX5010-INT at Harvard CNS. The high temperature needed for this process limits the choice of substrates. Molybdenum appears to be an excellent choice for our purposes: in addition to withstanding the high-temperature PECVD process, it can be obtained and machined fairly easily, and its low coefficient of thermal expansion ensures a tight fit, and hence good thermal contact, at low temperatures.

Before diamond deposition, the molybdenum substrate needs to be prepared. We begin by polishing the face onto which the diamond film will be grown to a mirror-like shine, and polishing the reverse side, which needs to make good contact with the center-plane of the heat-sink box, to a nice matte finish. It is unclear whether the mirror finish for the

diamond-film side is necessary, but its purpose is to reduce the likelihood of any exposed metal remaining after the film is grown in order to prevent shorts between the meander lines and the molybdenum. Next, the substrate is cleaned by sonication in TCE, acetone, and methanol for 5 min each. The growth is then seeded by impregnating the substrate with diamond crystals via sonication for 15 min in a mixture of one part methanol to three parts diamond-seeding slurry. The slurry is 0.5% w/v detonation nano-diamond in DMSO. After seeding, the substrate is rinsed briefly in methanol (no sonication at this step) and blown dry with nitrogen gas.

The PECVD process uses an RF power source to ignite a plasma from a 40 Torr mixture of H_2 and CH_4 flowing at rates of 300 and 3 SCCM, respectively. The optimal growth temperature is a little above 1000° C. Carbon is deposited onto the seeded nano-diamond crystals, leading to a vertical growth rate of approximately 0.5 μm per hour. Films of about 5 μm or thicker are generally robust against shorts; occasional room-temperature resistances of several MΩ to ground are observed, but usually freeze out at low temperatures. When the desired thickness is reached, the substrate should be cooled gradually: on the order of 10 min to reach 500° C, and then at least another 20 min after turning off the RF power before venting the chamber. Faster cooldowns have caused the diamond film to crack and flake off. After removal from the chamber, the substrate is baked on a hotplate at 350° C for 30 min in order to evolve the hydrogen gas trapped in the diamond film, which would otherwise lead to shorts between the diamond surface and the molybdenum. If the bake is not performed right away, shorts will develop over the course of a few hours, but performing the bake even after then will reverse any shorts that have developed.

Meander line fabrication process

We fabricate meander lines using a standard photolithography technique in which the metal layer is pre-evaporated, and the patterned photoresist serves as an etch mask. This etching procedure is preferable to a lift-off procedure since the metals used are easily etched, and lift-off with photolithography can be difficult since the walls of the resist do not naturally give the desired undercut.

The following procedure is used for both sapphire and diamond-based heat sinks, with only minor differences as noted.

1. Clean the substrate in acetone and then isopropanol for 3 min each, then blow dry with the side on which meander lines are to be fabricated facing up.

2. Evaporate 30 nm Cr followed by 300 nm Au on the meander-line side. *Do not substitute Ti for Cr!*

3. Repeat step 1.

4. Bake at 180° C for 5 min.

5. Set spinner recipe for 45 s at 5000 rpm, with ramp speed 5000 rpm/min. Position substrate on spinner, using as a large a chuck as possible in order to maximize suction. The diamond-on-molybdenum substrates in particular have a tendency to fly off if not mounted optimally. Spin the substrate before applying resist to allow it to cool and test the suction.

6. Apply enough S1813 photoresist to cover most of the substrate, being careful to avoid creating bubbles. Any bubbles that do appear can be removed by dragging them to the edge and popping them.

7. Spin again.

8. Bake for 2 min at 115° C.

9. Align and expose for 4 s on the AB-M mask aligner.

10. Develop for 20 s in one beaker of CD-26, 25 s in a second beaker of CD-26, then rinse for 20 s in a beaker of DI water, and finally blow dry. Continuously move the substrate back and forth throughout the two developing steps.

11. UV-Ozone clean for 45 s.

12. Etch the gold layer using an iodine-based gold etchant such as Transene Type TFA. The gold should be thoroughly gone after a minute or two. Transfer to DI water and rinse for 15 s. Then transfer directly to a chromium etchant such as Transene Type 1020. During both transfers, keep a layer of liquid on the surface to prevent the chromium from oxidizing. If the chromium has not oxidized, the Transene Type 1020 should remove it within a minute.

13. If the chromium appears to resist the Transene Type 1020, it has likely oxidized. In this case, rinse in DI water and then transfer to HCl ($\sim$ 30%, undiluted) at 50° C. Take a 6-inch-long piece of aluminum foil and dip the end into the HCl for a few seconds. Soon after being removed, the dipped part of the aluminum foil should hiss and turn black, and the chromium oxide on the substrate should dissolve. Amazing!

14. Rinse the substrate in a fresh beaker of DI water for 30 s and blow dry.

15. Remove the photoresist by soaking in acetone for about 10 min, or less if heat is applied. Do not sonicate, as it may damage the metal traces. Then rinse in isopropanol and blow dry.

16. Anneal the substrate. A typical GaAs ohmic-contact anneal recipe works well for this purpose: anything close to 460° C for about 75 s should be fine.

17. If you somehow forgot to remove the resist before annealing, the traces will look dark brown and seem to be completely ruined. Fortunately, experience has shown that a minute or two in a piranha bath (roughly a 3:1 mixture of H_2SO_4:H_2O_2) will remove the hard-baked resist and restore the gold appearance of the traces.

B.4 Thermocoax

An alternative method of filtering and heat-sinking is the use of thin coaxial cables with a lossy metal-oxide-powder dielectric such as those made by a company named Thermocoax. The skin effect causes radiation traveling down the center conductor of each line to be absorbed by the dielectric and dissipated continuously along the length of the cable, with no need for any additional filtering or heat-sinking of the inner conductor between room temperature and the mixing chamber. We tested this approach using 7 ft of cable for each line, heat-sinking the outer conductors at each temperature stage using a bracket filled with silver epoxy, and using a meander-line heat sink to thermalize the inner conductors at the coldfinger. The 2DEG temperatures achieved using this approach were comparable to those achieved with the discrete-filter approach, but there were advantages and disadvantages in other performance aspects. The main advantage was that the shielding from the outer conductors prevented stray electromagnetic radiation from interfering with the lock-in measurements. On the other hand, the relatively high 1 nF capacitance of each line and the room-temperature partial shorts between the center and outer conductors on some lines proved troublesome enough that we ended up sticking with the discrete-filter approach.

B.5 Low-Temperature Thermometry Techniques

Finally, it is worth briefly addressing the question of how the fridge and 2DEG temperatures can be measured. One would ideally like to have a primary thermometer, namely one whose output can be converted into a temperature using only known physical constants, but measuring such thermometers tends to be time-consuming and/or require specialized equipment. As a result, the more common method is secondary thermometry, in which the temperature is determined from a system whose temperature dependence is not known *a priori* but has been determined from measurements in a system with a known temperature and parameterized using a fit function. Although typically simpler to measure, secondary thermometers have the disadvantage that their temperature dependence may drift over time, especially after repeated thermal shocks and other stresses. In this section, we describe some primary and secondary thermometers used for determining the temperature of the mixing chamber and the 2DEG.

B.5.1 Mixing chamber thermometry

At dilution refrigerator temperatures, a commonly used technique for primary thermometry is the nuclear orientation technique, in which the temperature is determined from the measured anisotropy of gamma ray emissions from a radioactive sample such as ^{60}Co. One advantage of this technique is that since the gamma rays penetrate the cryostat walls, they can be detected externally without the need for any wires running from room temperature to the mixing chamber; as a result, the performance of the mixing chamber can be measured with minimal heat load.

Since keeping a radioactive sample mounted at the mixing chamber and measuring it during every cooldown would be inconvenient, secondary thermometry is typically used once the fridge's base temperature has been confirmed. The most commonly used

secondary thermometer for temperatures below about 100 mK is a ruthenium oxide resistor. In addition to the two that came with the dilution refrigerator, we purchased a few of the model RX-102A-AA resistors from Lakeshore Cryotronics in order to test coldfinger thermalization times and to have backups since the exact temperature dependence can drift after many thermal cycles. These resistors are sold both uncalibrated (expensive) and calibrated (really, really expensive), so since we had one resistor with known calibration, we purchased uncalibrated ones and calibrated them ourselves by measuring their resistance at several known temperatures and fitting a special function to the data. The fit coefficients are used to convert resistance to temperature on subsequent cooldowns.

It is worth noting that both the pre-installed ruthenium oxide resistors and the ones we added were connected to a secondary loom for diagnostic wiring, which does not undergo the same extensive heat-sinking and filtering as the measurement loom; instead, simple copper posts are used at each stage. Since the reported temperatures are quite reproducibly on the order of 10 mK, evidently the resistors themselves are well thermalized: the pre-installed resistors have an outer shield that is screwed into the mixing chamber plate, and the ones we installed have a smaller shield that we attach to the target component using silver paint. On some cooldowns, and especially at high magnetic fields, we do notice occasional heating of the resistors (but not the 2DEG), likely resulting from the lack of robust heat-sinking of the wires connecting to them.

B.5.2 2DEG thermometry

As discussed throughout this appendix, the 2DEG can be at a substantially higher temperature than the mixing chamber, and so a direct measurement of its temperature is useful. Methods of primary thermometry include Coulomb blockade peak widths in the temperature-broadened regime [171] and shot-noise thermometry [172]. As with other

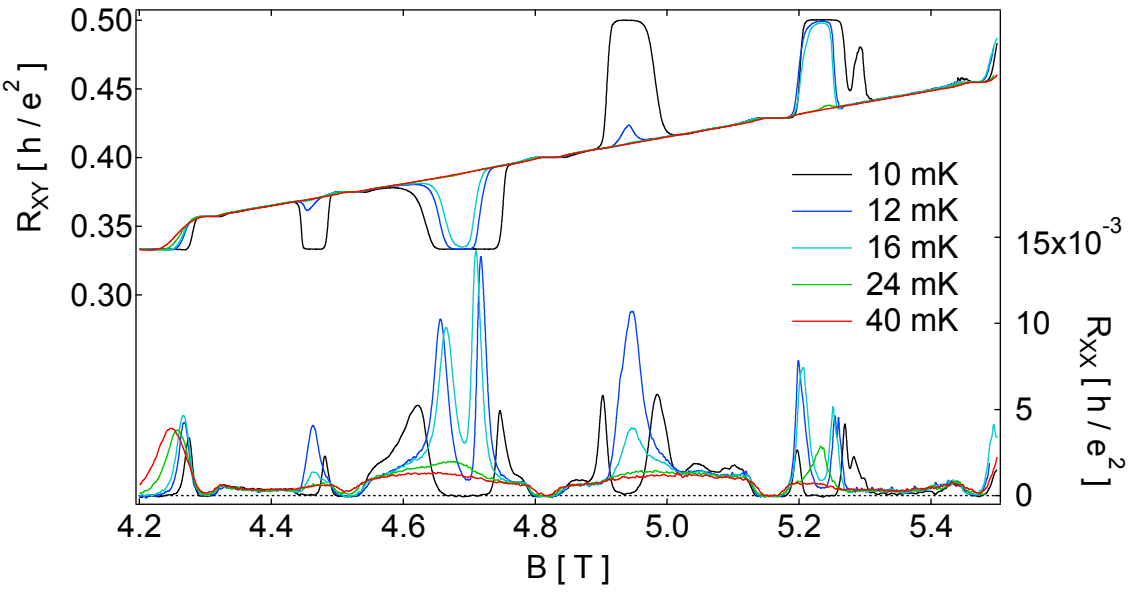

Figure B.8: The re-entrant IQH features in the second Landau level are extremely sensitive to temperature below about 25 mK, making them particularly useful for relative thermometry in this temperature range. The 10 mK trace is not quite the coldest that we can achieve, but is shown here to highlight the interesting competition at this temperature between the re-entrant IQH state near $B = 5.2$ T and an FQH state.

primary thermometers, each of these has drawbacks making them undesirable for regular use: the former requires a quantum dot that needs to be carefully tuned on each cooldown, while the latter requires a quantum point contact and coaxial cables for MHz-frequency measurements.

As a result, the 2DEG temperature is typically estimated through indirect methods, many of which cannot even properly be called secondary thermometers. The IQHE and FQHE show significant temperature dependence from 4 K all the way down to the lowest measurable temperatures, and so the simplest way to estimate the 2DEG temperature is simply to measure a wafer with known temperature dependence and observe which features appear. For a wafer whose behavior has not already been measured in a fridge where the 2DEG temperature is known to match the mixing chamber temperature, saturation

of Shubnikov-de Haas oscillation amplitudes [173] or of FQH-state R_{xx} minima [174] are additional ways to estimate the 2DEG temperature. At the lowest temperatures, the FQH states and especially re-entrant IQH states in the second Landau level become extremely sensitive to temperature, as shown in Figure B.8, making them especially useful for quickly estimating relative temperature between different cooldowns of the same wafer.

B.6 LED illumination

A way to increase the density and mobility of a given 2DEG, particularly in GaAs/AlGaAs wafers where the Si donors are placed directly in the AlGaAs layer, is to illuminate it with a red LED for some length of time during the cooldown. Doing so excites electrons out of tightly bound states associated with DX centers [175], not only increasing the density of electrons in the 2DEG but also delocalizing electrons in the donor layer, leading to more effective screening. In our experience, while illumination enhances the quality of the FQH features, it also significantly reduces the stability of gated devices: specifically, trench-gated devices remain just stable enough to observe oscillations with clear magnetic-field and gate-voltage periods, but surface-gated devices become too unstable to measure any periods. All of the main experiments presented in this thesis were performed without illumination, but the details of our illumination procedure are included here for completeness.

The LED is a standard red LED that lights at room temperature with a current of a few milliamps and a voltage drop of a few volts. Unlike some other nominally equivalent LED's, it was found to remain lit while dunked in liquid nitrogen before mounting in the fridge. It is tied to a stainless steel tube just below the 4 K plate at the top of the fridge, but no special steps are taken to thermalize it since it needs to heat above 4 K in order to

operate well (i.e. at reasonably low voltages). It is powered using constantan wires from the same loom that the ruthenium oxide sensors connect to. A fiber-optic cable is inserted into a small hole drilled in the tip of the LED housing and held in place with optically transparent epoxy. The cable runs from the LED down the fridge and into the side of the coldfinger not being used for circuit boxes. At the very bottom, the cable is bent in a "J" shape so that it points back up toward the sample. The end of the fiber-optic is capped with a large blob of optically transparent epoxy to slightly diffuse the light coming out the end.

During the cooldown, the LED is typically activated when the mixing chamber temperature is estimated to be between 5 and 20 K, and left on for $10 - 15$ min. The LED is activated using a current bias of 3 mA from a Keithley 2400 SourceMeter. A large voltage, many tens of volts, is usually required to turn on the LED, but the needed voltage quickly falls to less than 20 V as a result of heating. This procedure seems quite reliable in that its effect on the density and FQH features is reproducible for different cooldowns of the same wafer.

Appendix C

Data acquisition hardware and software

The data acquisition system built for these experiments can be divided into hardware and software components, and components in each category can be classified according to whether their function is to control the independent variables (primarily magnetic field, gate voltages, and applied currents) or to measure the dependent variables (primarily Hall, longitudinal, and diagonal resistances). This appendix presents the hardware and software used for control and measurement in these experiments.

C.1 Hardware

The measurement hardware consists of commercial pre-amplifiers and digitizers chosen to allow low-noise, low-frequency measurements of low-impedance (usually $\lesssim 25$ kΩ) devices. In a conventional setup, each pre-amplifier would be followed by a lock-in amplifier such as the much-revered but antiquated Princeton Applied Research 124[1] or the more

[1]This model has its own built-in pre-amplifier, the PAR 116, which has excellent noise properties.

modern Stanford Research 830. Such a setup works well when one or two signals are being measured, but becomes unwieldy beyond that as multiple lock-in amplifiers must be stacked up and wired appropriately with power and signal connections. Obviously such a setup includes a great deal of redundancy, especially if only one excitation is being used for all of the measurements. In the experiments presented in this thesis, up to four signals are measured at once (e.g. Hall and longitudinal resistances on two different mesas), with up to three of them sharing the same excitation (e.g. Hall, longitudinal, and diagonal resistances on a single mesa). To facilitate such measurements, the pre-amplifier outputs are digitized, and the resulting data streams continuously fed to a dedicated computer that performs the functions of a lock-in amplifier (several integrated lock-in amplifiers, actually) using digital signal processing techniques. Further discussion of the digital lock-in software will be saved for Section C.2.1.

The remainder of this section presents details of the measurement hardware, control hardware, and physical layout of the system.

C.1.1 Pre-amplifiers

The oscillations in resistance that constitute the signature of electronic Fabry-Perot interference are in some cases quite small ($0.001\ h/e^2 \approx 25\ \Omega$), and often must be measured with small currents (less than 1 nA) to avoid energy averaging (see Chapter 3) and DNP effects (see Chapter 4). To achieve a signal-to-noise ratio (SNR) of 10 or better when measuring a 25 Ω signal with 0.5 nA, a noise level of 1.25 nV or less is required.

The best commercially available low-noise voltage pre-amplifiers allow such precision to be achieved with reasonable ($\lesssim 1$ s) averaging times. For these experiments, we used model LI-75A pre-amplifiers made by the Japan-based NF Corporation, which have an input-referred noise floor of about 1.3 $\mathrm{nV}/\sqrt{\mathrm{Hz}}$ and a voltage gain of 100. Although other

pre-amplifiers such as Signal Recovery's model 5184 offer lower noise floors, the LI-75A is a true differential amplifier, making it less sensitive to common-mode noise than pseudo-differential amplifiers like the 5184. Another advantage of the LI-75A is its use of a separate power supply box, the PS-70A, that can be installed several feet away in order to reduce the potential for 60 Hz noise issues. The main disadvantage of the LI-75A pre-amplifiers is that some units suffer from significant $1/f$ noise, necessitating the use of frequencies above 100 Hz to obtain the best noise performance, but this is not a significant limitation for these measurements.

C.1.2 Digitizers

The two digitizers used for this system are both National Instruments model PXI-4462, mounted in adjacent slots in a National Instruments PXI-1000B chassis. The PXI chassis, depicted in Figure C.1, connects to a computer and essentially acts as an extension of its PCI bus, allowing modules to be easily inserted and removed without taking apart the computer.

Each PXI-4462 has four simultaneously sampled channels. The maximum sampling rate of $204,800$ samples per second is more than two orders of magnitude above the rate needed to measure our signals, which are well under 1 kHz. The most important feature is the high sensitivity: each channel has 24-bit resolution, in principle allowing voltage sensitivity down to 37.7 nV when the minimum input range of ± 316 mV is selected. In practice, noise becomes the limiting factor in this range, even with the digitizer inputs grounded. The typical noise level of $\lesssim 10$ nV$/\sqrt{\text{Hz}}$ measured in that configuration is an order of magnitude smaller than the noise from the preamplifiers, and therefore insignificant. Cross-talk between channels is also negligible. On a typical cooldown in which devices on two mesas are being measured simultaneously, each digitizer is dedicated to one mesa,

Figure C.1: National Instruments PXI chassis including digitizers, signal generators, and other instruments. The two PXI-4462 digitizer cards accept signals via direct BNC connection, while the PXI-6259 card, used for generating the lock-in reference signals, connects via the external breakout boxes sitting above the PXI chassis.

sampling the associated lock-in reference signal and up to three measurement signals. In principle, however, the two cards could be synchronized to allow signals measured on one card to be compared against a reference measured on the other.

C.1.3 Control hardware

The lock-in reference excitations are generated by a National Instruments model PXI-6259 card on the same chassis as the digitizer cards. The two ac voltages generated by this card, typically in the range of $100 - 300$ Hz and $0.1 - 0.5$ V_{rms}, are converted to currents using resistors on the order of 1 GΩ at the top of the fridge.

Gate voltages are applied using a DecaDAC board and a BabyDAC board, both designed and built by Jim MacArthur of Harvard's Electronic Instrument Design Lab. Both boards have high voltage resolution and are controlled from the main acquisition

computer using commands sent over a fiber-optic connection. Their outputs are connected to the fridge using BNC cables designed to minimize triboelectric noise, specifically Pomona Electronics series 4964-SS. At the top of the fridge, each gate-voltage signal is passed through a 2.5x voltage divider in order to increase resolution[2], and low-pass filtered using a single-pole RC filter with $f_{3\mathrm{dB}} \sim 1$ kHz.

The magnet is a superconducting solenoid with a maximum field of 10 T when operated at 4 K, or 12 T when the so-called "Lambda fridge" is used to cool the portion of the helium bath containing the magnet to about 2 K. The magnet can be run in persistent mode, which significantly reduces helium consumption if the magnet needs to be held at a constant high field for a significant time. The magnetic field is proportional to the current run through the solenoid, which is supplied by two sources: the IPS-120-10 provided by Oxford Instruments can provide enough current to reach the highest fields, but is limited to a minimum step size of 0.1 mT and a minimum ramp rate of 1 mT/min; connected in parallel, a Kepco BOP-20-20 can access a much smaller range of field but allows much smaller steps and sweep rates. The IPS-120-10 is controlled directly from the main acquisition computer over a serial cable, while the Kepco is controlled via a voltage from the BabyDAC board.

C.1.4 Overall layout

In order to minimize noise induced by electromagnetic radiation, the shielded room is usually maintained as a "dc-only" zone, containing no electronic equipment besides the DAC's and the pre-amplifiers, all of which receive dc power from sources located outside the shielded room. The power cables for these instruments, as well as all signal-carrying cables, run through a long, narrow tube penetrating the shielded room wall. Near the outside end

[2]The ultra-high resolution thus achieved has not been necessary for these experiments, but the range has not been a limiting factor either.

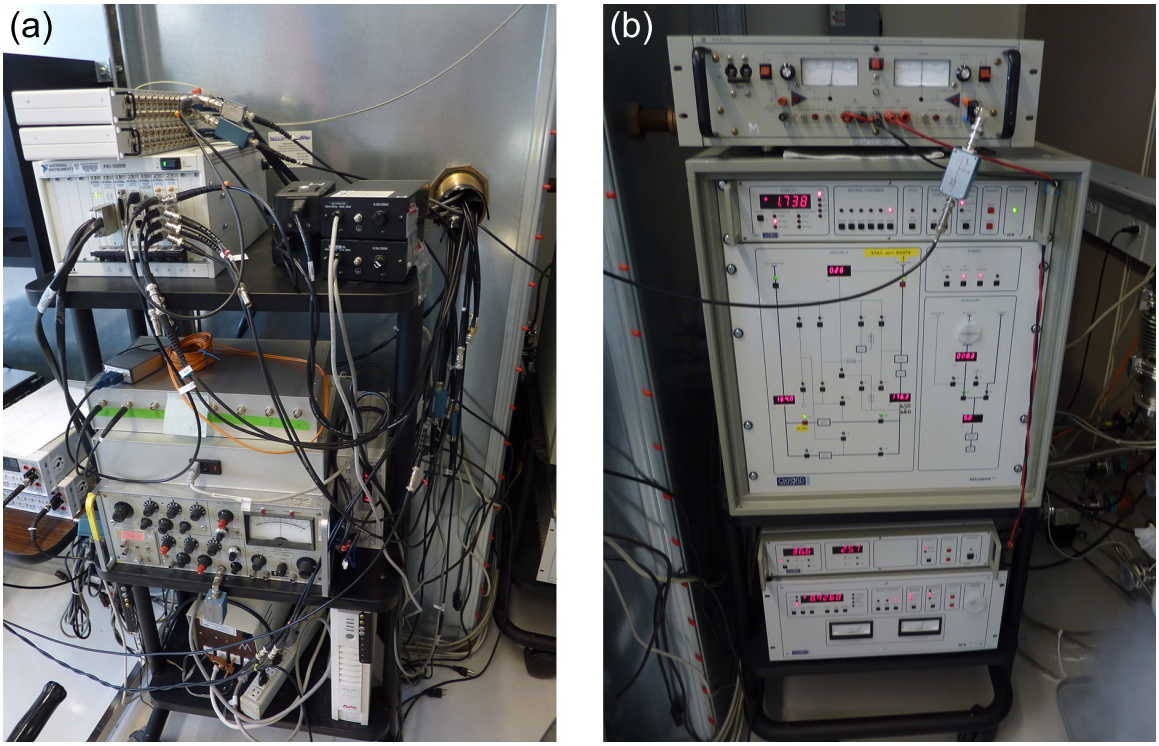

Figure C.2: Non-conductive racks containing all hardware components except the fridge, pre-amplifiers and DAC's (all located inside the shielded room), and the main and lock-in computers (located on a desk opposite the equipment racks). (a) Top shelf: PXI system and power supplies for pre-amplifiers. Middle shelf: BabyDAC unit, BabyDAC power supply, and PAR 124 lock-in amplifier. This equipment is used for testing ohmic contacts and devices in a 4 K dunker. The DAC connects to the a card on the PXI rack, allowing it to be controlled from the lock-in computer. Using a second instance of Igor on that computer to control the BabyDAC and record the PAR 124 measurements (digitized using a Hewlett-Packard 34401A DMM) does not compromise the performance of the digital lock-in software running in the main instance of Igor. Bottom shelf: ground-isolating transformer and surge suppressor with battery backup. All equipment except the computers, IGH, and magnet power supplies are powered from the isolation transformer, which is grounded to a clean grounding point. The battery backup is used for the DAC's and pre-amplifiers. (b) Top: Kepco BOP-20-20 power source, used for fine control of the magnet, with a BNC cable from a BabyDAC channel connected to its current-control port. Middle: Oxford IGH cabinet. Bottom: helium and nitrogen level meters, and Oxford IPS-120-10 magnet power supply. Lower-right corner: clouds emanate from an in-progress liquid nitrogen transfer.

of this tube are two equipment racks (Figure C.2). One rack holds measurement equipment and electronics power supplies, and the other holds the Oxford Intelligent Gas Handling (IGH) cabinet, cryogen level meters, and magnet power supplies. More details are given in

the Figure C.2 caption. Finally, the equipment on the racks connects to the two computers via fiber-optic, serial, and/or GPIB cables. The two computers communicate directly via serial cable.

C.2 Software

All data acquisition and analysis was performed using WaveMetrics Igor Pro ("Igor"). Igor provides many built-in functions for communicating with instruments and working with data, as well as the ability to write customized functions using a proprietary programming language. The customized functions used for these experiments, written primarily by myself and Yiming Zhang, are included in their entirety in the supplementary file IgorFiles.zip. The digital lock-in functions, which run on a dedicated computer, are probably the most complicated, and so a brief overview of their structure is given here.

C.2.1 Digital lock-in

The digital lock-in software consists of a set of functions implemented in Igor that perform three main functions: (a) interface with the user and the main acquisition computer, (b) data input and output, and (c) signal processing. The interface with the local user (Figure C.3) consists of a control panel and several graphs, which normally run in oscilloscope mode but can be switched to FFT mode for diagnostic purposes. Communication with the main acquisition computer is done over a direct serial cable connection, accessed via a COM port on each computer. Data input and output relies on the WaveMetrics NI-DAQ Tools MX package for Igor Pro, which allows Igor to communicate with the digitizer cards. Finally, the signal processing functions use Igor's built-in FFT and other mathematical operations.

Once the lock-in is started, it acquires and analyzes blocks of data continuously

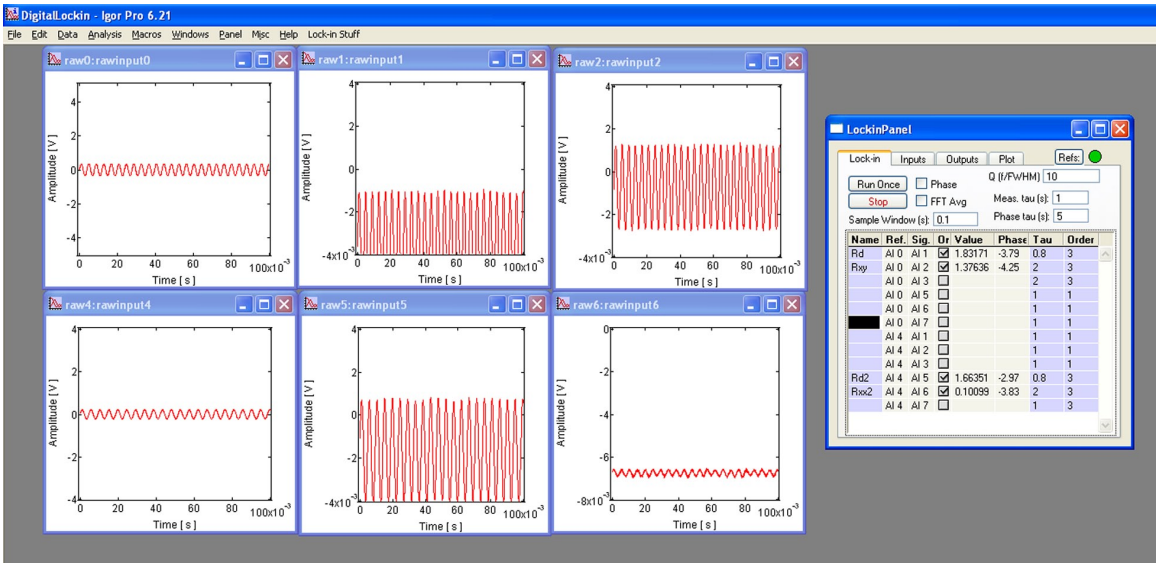

Figure C.3: Screenshot of digital lock-in software running in Igor Pro. The control panel at right allows full control of the lock-in input and output settings, and the graphs at left show real-time oscilloscope-like views of the active reference and signal channels.

until stopped. Three separate background tasks each run about 10 times per second: one checks the COM port for new requests and handles any it finds, and the other two download and analyze new blocks of data from the two digitizers. During intervals when no task is running, Igor responds to keyboard and mouse input while the digitizers acquire data.

C.2.2 Code listings

The supplementary file IgorFiles.zip contains two folders, one for digital lock-in files and one for general data acquisition files. Each folder includes a single *.pxp (Igor packed experiment) file that contains relevant variables, control panels, and other windows. The *.pxp files cannot be opened outside of Igor, but the associated *.ipf files, which contain our functions, can be opened using any text editor. The organization of code in these files is outlined below. Files not listed below contain functions written by other lab members and not substantially modified by me, as well as many small functions whose purpose and

workings are trivial.

- Digital lock-in code (associated with DigitalLockin.pxp):
  - All functions: DigitalLockin_PXI.ipf
- Other data acquisition code (associated with DataAcquisition.pxp):
  - Control - DAC boards: IngotDAC_VERSA.ipf
  - Control - digital lock-in: LockinControl.ipf
  - Acquisition - single data points: SingleRead.ipf
  - Acquisition - single-parameter sweeps: OnedSweeps.ipf
  - Acquisition - two-parameter sweeps: TwodSweep.ipf
  - Analysis - graph manipulation: GraphAnalysis.ipf
  - Analysis - specialized FFT procedures, etc.: GeneralAnalysis.ipf
  - Analysis - temperature dependence: FFT_TempDep_Analysis.ipf
  - Analysis - oscillation period analysis widget: OscCalc.ipf
  - Misc. - file and folder management: FileFolderProcedures.ipf
  - Misc. - control panel for gas handling cabinet: Virtual_IGH.ipf
  - Misc. - interface to SyncBackSE backup software: Backups_WinXP.ipf

Appendix D

Catalog of good wafers and devices

D.1 Wafer and device list

The published results presented in this thesis amount to a small subset of the measurements performed over the course of doing these experiments. The majority of cooldowns, devices, and wafers did not lead directly to published results, but on the other hand, relatively few turned out to be totally useless. This section provides details of not only the wafers and devices that led to published results, but also those that led to interesting or useful unpublished results.

In the table below, wafer ID's are of the form X(M)M-(D)D-YY.N, where X is either "M" (grown by Manfra) or "P" (grown by Pfeiffer), and the remaining fields indicate the wafer's month, day and year of growth, and serial number. Chip ID's are of the form XYZN, where XYZ are the initials of the person who cleaved the chip, and N is a serial number. Device ID's reflect the location on the chip: a letter for the mesa row, followed by a letter or number for the mesa column, possibly followed by a letter for the position on the mesa. Square-mesa chips have sixteen mesas, arranged in four rows (A through D from top to bottom) and four columns (1 through 4 from left to right), with one device per mesa.

Hall-bar chips have sixteen Hall bars in eight rows (A through H from top to bottom) and two columns (L=Left and R=Right), with up to three devices per mesa (L=Left, C=Center, and R=Right). Some small chips follow neither convention, in which case the device ID is listed as "N/A," but the device may be identified by inspection under a microscope.

Listed devices are all Fabry-Perot interferometers with comparable geometries, and can be assumed to use surface gates unless a trench depth is listed, with no helper or screening gates unless otherwise indicated. For devices with a range of constriction sizes listed, helper gates are divided into multiple segments, as in Figure A.3(a), allowing the constriction sizes to be changed by depleting one or more segments.

Table D.1: List of notable wafers and devices used for these experiments, sorted by date of wafer growth. Densities (n) and mobilities (μ) are for un-illuminated 2DEG except where indicated by an L. The parameters d, t, and s all indicate distances from the top of the 2DEG layer to other layers: d to the top of the wafer, t to the bottom of the 2DEG layer, and s to the nearest donor layer.

Wafer ID	n [cm^{-2}]	μ [cm^2/Vs]	$d+t$ [nm]	s [nm]	Doping Wells
	Wafer notes				
Chip ID	Device ID: description				
P2-25-05.1	2.6×10^{11}	25×10^6	$195 + 30$	80	Yes
	Jack-of-all-trades wafer: good mobility and second Landau level features, intermediate density, decent gating.				
ELF1	N/A: area 2 μm^2, constrictions 250 nm $-$ 1 μm, helper and screening gates. Good CD oscillations. Data presented in Chapter 2.				
P5-15-07.1	L: 3.9×10^{11}	L: 26×10^6	$176 + 24$	78	No
	Excellent second Landau level after illumination. Stable gating without illumination. GaAs screening wells between 2DEG and donor layers.				
WC1	A1: area 2 μm^2, constrictions 250 nm $-$ 1 μm, helper gates. Good CD and simultaneous AB.				
P6-27-07.1	2.7×10^{11}	25×10^6	$195 + 30$	80	Yes
	Copy of P2-25-05.1.				
ELF1	N/A: area 8 μm^2, constrictions 250 nm $-$ 1 μm, helper and screening gates. Good AB oscillations. Velocities measured from AB were consistent with the framework presented in Chapter 3.				
	N/A: area 20 μm^2, constrictions 250 nm $-$ 1 μm, helper and screening gates. Good AB oscillations, presented in Chapters 2 and 3.				

Table D.1 continued on next page...

Table D.1 (continued)

P7-28-08.2	0.8×10^{11}	13×10^6	$400 + 48$	300	No
	Very stable gating.				
DTM2	A2: area 4 μm^2, constrictions 250 nm $-$ 1 μm, helper and screening gates. Main device used for DNP measurements in Chapter 4. Shows good CD oscillations and some AB at lower fields, which yielded velocity measurements consistent with the framework presented in Chapter 3. First observation of simultaneous AB and CD.				
WC1	A3: area 20 μm^2, constrictions 250 nm $-$ 1 μm, helper gates. Showed CD oscillations only.				
P11-18-08.1	1.6×10^{11}	12×10^6	$230 + 30$	130	No
	Very stable gating.				
DTM1	N/A: area 2 μm^2, constrictions 250 nm $-$ 1 μm, helper gates. Some DNP effects studied here.				
DTM2	A2: area 20 μm^2, constrictions 250 nm $-$ 1 μm, helper and screening gates. Some AB oscillations at low field. Velocities measured from AB were consistent with the framework presented in Chapter 3.				
	C3: area 9 μm^2, constrictions 500 nm, trench depth 120 nm. First RIE-etched device. Strong AB oscillations at low field (first time seen in a device without a screening gate). Velocities measured from AB were consistent with the framework presented in Chapter 3.				
P2-22-10.1	1.6×10^{11}	19×10^6	$270 + 40$	160	Yes
	An excellent wafer: good mobility and second Landau level features despite the relatively low density, good fractions between filling factors 1 and 2, decent gating.				
DTM1	A4: area 2 μm^2, constrictions 600 nm, trench depth 120 nm. First observation of CD oscillations at fractional f_c: 2/3, 5/3, and unstable ones at 1/3. Data presented in Chapter 5. Some ohmic contacts are poor.				
WC1	A4: area 1 μm^2, constrictions 550 nm, trench depth 150 nm. Good CD oscillations at $f_c = 1/3, 2/3, 5/3$. Temperature dependence presented in Chapter 6.				
	C2: area 4 μm^2, constrictions 750 nm, trench depth 160 nm. Excellent CD oscillations at $f_c = 2/3$ and 4/3, and weak ones at 5/3. Data presented in Chapter 5. Not as good since a blob of some sort of organic contaminant happened to land right on it.				
	C3: same as C2 but with 1 μm constrictions. Some CD oscillations at $f_c = 2/3$ with fairly negative gate voltages.				
P2-23-10.1	3.0×10^{11}	25×10^6	$195 + 30$	80	Yes
	Similar to P2-22-10.1 but with higher 2DEG density. The second Landau level is not quite as nice, possibly the result of the use of less Si than usual in the doping wells in an attempt to improve gate stability.				

Table D.1 continued on next page...

Table D.1 (continued)

WC1	D4: area 20 μm^2, constrictions 500 nm, trench depth 120 nm. Good AB, but some gates shorted together.				
P10-12-10.1	2.8×10^{11}	22×10^6	$170 + 29$	80	Yes
	Surface states compensated by extra donors near surface rather than asymmetrically doped main wells. Second Landau level good but inconsistent; gating decent.				
DTM2	DRC: area 2 μm^2, constrictions 500 nm, trench depth 100 nm, constrictions broader than in the standard design. Relatively high zero-field, zero-gate-voltage diagonal resistance of almost 0.1 h/e^2, and AB oscillations with less pinch-off than typically needed.				
P10-12-10.2	2.0×10^{11}	18×10^6	$210 + 33$	120	Yes
	Similar to P10-12-10.1 but with lower 2DEG density. Second Landau level good but inconsistent; gating decent.				
DTM3	BLL: area 2 μm^2, constrictions 550 nm, trench depth 100 nm. Strong CD oscillations at $f_c = 2/3$, and some at 4/3 as well.				
M11-11-11.1	1.7×10^{11}	unknown	$185 + 30$	110	No
	Decent second Landau level, very stable gating when used without illumination.				
DTM2	BLC: area 2 μm^2, constrictions 500 nm, trench depth 100 nm. Good, stable AB oscillations in the dark (temperature-dependence scale versus magnetic field presented in Chapter 6). First observation of somewhat stable oscillations after illumination, but CD only.				

D.2 Wafer data sheets

Data sheets containing more details about all of the wafers grown by Pfeiffer are included in the supplementary file WaferDataSheets.pdf.

Bibliography

[1] E. Hall, *On a new action of the magnet on electric currents*, Am. J. Math. **2**, 287 (1879).

[2] K. von Klitzing, G. Dorda, and M. Pepper, *New method for high accuracy determination of the fine-structure constant based on quantized Hall resistance*, Phys. Rev. Lett. **45**, 494 (1980).

[3] B. Jeckelmann and B. Jeanneret, *The quantum Hall effect as an electrical resistance standard*, Rep. Prog. Phys. **64**, 1603 (2001).

[4] D. C. Tsui, H. L. Stormer, and A. C. Gossard, *Two-dimensional magnetotransport in the extreme quantum limit*, Phys. Rev. Lett. **48**, 1559 (1982).

[5] H. L. Stormer, D. C. Tsui, and A. C. Gossard, *The fractional quantum Hall effect*, Rev. Mod. Phys. **71**, S298 (1999).

[6] R. Willett, J. P. Eisenstein, H. L. Störmer, D. C. Tsui, A. C. Gossard, and J. H. English, *Observation of an even-denominator quantum number in the fractional quantum Hall effect*, Phys. Rev. Lett. **59**, 1776 (1987).

[7] G. Moore and N. Read, *Nonabelions in the fractional quantum Hall effect*, Nuc. Phys. B **360**, 362 (1991).

[8] J. Bardeen, L. N. Cooper, and J. R. Schrieffer, *Theory of superconductivity*, Phys. Rev. **108**, 1175 (1957).

[9] J. K. Jain, *Composite-fermion approach for the fractional quantum Hall effect*, Phys. Rev. Lett. **63**, 199 (1989).

[10] A. A. Koulakov, M. M. Fogler, and B. I. Shklovskii, *Charge density wave in two-dimensional electron liquid in weak magnetic field*, Phys. Rev. Lett. **76**, 499 (1996).

[11] M. M. Fogler, A. A. Koulakov, and B. I. Shklovskii, *Ground state of a two-dimensional electron liquid in a weak magnetic field*, Phys. Rev. B **54**, 1853 (1996).

[12] J. K. Jain, *Composite Fermions* (Cambridge University Press, Cambridge, 2007).

[13] A. Y. Kitaev, *Fault-tolerant quantum computation by anyons*, Ann. Phys. **303**, 2 (2003).

[14] S. Das Sarma, M. Freedman, and C. Nayak, *Topologically protected qubits from a possible non-Abelian fractional quantum Hall state*, Phys. Rev. Lett. **94**, 166802 (2005).

[15] M. P. Marder, *Condensed Matter Physics*, 2nd Ed. (Wiley, New York, 2010).

[16] A. Y. Cho, *Film deposition by molecular beam techniques*, J. Vac. Sci. Tech. **8**, S31 (1971).

[17] S. M. Sze, *Physics of Semiconductor Devices*, 2nd Ed. (Wiley, New York, 1981).

[18] B. A. Piot, J. Kunc, M. Potemski, D. K. Maude, C. Betthausen, A. Vogl, D. Weiss, G. Karczewski, and T. Wojtowicz, *Fractional quantum Hall effect in CdTe*, Phys. Rev. B **82**, 081307 (2010).

[19] C. R. Dean, A. F. Young, P. Cadden-Zimansky, L. Wang, H. Ren, K. Watanabe, T. Taniguchi, P. Kim, J. L. Hone, and K. L. Shepard, *Multicomponent fractional quantum Hall effect in graphene*, Nat. Phys. **7**, 693 (2011).

[20] V. Umansky, M. Heiblum, Y. Levinson, J. Smet, J. Nübler, and M. Dolev, *MBE growth of ultra-low disorder 2DEG with mobility exceeding* 35×10^6 cm^2/Vs, J. Crystal Growth **311**, 1658 (2008).

[21] D. C. Look, *Electrical Characterization of GaAs Materials and Devices* (Wiley, New York, 1989).

[22] V. Umansky, R. de Picciotto, and M. Heiblum, *Extremely high-mobility two dimensional electron gas: Evaluation of scattering mechanisms*, Appl. Phys. Lett. **71**, 683 (1997).

[23] S. Datta, *Electronic Transport in Mesoscopic Systems* (Cambridge University Press, Cambridge, 1995).

[24] C. W. J. Beenakker and H. van Houten, *Quantum transport in semiconductor nanostructures*, Solid State Phys. **44**, 1 (1991).

[25] R. B. Laughlin, *Anomalous quantum Hall effect: an incompressible quantum fluid with fractionally charged excitations*, Phys. Rev. Lett. **50**, 1395 (1983).

[26] W. Kang, H. L. Stormer, L. N. Pfeiffer, K. W. Baldwin, and K. W. West, *How real are composite fermions?*, Phys. Rev. Lett. **71**, 3850 (1993).

[27] V. J. Goldman, B. Su, and J. K. Jain, *Detection of composite fermions by magnetic focusing*, Phys. Rev. Lett. **72**, 2065 (1994).

[28] B. I. Halperin, *Theory of the quantized Hall conductance*, Helv. Phys. Acta **56**, 75 (1983).

[29] F. D. M. Haldane and E. H. Rezayi, *Spin-singlet wave function for the half-integral quantum Hall effect*, Phys. Rev. Lett. **60**, 956 (1988).

[30] M. Greiter, X.-G. Wen, and F. Wilczek, *Paired Hall state at half filling*, Phys. Rev. Lett. **66**, 3205 (1991).

[31] B. I. Halperin, P. A. Lee, and N. Read, *Theory of the half-filled Landau level*, Phys. Rev. B **47**, 7312 (1993).

[32] P. Bonderson, V. Gurarie, and C. Nayak, *Plasma analogy and non-Abelian statistics for Ising-type quantum Hall states*, Phys. Rev. B **83**, 075303 (2011).

[33] W. Pan, H. Stormer, D. Tsui, L. Pfeiffer, K. Baldwin, and K. West, *Experimental evidence for a spin-polarized ground state in the 5/2 fractional quantum Hall effect*, Solid State Commun. **119**, 641 (2001).

[34] M. Dolev, M. Heiblum, V. Umansky, A. Stern, and D. Mahalu, *Observation of a quarter of an electron charge at the $\nu = 5/2$ quantum Hall state*, Nature **452**, 829 (2008).

[35] I. P. Radu, J. B. Miller, C. M. Marcus, M. A. Kastner, L. N. Pfeiffer, and K. W. West, *Quasi-particle properties from tunneling in the $\nu = 5/2$ fractional quantum Hall state*, Science **320**, 899 (2008).

[36] V. Venkatachalam, A. Yacoby, L. N. Pfeiffer, and K. W. West, *Local charge of the 5/2 fractional quantum Hall state*, Nature **469**, 185 (2011).

[37] L. Tiemann, G. Gamez, N. Kumada, and K. Muraki, *Unraveling the spin polarization of the $\nu = 5/2$ fractional quantum Hall state*, Science **335**, 828 (2012).

[38] L. Saminadayar, D. C. Glattli, Y. Jin, and B. Etienne, *Observation of the e/3 fractionally charged Laughlin quasiparticle*, Phys. Rev. Lett. **79**, 2526 (1997).

[39] R. de Picciotto, M. Reznikov, M. Heiblum, V. Umansky, G. Bunin, and D. Mahalu, *Direct observation of a fractional charge*, Nature **389**, 162 (1997).

[40] M. Reznikov, R. de Picciotto, T. G. Griffiths, V. Umansky, and M. Heiblum, *Observation of quasiparticles with one-fifth of an electron's charge*, Nature **399**, 238 (1999).

[41] V. J. Goldman and B. Su, *Resonant tunneling in the quantum Hall regime: Measurement of fractional charge*, Science **267**, 1010 (1995).

[42] J. Martin, S. Ilani, B. Verdene, J. Smet, V. Umansky, D. Mahalu, D. Schuh, G. Abstreiter, and A. Yacoby, *Localization of fractionally charged quasi-particles*, Science **305**, 980 (2004).

[43] Y. C. Chung, M. Heiblum, and V. Umansky, *Scattering of bunched fractionally charged quasiparticles*, Phys. Rev. Lett. **91**, 216804 (2003).

[44] A. Bid, N. Ofek, M. Heiblum, V. Umansky, and D. Mahalu, *Shot noise and charge at the 2/3 composite fractional quantum Hall state*, Phys. Rev. Lett. **103**, 236802 (2009).

[45] M. Dolev, Y. Gross, Y. C. Chung, M. Heiblum, V. Umansky, and D. Mahalu, *Dependence of the tunneling quasiparticle charge determined via shot noise measurements on the tunneling barrier and energetics*, Phys. Rev. B **81**, 161303 (2010).

[46] D. Ferraro, A. Braggio, N. Magnoli, and M. Sassetti, *Charge tunneling in fractional edge channels*, Phys. Rev. B **82**, 085323 (2010).

[47] M. Carrega, D. Ferraro, A. Braggio, N. Magnoli, and M. Sassetti, *Anomalous charge tunneling in fractional quantum Hall edge states at a filling factor 5/2*, Phys. Rev. Lett. **107**, 146404 (2011).

[48] X. Lin, C. Dillard, M. A. Kastner, L. N. Pfeiffer, and K. W. West, *Measurements of quasiparticle tunneling in the $\nu = 5/2$ fractional quantum Hall state*, Phys. Rev. B **85**, 165321 (2012).

[49] F. E. Camino, W. Zhou, and V. J. Goldman, *$e/3$ Laughlin quasiparticle primary-filling $\nu = 1/3$ interferometer*, Phys. Rev. Lett. **98**, 076805 (2007).

[50] S. An, P. Jiang, H. Choi, W. Kang, S. H. Simon, L. N. Pfeiffer, K. W. West, and K. W. Baldwin, *Braiding of Abelian and non-Abelian anyons in the fractional quantum Hall effect*, arXiv:1112.3400 (2011).

[51] A. Stern, *Non-Abelian states of matter*, Nature **464**, 187 (2010).

[52] C. W. J. Beenakker, *Edge channels for the fractional quantum Hall effect*, Phys. Rev. Lett. **64**, 216 (1990).

[53] C. de C. Chamon and X. G. Wen, *Sharp and smooth boundaries of quantum Hall liquids*, Phys. Rev. B **49**, 8227 (1994).

[54] C. L. Kane, M. P. A. Fisher, and J. Polchinski, *Randomness at the edge: Theory of quantum Hall transport at filling $\nu = 2/3$*, Phys. Rev. Lett. **72**, 4129 (1994).

[55] C. L. Kane and M. P. A. Fisher, *Impurity scattering and transport of fractional quantum Hall edge states*, Phys. Rev. B **51**, 13449 (1995).

[56] A. Bid, N. Ofek, H. Inoue, M. Heiblum, C. L. Kane, V. Umansky, and D. Mahalu, *Observation of neutral modes in the fractional quantum Hall regime*, Nature **466**, 585 (2010).

[57] V. Venkatachalam, S. Hart, L. N. Pfeiffer, K. W. West, and A. Yacoby, *Local thermometry of neutral modes on the quantum Hall edge*, arXiv:1202.6681 (2012).

[58] Y. Q. Li and J. H. Smet, *Nuclear-electron spin interactions in the quantum Hall regime*, in *Spin Physics in Semiconductors*, edited by M. I. Dyakonov (Springer-Verlag, Berlin, 2008).

[59] J. P. Eisenstein, H. L. Stormer, and L. N. Pfeiffer, *Evidence for a spin transition in the $\nu = 2/3$ fractional quantum Hall effect*, Phys. Rev. B **41**, 7910 (1990).

[60] J. P. Eisenstein, R. Willett, H. L. Stormer, D. C. Tsui, A. C. Gossard, and J. H. English, *Collapse of the even-denominator fractional quantum Hall effect in tilted fields*, Phys. Rev. Lett. **61**, 997 (1988).

[61] R. H. Morf, *Transition from quantum Hall to compressible states in the second Landau level: New light on the 5/2 enigma*, Phys. Rev. Lett. **80**, 1505 (1998).

[62] W. Pan, J.-S. Xia, V. Shvarts, D. E. Adams, H. L. Stormer, D. C. Tsui, L. N. Pfeiffer, K. W. Baldwin, and K. W. West, *Exact quantization of the even-denominator fractional quantum Hall state at 5/2 Landau level filling factor*, Phys. Rev. Lett. **83**, 3530 (1999).

[63] M. Kawamura, H. Takahashi, K. Sugihara, and S. Masubuchi, *Electrical polarization of nuclear spins in a breakdown regime of quantum Hall effect*, Appl. Phys. Lett. **90**, 022102 (2007).

[64] M. Kawamura, M. Ono, Y. Hashimoto, S. Katsumoto, K. Hamaya, and T. Machida, *Dynamic nuclear polarization induced by breakdown of fractional quantum Hall effect*, Phys. Rev. B **79**, 193304 (2009).

[65] K. R. Wald, L. P. Kouwenhoven, P. L. McEuen, N. C. van der Vaart, and C. T. Foxon, *Local dynamic nuclear polarization using quantum point contacts*, Phys. Rev. Lett. **73**, 1011 (1994).

[66] S. L. Sondhi, A. Karlhede, S. A. Kivelson, and E. H. Rezayi, *Skyrmions and the crossover from the integer to fractional quantum Hall effect at small Zeeman energies*, Phys. Rev. B **47**, 16419 (1993).

[67] R. Cote, A. H. MacDonald, L. Brey, H. A. Fertig, S. M. Girvin, and H. T. C. Stoof, *Collective excitations, NMR, and phase transitions in Skyrme crystals*, Phys. Rev. Lett. **78**, 4825 (1997).

[68] K. Hashimoto, K. Muraki, T. Saku, and Y. Hirayama, *Electrically controlled nuclear spin polarization and relaxation by quantum-Hall states*, Phys. Rev. Lett. **88**, 176601 (2002).

[69] T. Young, *Experimental demonstration of the general law of the interference of light*, Phil. Trans. R. Soc. Lond. **94**, 1 (1804).

[70] C. Fabry and A. Perot, *Sur les franges des lames minces argentées et leur application à la mesure de petites épaisseurs d'air*, Ann. Chim. Phys. **12**, 459 (1897).

[71] L. Zehnder, *Ein neuer Interferenzrefraktor*, Instrumentenkunde **11**, 275 (1891).

[72] L. Mach, *Ueber einen Interferenzrefraktor*, Instrumentenkunde **12**, 89 (1892).

[73] B. J. van Wees, H. van Houten, C. W. J. Beenakker, J. G. Williamson, L. P. Kouwenhoven, D. van der Marel, and C. T. Foxon, *Quantized conductance of point contacts in a two-dimensional electron gas*, Phys. Rev. Lett. **60**, 848 (1988).

[74] A. Yacoby, U. Sivan, C. P. Umbach, and J. M. Hong, *Interference and dephasing by electron-electron interaction on length scales shorter than the elastic mean free path*, Phys. Rev. Lett. **66**, 1938 (1991).

[75] C. de C. Chamon, D. E. Freed, S. A. Kivelson, S. L. Sondhi, and X. G. Wen, *Two point-contact interferometer for quantum Hall systems*, Phys. Rev. B **55**, 2331 (1997).

[76] Y. Ji, Y. Chung, D. Sprinzak, M. Heiblum, D. Mahalu, and H. Shtrikman, *An electronic Mach-Zehnder interferometer*, Nature **422**, 415 (2003).

[77] L. P. Kouwenhoven, C. M. Marcus, P. L. McEuen, S. Tarucha, R. M. Westervelt, and N. S. Wingreen, *Electron transport in quantum dots*, in *Mesoscopic Electron Transport*, edited by L. L. Sohn, L. P. Kouwenhoven, and G. Schön, NATO ASI Series E, Vol. 345 (Kluwer, Dordrecht, 1997).

[78] D. E. Feldman and A. Kitaev, *Detecting non-Abelian statistics with an electronic Mach-Zehnder interferometer*, Phys. Rev. Lett. **97**, 186803 (2006).

[79] A. Stern and B. I. Halperin, *Proposed experiments to probe the $\nu = 5/2$ quantum Hall state*, Phys. Rev. Lett. **96**, 016802 (2006).

[80] C. Nayak, S. H. Simon, A. Stern, M. Freedman, and S. D. Sarma, *Non-Abelian anyons and topological quantum computation*, Rev. Mod. Phys. **80**, 1083 (2008).

[81] A. Stern, B. Rosenow, R. Ilan, and B. I. Halperin, *Interference, Coulomb blockade, and the identification of non-Abelian quantum Hall states*, Phys. Rev. B **82**, 085321 (2010).

[82] B. I. Halperin, A. Stern, I. Neder, and B. Rosenow, *Theory of the Fabry-Pérot quantum Hall interferometer*, Phys. Rev. B **83**, 155440 (2011).

[83] N. Byers and C. N. Yang, *Theoretical considerations concerning quantized magnetic flux in superconducting cylinders*, Phys. Rev. Lett. **7**, 46 (1961).

[84] B. Rosenow and S. H. Simon, *Telegraph noise and the Fabry-Perot quantum Hall interferometer*, arXiv:1111.6475 (2011).

[85] B. Rosenow, B. I. Halperin, S. H. Simon, and A. Stern, *Bulk-edge coupling in the non-Abelian 5/2 quantum Hall interferometer*, Phys. Rev. Lett. **100**, 226803 (2008).

[86] B. L. Altshuler, A. G. Aronov, and D. E. Khmelnitsky, *Effects of electron-electron collisions with small energy transfers on quantum localisation*, J. Phys. C **15**, 7367 (1982).

[87] B. Rosenow and B. I. Halperin, *Influence of interactions on flux and back-gate period of quantum Hall interferometers*, Phys. Rev. Lett. **98**, 106801 (2007).

[88] J. B. Miller, I. P. Radu, D. M. Zumbuhl, E. M. Levenson-Falk, M. A. Kastner, C. M. Marcus, L. N. Pfeiffer, and K. W. West, *Fractional quantum Hall effect in a quantum point contact at filling fraction 5/2*, Nat. Phys. **3**, 561 (2007).

[89] B. J. van Wees, L. P. Kouwenhoven, C. J. P. M. Harmans, J. G. Williamson, C. E. Timmering, M. E. I. Broekaart, C. T. Foxon, and J. J. Harris, *Observation of zero-dimensional states in a one-dimensional electron interferometer*, Phys. Rev. Lett. **62**, 2523 (1989).

[90] B. W. Alphenaar, A. A. M. Staring, H. van Houten, M. A. A. Mabesoone, O. J. A. Buyk, and C. T. Foxon, *Influence of adiabatically transmitted edge channels on single-electron tunneling through a quantum dot*, Phys. Rev. B **46**, 7236 (1992).

[91] R. P. Taylor, A. S. Sachrajda, P. Zawadzki, P. T. Coleridge, and J. A. Adams, *Aharonov-Bohm oscillations in the Coulomb blockade regime*, Phys. Rev. Lett. **69**, 1989 (1992).

[92] J. P. Bird, K. Ishibashi, Y. Aoyagi, and T. Sugano, *Precise period doubling of the Aharonov-Bohm effect in a quantum dot at high magnetic fields*, Phys. Rev. B **53**, 3642 (1996).

[93] F. E. Camino, W. Zhou, and V. J. Goldman, *Aharonov-Bohm superperiod in a Laughlin quasiparticle interferometer*, Phys. Rev. Lett. **95**, 246802 (2005).

[94] F. E. Camino, W. Zhou, and V. J. Goldman, *Realization of a Laughlin quasiparticle interferometer: Observation of fractional statistics*, Phys. Rev. B **72**, 075342 (2005).

[95] E.-A. Kim, *Aharanov-Bohm interference and fractional statistics in a quantum Hall interferometer*, Phys. Rev. Lett. **97**, 216404 (2006).

[96] B. Hackens, F. Martins, S. Faniel, C. A. Dutu, H. Sellier, S. Huant, M. Pala, L. Desplanque, X. Wallart, and V. Bayot, *Imaging Coulomb islands in a quantum Hall interferometer*, Nat. Commun. **1**, 39 (2010).

[97] I. Neder, M. Heiblum, Y. Levinson, D. Mahalu, and V. Umansky, *Unexpected behavior in a two-path electron interferometer*, Phys. Rev. Lett. **96**, 016804 (2006).

[98] L. V. Litvin, H.-P. Tranitz, W. Wegscheider, and C. Strunk, *Decoherence and single electron charging in an electronic Mach-Zehnder interferometer*, Phys. Rev. B **75**, 033315 (2007).

[99] P. Roulleau, F. Portier, D. C. Glattli, P. Roche, A. Cavanna, G. Faini, U. Gennser, and D. Mailly, *Finite bias visibility of the electronic Mach-Zehnder interferometer*, Phys. Rev. B **76**, 161309 (2007).

[100] J. T. Chalker, Y. Gefen, and M. Y. Veillette, *Decoherence and interactions in an electronic Mach-Zehnder interferometer*, Phys. Rev. B **76**, 085320 (2007).

[101] I. Neder and E. Ginossar, *Behavior of electronic interferometers in the nonlinear regime*, Phys. Rev. Lett. **100**, 196806 (2008).

[102] I. P. Levkivskyi and E. V. Sukhorukov, *Dephasing in the electronic Mach-Zehnder interferometer at filling factor* $\nu = 2$, Phys. Rev. B **78**, 045322 (2008).

[103] M. D. Godfrey, P. Jiang, W. Kang, S. H. Simon, K. W. Baldwin, L. N. Pfeiffer, and K. W. West, *Aharonov-Bohm-like oscillations in quantum Hall corrals*, arXiv:0708.2448 (2007).

[104] P. V. Lin, F. E. Camino, and V. J. Goldman, *Electron interferometry in the quantum Hall regime: Aharonov-Bohm effect of interacting electrons*, Phys. Rev. B **80**, 125310 (2009).

[105] N. Ofek, A. Bid, M. Heiblum, A. Stern, V. Umansky, and D. Mahalu, *The role of interactions in an electronic Fabry-Perot interferometer operating in the quantum Hall effect regime*, Proc. Natl. Acad. Sci. USA **107**, 5276 (2010).

[106] R. L. Willett, L. N. Pfeiffer, and K. W. West, *Alternation and interchange of e/4 and e/2 period interference oscillations consistent with filling factor 5/2 non-Abelian quasiparticles*, Phys. Rev. B **82**, 205301 (2010).

[107] R. L. Willett, L. N. Pfeiffer, and K. W. West, *Measurement of filling factor 5/2 quasiparticle interference with observation of charge e/4 and e/2 period oscillations*, Proc. Natl. Acad. Sci. USA **106**, 8853 (2009).

[108] P. Roulleau, F. Portier, P. Roche, A. Cavanna, G. Faini, U. Gennser, and D. Mailly, *Direct measurement of the coherence length of edge states in the integer quantum Hall regime*, Phys. Rev. Lett. **100**, 126802 (2008).

[109] L. V. Litvin, A. Helzel, H.-P. Tranitz, W. Wegscheider, and C. Strunk, *Edge-channel interference controlled by Landau level filling*, Phys. Rev. B **78**, 075303 (2008).

[110] L. V. Litvin, A. Helzel, H.-P. Tranitz, W. Wegscheider, and C. Strunk, *Measurement of the transmission phase through a quantum dot embedded in one arm of an electronic Mach-Zehnder interferometer*, arXiv:0912.1230 (2009).

[111] B. L. Altshuler, P. A. Lee, and R. A. Webb, *Mesoscopic Phenomena in Solids* (North-Holland, Amsterdam, 1991).

[112] W. Liang, M. Bockrath, D. Bozovic, J. H. Hafner, M. Tinkham, and H. Park, *Fabry-Pérot interference in a nanotube electron waveguide*, Nature **411**, 665 (2001).

[113] I. L. Aleiner, P. W. Brouwer, and L. I. Glazman, *Quantum effects in Coulomb blockade*, Phys. Rep. **358**, 309 (2002).

[114] E. Buks, R. Schuster, M. Heiblum, D. Mahalu, and V. Umansky, *Dephasing in electron interference by a 'which-path' detector*, Nature **391**, 871 (1998).

[115] D. C. Glattli, C. Pasquier, U. Meirav, F. I. B. Williams, Y. Jin, and B. Etienne, *Co-tunneling of the charge through a 2-D electron island*, Z. Phys. B **85**, 375 (1991).

[116] J. A. Folk, S. R. Patel, S. F. Godijn, A. G. Huibers, S. M. Cronenwett, C. M. Marcus, K. Campman, and A. C. Gossard, *Statistics and parametric correlations of Coulomb blockade peak fluctuations in quantum dots*, Phys. Rev. Lett. **76**, 1699 (1996).

[117] S. M. Cronenwett, S. R. Patel, C. M. Marcus, K. Campman, and A. C. Gossard, *Mesoscopic fluctuations of elastic cotunneling in Coulomb blockaded quantum dots*, Phys. Rev. Lett. **79**, 2312 (1997).

[118] P. Bonderson, A. Kitaev, and K. Shtengel, *Detecting non-Abelian statistics in the $\nu = 5/2$ fractional quantum Hall state*, Phys. Rev. Lett. **96**, 016803 (2006).

[119] R. Ilan, E. Grosfeld, and A. Stern, *Coulomb blockade as a probe for non-Abelian statistics in Read-Rezayi states*, Phys. Rev. Lett. **100**, 086803 (2008).

[120] W. Zhou, F. E. Camino, and V. J. Goldman, *Quantum transport in an Aharonov-Bohm electron interferometer*, AIP Conf. Proc. **850**, 1351 (2006).

[121] F. E. Camino, W. Zhou, and V. J. Goldman, *Quantum transport in electron Fabry-Perot interferometers*, Phys. Rev. B **76**, 155305 (2007).

[122] M. W. C. Dharma-wardana, R. P. Taylor, and A. S. Sachrajda, *The effect of Coulomb interactions on the magnetoconductance oscillations of quantum dots*, Solid State Commun. **84**, 631 (1992).

[123] S. Ihnatsenka and I. V. Zozoulenko, *Interacting electrons in the Aharonov-Bohm interferometer*, Phys. Rev. B **77**, 235304 (2008).

[124] F. E. Camino, W. Zhou, and V. J. Goldman, *Transport in the Laughlin quasiparticle interferometer: Evidence for topological protection in an anyonic qubit*, Phys. Rev. B **74**, 115301 (2006).

[125] Y. Zhang, D. T. McClure, E. M. Levenson-Falk, C. M. Marcus, L. N. Pfeiffer, and K. W. West, *Distinct signatures for Coulomb blockade and Aharonov-Bohm interference in electronic Fabry-Perot interferometers*, Phys. Rev. B **79**, 241304 (2009).

[126] P. L. McEuen, E. B. Foxman, J. Kinaret, U. Meirav, M. A. Kastner, N. S. Wingreen, and S. J. Wind, *Self-consistent addition spectrum of a Coulomb island in the quantum Hall regime*, Phys. Rev. B **45**, 11419 (1992).

[127] M. Keller, U. Wilhelm, J. Schmid, J. Weis, K. v. Klitzing, and K. Eberl, *Quantum dot in high magnetic fields: Correlated tunneling of electrons probes the spin configuration at the edge of the dot*, Phys. Rev. B **64**, 033302 (2001).

[128] M. Stopa, W. G. van der Wiel, S. D. Franceschi, S. Tarucha, and L. P. Kouwenhoven, *Magnetically induced chessboard pattern in the conductance of a Kondo quantum dot*, Phys. Rev. Lett. **91**, 046601 (2003).

[129] A. van Oudenaarden, M. H. Devoret, Y. V. Nazarov, and J. E. Mooij, *Magneto-electric Aharonov-Bohm effect in metal rings*, Nature **391**, 768 (1998).

[130] W. G. van der Wiel, Y. V. Nazarov, S. De Franceschi, T. Fujisawa, J. M. Elzerman, E. W. G. M. Huizeling, S. Tarucha, and L. P. Kouwenhoven, *Electromagnetic Aharonov-Bohm effect in a two-dimensional electron gas ring*, Phys. Rev. B **67**, 033307 (2003).

[131] Y. Aharonov and D. Bohm, *Significance of electromagnetic potentials in the quantum theory*, Phys. Rev. **115**, 485 (1959).

[132] Y. V. Nazarov, *Aharonov-Bohm effect in the system of two tunnel junctions*, Phys. Rev. B **47**, 2768 (1993).

[133] Y. V. Nazarov, *Quantum interference, tunnel junctions and resonant tunneling interferometer*, Physica B **189**, 57 (1993).

[134] E. V. Sukhorukov and V. V. Cheianov, *Resonant dephasing in the electronic Mach-Zehnder interferometer*, Phys. Rev. Lett. **99**, 156801 (2007).

[135] R. C. Ashoori, H. L. Stormer, L. N. Pfeiffer, K. W. Baldwin, and K. West, *Edge magnetoplasmons in the time domain*, Phys. Rev. B **45**, 3894 (1992).

[136] G. Ernst, N. B. Zhitenev, R. J. Haug, and K. von Klitzing, *Probing the edge of a 2DEG by time-resolved transport measurements*, Physica E **1**, 95 (1998).

[137] B. I. Halperin, private communication .

[138] B. Rosenow *et al.*, unpublished .

[139] B. L. Altshuler and A. G. Aronov, in *Electron-Electron Interactions in Disordered Systems*, edited by A. L. Efros and M. Pollak (North-Holland, Amsterdam, 1985).

[140] I. Kukushkin, K. von Klitzing, and K. Eberl, *Spin polarization of composite fermions: Measurements of the Fermi energy*, Phys. Rev. Lett. **82**, 3665 (1999).

[141] N. Freytag, M. Horvatić, C. Berthier, M. Shayegan, and L. Lévy, *NMR investigation of how free composite fermions are at $\nu = 1/2$*, Phys. Rev. Lett. **89**, 246804 (2002).

[142] W. Kang, J. Young, S. Hannahs, E. Palm, K. Campman, and A. Gossard, *Evidence for a spin transition in the $\nu = 2/5$ fractional quantum Hall effect*, Phys. Rev. B **56**, R12776 (1997).

[143] D. C. Dixon, K. R. Wald, P. L. McEuen, and M. R. Melloch, *Dynamic nuclear polarization at the edge of a two-dimensional electron gas*, Phys. Rev. B **56**, 4743 (1997).

[144] S. Kronmüller, W. Dietsche, K. v. Klitzing, G. Denninger, W. Wegscheider, and M. Bichler, *New type of electron nuclear-spin interaction from resistively detected NMR in the fractional quantum Hall effect regime*, Phys. Rev. Lett. **82**, 4070 (1999).

[145] J. Smet, R. Deutschmann, W. Wegscheider, G. Abstreiter, and K. von Klitzing, *Ising ferromagnetism and domain morphology in the fractional quantum Hall regime*, Phys. Rev. Lett. **86**, 2412 (2001).

[146] J. H. Smet, R. A. Deutschmann, F. Ertl, W. Wegscheider, G. Abstreiter, and K. von Klitzing, *Gate-voltage control of spin interactions between electrons and nuclei in a semiconductor*, Nature **415**, 281 (2002).

[147] T. Machida, S. Ishizuka, T. Yamazaki, S. Komiyama, K. Muraki, and Y. Hirayama, *Spin polarization of fractional quantum Hall edge channels studied by dynamic nuclear polarization*, Phys. Rev. B **65**, 233304 (2002).

[148] T. Machida and S. Komiyama, *Hysteretic feature of quantum-Hall-effect breakdown caused by the dynamic nuclear polarization*, J. Phys. Soc. Jpn. **72**, 199 (2003).

[149] O. Stern, N. Freytag, A. Fay, W. Dietsche, J. H. Smet, K. von Klitzing, D. Schuh, and W. Wegscheider, *NMR study of the electron spin polarization in the fractional quantum Hall effect of a single quantum well: Spectroscopic evidence for domain formation*, Phys. Rev. B **70**, 075318 (2004).

[150] G. Yusa, K. Muraki, K. Takashina, K. Hashimoto, and Y. Hirayama, *Controlled multiple quantum coherences of nuclear spins in a nanometre-scale device*, Nature **434**, 1001 (2005).

[151] L. A. Tracy, J. P. Eisenstein, L. Pfeiffer, and K. West, *Spin transition in the half-filled Landau level*, Phys. Rev. Lett. **98**, 086801 (2007).

[152] M. Kawamura, H. Takahashi, S. Masubuchi, Y. Hashimoto, S. Katsumoto, K. Hamaya, and T. Machida, *Dynamic nuclear polarization and Knight shift measurements in a breakdown regime of integer quantum Hall effect*, Physica E **40**, 1389 (2008).

[153] Y. Q. Li, V. Umansky, K. von Klitzing, and J. H. Smet, *Nature of the spin transition in the half-filled Landau level*, Phys. Rev. Lett. **102**, 046803 (2009).

[154] C. R. Dean, B. A. Piot, G. Gervais, L. N. Pfeiffer, and K. W. West, *Current-induced nuclear-spin activation in a two-dimensional electron gas*, Phys. Rev. B **80**, 153301 (2009).

[155] Y. Ren, W. Yu, S. M. Frolov, J. A. Folk, and W. Wegscheider, *Nuclear polarization in quantum point contacts in an in-plane magnetic field*, Phys. Rev. B **81**, 125330 (2010).

[156] P. Khandelwal, A. E. Dementyev, N. N. Kuzma, S. E. Barrett, L. N. Pfeiffer, and K. W. West, *Spectroscopic evidence for the localization of Skyrmions near* $\nu = 1$ *as* $T \to 0$, Phys. Rev. Lett. **86**, 5353 (2001).

[157] J. K. Jain, *Composite Fermions* (Cambridge University Press, Cambridge, 2007).

[158] J. B. Miller, *Electron transport in GaAs heterostructures at various magnetic fields*, Ph.D. thesis, Harvard University (2007).

[159] R. E. Williams, *Modern GaAs Processing Methods*, 2nd Ed. (Artech House, Norwood, MA, 1990).

[160] R. Dingle, H. L. Stormer, A. C. Gossard, and W. Wiegmann, *Electron mobilities in modulation-doped semiconductor heterojunction devices*, Appl. Phys. Lett. **33**, 665 (1978).

[161] G. Gamez and K. Muraki, *5/2 fractional quantum Hall state in low-mobility electron systems: Different roles of disorder*, arXiv:1101.5856 (2011).

[162] P. M. Mooney, *Deep donor levels (DX centers) in III-V semiconductors*, J. Appl. Phys. **67**, R1 (1990).

[163] J. H. Davies, I. A. Larkin, and E. V. Sukhorukov, *Modeling the patterned two-dimensional electron gas: Electrostatics*, J. Appl. Phys. **77**, 4504 (1995).

[164] D. T. McClure, Y. Zhang, B. Rosenow, E. M. Levenson-Falk, C. M. Marcus, L. N. Pfeiffer, and K. W. West, *Edge-state velocity and coherence in a quantum Hall Fabry-Pérot interferometer*, Phys. Rev. Lett. **103**, 206806 (2009).

[165] D. T. McClure, W. Chang, C. M. Marcus, L. N. Pfeiffer, and K. W. West, *Fabry-Perot interferometry with fractional charges*, arXiv:1112.0538 (2011).

[166] O. V. Lounasmaa, *Experimental Principles and Methods Below 1 K*, 1st Ed. (Academic Press, New York, 1974).

[167] F. Pobell, *Matter and Methods at Low Temperatures*, 2nd Ed. (Springer-Verlag, Berlin, 1996).

[168] N. H. Balshaw, *Practical Cryogenics: an Introduction to Laboratory Cryogenics*, 2nd Ed. (Oxford Instruments Superconductivity Ltd., Oxon, England, 2001).

[169] K. Bladh, D. Gunnarsson, E. Hürfeld, S. Devi, C. Kristoffersson, B. Smålander, S. Pehrson, T. Claeson, P. Delsing, and M. Taslakov, *Comparison of cryogenic filters for use in single electronics experiments*, Review of Scientific Instruments **74**, 1323 (2003).

[170] D. G. Park, D. W. Kim, C. S. Angani, V. P. Timofeev, and Y. M. Cheong, *Measurement of the magnetic moment in a cold worked 304 stainless steel using HTS SQUID*, J. Magn. Magn. Mater. **320**, 571 (2008).

[171] J. P. Kauppinen, K. T. Loberg, A. J. Manninen, and J. P. Pekola, *Coulomb blockade thermometer: Tests and instrumentation*, Rev. Sci. Instrum. **69**, 4166 (1998).

[172] L. Spietz, K. W. Lehnert, I. Siddiqi, and R. J. Schoelkopf, *Primary electronic thermometry using the shot noise of a tunnel junction*, Science **300**, 1929 (2003).

[173] T. Ando, *Theory of quantum transport in a two-dimensional electron system under magnetic fields. IV. Oscillatory conductivity*, J. Phys. Soc. Jpn. **37**, 1233 (1974).

[174] G. S. Boebinger, A. M. Chang, H. L. Stormer, and D. C. Tsui, *Magnetic field dependence of activation energies in the fractional quantum Hall effect*, Phys. Rev. Lett. **55**, 1606 (1985).

[175] E. Buks, M. Heiblum, Y. Levinson, and H. Shtrikman, *Scattering of a two-dimensional electron gas by a correlated system of ionized donors*, Semicond. Sci. Technol. **9**, 2031 (1994).